Simulation of Electromagnetic Fields in Double Negative Metamaterials

Vom Fachbereich Elektrotechnik und Informationstechnik
der Technischen Universität Darmstadt

zur Erlangung des akademischen Grades eines
Doktor - Ingenieurs (Dr.-Ing.)
genehmigte

DISSERTATION

von

Grzegorz Lubkowski, M.Sc.
geboren am 23. Juli 1976 in Danzig

Referent:	Prof. Dr.-Ing. Thomas Weiland
Korreferent:	Prof. Dr.-Ing. Rolf Jakoby
Korreferent:	Prof. Dr.-Ing. Rolf Schuhmann

Tag der Einreichung:	03.07.09
Tag der mündlichen Prüfung:	22.10.09

D 17
Darmstädter Dissertation

Darmstadt 2009

Abstract

Metamaterials are artificially fabricated structures that have new, physically realizable response functions that do not occur or may not be readily available in nature. This thesis presents an efficient approach to the numerical modeling of metamaterial structures. Metamaterials are analysed at two levels: as microstructures (unit cells) and macrostructures (periodic lattices). The simulation approach at the unit-cell level is based on the extraction of effective constitutive parameters, solution of a periodic boundary eigenvalue problem and analysis of higher order modes. Macrostructure simulations provide reference and validation to the proposed modeling procedure.

The popular homogenization method based on the extraction of effective constitutive parameters from scattering matrix often delivers non-physical results in the frequency range of interest. The homogenization approach proposed within this work and based on the parameter fitting of dispersive models allows one to avoid the common pitfalls of the popular $\boldsymbol{S}$-retrieval method.

Metamaterials occupy a special niche between homogeneous media and photonic crystals. For that reason, Bloch analysis and computation of band structures constitute important tools in the modeling of metamaterials. Dispersion diagrams obtained as a solution of a periodic boundary eigenvalue problem reveal the passbands, stopbands and the type of the wave propagated in the lattice, that allows for the verification of the homogenized effective description.

Due to the inherent resonant character, most metamaterial structures are characterized by a significant level of higher order modes near the resonance frequency. Simulation results of a multimode scattering matrix for a metamaterial unit cell allow one to identify the spectral range in which the homogenized metamaterial model is not valid because of a non-negligible contribution of the higher order modes to the transmission process.

The simulation results of a negative refraction observed in the rigorous and homogenized implementations of the metamaterial macrostructure provide the validation of the presented numerical approach. It is shown that the relevant information regarding the phenomena observed at the macrostructure level can be predicted from the unit-cell level analysis. Application of the homogenized model allows for a significant reduction of the computational costs.

Kurzfassung

Metamaterialien sind künstlich hergestellte Strukturen mit neuartigen physikalischen Eigenschaften, wie sie nicht in der Natur auftreten. Diese Dissertation stellt einen effizienten Ansatz für die numerische Modellierung von Metamaterialien vor. Metamaterialien werden auf zwei Ebenen analysiert: In Form ihrer Elementarzellen (Mikrostruktur) und als periodische Anordnungen (Makrostruktur). Der Simulationsansatz auf der Elementarzellenebene basiert auf der Extraktion von effektiven konstitutiven Parametern, der Bestimmung der Eigenmoden der Elementarzellen und der Analyse von Moden höherer Ordnung. Simulationen der Makrostruktur liefern eine Referenz und Validierung für die vorgeschlagenen Modellierungsverfahren.

Die bisher meist verwendete Homogenisierungsmethode auf Basis einer Extraktion von effektiven konstitutiven Parametern aus der Streumatrix liefert oft nicht-physikalische Ergebnisse im betrachteten Frequenzbereich. Der neue Homogenisierungsansatz, der in dieser Doktorarbeit vorgeschlagen wird, basiert auf der Parameteranpassung von dispersiven Materialmodellen und vermeidet einige Schwachstellen des genannten Streumatrix-Extraktionsverfahrens.

Metamaterialien sind eine besondere Klasse von periodischen Materialien, die sich zwischen homogenen Medien und photonischen Kristallen einordnen lässt. Aus diesem Grund stellen eine Blochwellenanalyse und die Berechnung der Band-Struktur wichtige Werkzeuge in der Modellierung von Metamaterialien dar. Dispersionsdiagramme lassen als Lösung eines Eigenwertproblems auf die Passbänder, Stoppbänder und den Typ der im Gitter propagierenden Welle schließen und erlauben so eine Verifizierung der homogenisierten effektiven Beschreibung.

Aufgrund des inhärenten resonanten Charakters der meisten Metamaterial-Strukturen liegt in der Nähe der Resonanzfrequenz eine Vielzahl von Moden höherer Ordnung vor. Mit Hilfe von Simulationsergebnisse der multimodalen Streumatrix für eine Metamaterial-Elementarzelle lässt sich der Spektralbereich bestimmen, in dem das homogenisierte Metamaterial-Modell aufgrund des nicht vernachlässigbaren Beitrags der Moden höherer Ordnung nicht gültig ist.

Simulationsergebnisse für ein bekanntes Brechungsexperiment mit negativen Materialparametern, die sowohl mit einer detaillierten als auch mit einer homogenisierten Implementierung der Metamaterial-Makrostruktur vorgestellt werden, validieren den vorgeschlagenen numerischen Ansatz. Es kann gezeigt werden, dass alle relevanten Informationen bezüglich der beobachteten Phänomene in der Makrostrukturebene von der Elementarzellenanalyse vorausberechnet werden können. Die Anwendung des homogenisierten Modells ermöglicht eine erhebliche Reduzierung der numerischen Komplexität.

Contents

Chapter 1

Introduction

1.1 Overview

A growing interest in the research results concerning the interaction of electromagnetic waves with complex materials has been observed in the past few years. A reflection of this fact is a new term *metamaterial*, that has emerged in the literature and become part of the research language. Metamaterials represent an emerging research area, one that may pose many challenging objectives of interest to scientists and engineers.

Metamaterials are artificially fabricated structures that have new, physically realizable response functions that do not occur or may not be readily available in nature. They are not "materials" in the usual sense, but rather artificially prepared arrays of inclusions or inhomogeneities embedded in a host medium. The underlying interest in metamaterials is based on the ability to engineer tailored electromagnetic properties, where the corresponding inclusions act as artificial "molecules" that scatter the impinging electromagnetic field in a controlled manner. The structural units of metamaterials can be tailored in shape and size, their composition and morphology can be artificially tuned, and inclusions can be designed and placed at desired locations to achieve new functionality. From the technological and engineering point of view, the interest in metamaterials is based on the possibility of designing devices and systems with new properties or functionalities, able to open up new fields of applications or to improve existing ones.

Metamaterials can generally be analysed and modeled by analytical or computational methods. The analytical methods can provide physical insight and approximate models of the electromagnetic behavior, but only for some basic types of inclusions. For more complex "molecules", due to the numerous approximations, the analytical models become less accurate, more complicated and unworkable. On the other hand, every form of a metamaterial can be numerically analysed by conventional computational methods since it is an electromagnetic structure obeying Maxwell's equations. In this work, metamaterial structures are analysed by means of numerical methods.

1.1.1 Motivation and Project's Aims

The analysis of electromagnetic properties of any material is based on the macroscopic Maxwell equations, that in principle can be derived from a microscopic starting point, i.e. considering a microscopic world made up of electrons and nuclei [1]. A macroscopic amount of matter at rest contains of the order of $10^{23\pm5}$ electrons and nuclei, all in incessant motion because of thermal agitation, zero point vibration, or orbital motion. The spatial variations occur over distances of the order of 10^{-10} m. Typically, as the lower limit to the macroscopic domain, the length of 10^{-8} m is taken, corresponding to the volume of 10^{-24} m^3 containing of the order of 10^6 nuclei and electrons [1]. For such a large number of microscopic sources the solution of the quantum mechanical equations leading to the determination of the macroscopic behavior is not a tractable problem. Moreover, for the macroscopic observations, the detailed microscopic behavior of the fields with their drastic variations in space over atomic distances is not relevant. In any region of macroscopic interest with the scale length larger than 10^{-8} m the local fluctuations are removed by a spatial averaging, whereas the relevant macroscopic fields and sources are the quantities averaged over a large volume compared to the volume occupied by a single atom or molecule.

The situation is quite similar in the analysis of composite materials, where instead of using the equations of classical physics at the microscopic level (for rigorous analysis of particular inclusions), one uses homogenized or effective equations at the macroscopic level [2].

One of the possible approaches is the mathematical theory of homogenization which makes it possible to find effective material approximations of heterogeneous structures by homogenization of partial differential equations (PDE). This theory is often referred to as *classical homogenization*[1]. The main idea is to select two scales in the study: a microscopic one (corresponding to the size of the basic cell) and a macroscopic one (corresponding to the size of the macrostructure). From a physical point of view the modulus of the propagating field is forced to oscillate due to rapid changes in the permittivity and the permeability within the microstructure. Mathematically, a parameter corresponding to the size of the microstructure which describes the fine scale in the material is introduced. When this parameter is infinitely small the solution of PDE with rapidly oscillating coefficients converges to the solution of the homogenized PDE [4]. The homogenized equation has constant coefficients that correspond to a model of a homogeneous material. The classical homogenization is typically applied to lossless structures (most of the classical approaches assume the lack of losses) with the microscopic scale of the structure infinitely smaller than the wavelength in the medium.

An alternative approach to homogenization is based on the *mixing* approach [5]. The simplest model of a mixture is composed of two material components (phases): a certain volume of inclusion phase (guest) embedded in the environment (host). The main advantage of the mixing theory is the availability of a broad collection of simple mixing rules [e.g. Maxwell Garnett, Clausius-Mossotti (Lorenz-Lorentz) or Bruggeman formulas] [5]. These mixing rules, however, are available only for some basic shapes of inclusions, e.g. spheres or ellipsoids. On the other hand, the classical homogenization allows for general microstructure geometries. The mixing formulas require, similar to classical homogenization, that the size of the inhomogeneity is much smaller than the wavelength in the composite medium.

The common assumption of effective medium theories is that the wavelength of the electromagnetic (EM) wave is much longer than the characteristic size of the microstructure. In this case, for EM waves incident on the boundary between free space and the medium, the conventional refraction phenomenon is observed. On the other hand, for photonic crys-

---

[1] To be precise, the classical homogenization involves a heterogeneous medium with a moderate contrast, whereas in the non-classical case the heterogeneous medium consists of components with highly contrasting parameters, see e.g. [3].

tals the period of the lattice is most often comparable to the operating wavelength and the question arises if the homogenization (e.g. by notion of effective refractive index) can be used or if the medium is a diffraction grating characterized by the diffraction phenomenon. In the long wavelength region homogenization techniques approximate the effective refractive index in an asymptotic notion [6]. However, for wavelengths of an order comparable to the period of the structure, the situation becomes more complex. Propagation of EM waves in weakly modulated photonic crystals is basically similar to the propagation in a diffraction grating in which conventional refractive index loses its meaning. On the other hand, propagation in strongly modulated photonic crystals becomes refractionlike in the vicinity of the photonic bandgap and the structure behaves as a material having an effective refractive index controllable by the band structure. In this case a two dimensional photonic crystal can be represented by a bulk homogeneous material [7].

A metamaterial unit cell is typically composed of elements characterized by small electrical dimensions, which in an ideal case should be infinitesimal compared to the operating wavelength. The number of unit cells in a 3D metamaterial macrostructure is typically of the order of 1000 (equivalently 100 for a 2D analogue, or 10 for a 1D realization) [8]. In order to observe macroscopic phenomena the electrical size of the macrostructure has to be in the range of (at least) several wavelengths. The details of the microstructure (unit cell) are very small with respect to the size characterizing the macrostructure which makes it challenging to include them in a full-wave 3D electromagnetic analysis. The microscopic and macroscopic requirements result in a very large computational problem which renders the numerical analysis of the rigorously implemented detailed macrostructure impractical.

Metamaterials based on periodic structures occupy a special niche between homogeneous media and photonic crystals (Fig. 1.1) [9]. Metallic-dielectric resonant structures with dispersive properties contain inclusions and unit-cell sizes of the order of the wavelength and fall out of the scope of the traditional homogenization approaches. Moreover, the analytical approaches become increasingly difficult to apply in cases where the scattering elements have complex geometry. As an approximation, an effective medium behavior can be expected if the wavelength in the structure[2] λ_m is large compared with the typical length scale a of the metamaterial (as a rule of thumb, the condition $a < \lambda_\mathrm{m}/4$ is used [10]). However, the wavelength inside the metamaterial can be much smaller than the corresponding free-space wavelength λ_0 when one approaches the resonance frequencies and the magnitude of the real part of the effective refraction index becomes large [11]. Consequently, one cannot know a priori how small the ratio a/λ_0 has to be in order to reach a reasonable effective medium behavior. Therefore, some researchers deduce that it is impossible to introduce effective material parameters over the whole resonant band of a metamaterial, whereas others claim that the effective description can be introduced within a part of the resonant band of the particles[3] [12]. Additional complications in the metamaterial homogenization are caused by the bianisotropic effects. If the basic inclusions do not have required symmetry then significant magnetoelectric couplings may exist, for instance in the case of a typical split ring resonator geometry [13].

The aim of this thesis is to propose an efficient methodology for numerical modeling of metamaterial structures, based on the calculation of homogenized effective material

---

[2] For the index of symbols used in this thesis see p. 109 ff.

[3] In the research related to metamaterials, the term *particle* is equivalent to a metamaterial inclusion (geometry of a metallic scatterer).

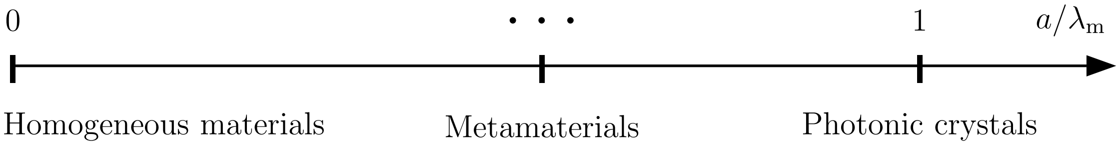

Figure 1.1: Classification of materials according to a/λ_m ratio (a - characteristic size of the structure, e.g. atomic radius, lattice constant, λ_m - wavelength in the medium).

parameters. The simulation approach is based on an example of a negative refraction phenomenon observed experimentally by Shelby *et al.* in a wedge shaped lattice of split ring resonators and wires [14].

1.1.2 Manuscript's Outline

This thesis is organized as follows. In the first chapter, a brief history of artificial media, with the emphasized subsequent steps leading to metamaterials, is presented. It is followed by a short overview of the main milestones and new trends and ideas related to the area of metamaterials research.

Chapter 2 presents Maxwell's equations in continuous and discrete settings. An overview of the Finite Integration Technique used for the solution of the numerical problems throughout this work is given, together with the corresponding time-domain and frequency-domain formulations.

The third chapter discusses the problem of metamaterials homogenization paying particular attention to the identification of metamaterial bianisotropy. The properties of most popular methods used for homogenization, i.e. retrieval from scattering parameters and averaging of electromagnetic fields, are described. The common pitfalls of these methods are discussed and a solution in form of an approach based on the parameter fitting of predefined dispersive models is proposed.

Chapter 4 deals with the Bloch analysis of photonic crystals. The most important tools used for the description of the properties of periodic lattices are introduced, including two- and three-dimensional dispersion diagrams and isofrequency contours. The problem of homogenization of photonic crystals, also beyond the low-frequency limit, is discussed. The Bloch analysis is applied to various metamaterial structures, including a two-dimensional periodic lattice (used in the negative refraction experiment reported in the literature) and metamaterial loaded waveguides (designed and experimentally tested in the frame of this work).

The problem of the interaction of higher order modes in resonant metamaterial structures is outlined in Chapter 5. The concepts of port modes and eigenmodes are clarified, followed by the presentation of a multimode scattering matrix approach. The homogenized description based on the solution of the system's eigenvalue equation is related to the effective model retrieved from single-mode scattering parameters. The multimode scattering matrix is used to indicate the spectral range in which the homogenized metamaterial description is not valid.

Chapter 6 presents simulation results for metamaterial macrostructures implemented in the form of rigorous and effective models. The rigorous implementation of the macrostructure is applied in order to provide reference results, whereas the effective macrostructure is described by the model obtained from the unit-cell analysis conducted in the previous chapters. The results presented in Chapter 6 constitute a validation of the modeling procedure proposed in this work.

The thesis is concluded in Chapter 7 with a summary and an outlook on future work.

1.2 History of Artificial Media

The prospect of designing and controlling electromagnetic properties of a material was always appealing to electrical engineers. The first studies in this area were reported at the end of the 19th century. In 1892 Lord Rayleigh investigated the influence of conducting spheres and cylinders, arranged in a rectangular order, on the effective properties of the medium [15]. In the work published in 1898 J. Bose experimentally demonstrated the rotation of the plane of polarization by man-made twisted structures (jute fibres), that was a precursor of artificial chiral structures by today's definition [16]. A number of works were published in the following decades reporting on, for instance, the rotation of polarization for a linearly polarized wave after propagating through a medium consisting of a collection of randomly oriented small copper helices embedded in cotton balls. This type of bi-isotropic media was studied in 1920s by K. Lindman [17].

The subject was revised and extended in 1940s-50s when W. Kock suggested to use *artificial media* as lightweight beam shaping elements in lens antenna applications [18]. He was probably the one to coin the term *artificial dielectric* which later became established in the microwave literature [19, 20]. In the mid-40s Kock proved experimentally that an array of parallel metal plates illuminated with a low gain radiator shapes the beam pattern in a similar way to a homogeneous dielectric lens characterized by refractive index less than unity. The plate spacing, comparable to the free-space wavelength λ_0, was seen as an effective way to modify the refractive index. The feasible values of the effective refractive index were in the range $0.4 - 0.7$, the structure was strongly dispersive, and its operational bandwidth was rather limited. To overcome the bandwidth limitations, several experimental models for artificial dielectric lenses having refractive indexes larger than unity were introduced [21]. The proposed prototypes included parallel plate lenses, three-dimensional lattice structures built of spheres, disks or strips, and lenses implemented by spraying conductive paint to form different geometries on polystyrene foam and cellophane sheets (Fig. 1.2) [22].

The metallic obstacles were usually supported by a low-density dielectric foam. The medium was capable of behaving identically with the natural dielectrics, but with the advantage of significantly reduced weight. The refractive index could have any desired value (in a certain range) and varied throughout the lens. Furthermore, surface matching was incorporated into the design [23, 24].

In 1960 J. Brown presented a detailed review of the early development steps in the area of artificial dielectrics [25]. The artificial dielectrics were divided into "delay dielectrics" and "phase advance" structures depending on whether the refractive index value was larger or less than unity. At that time, the large aperture antenna lenses, dispersive prisms, polarization filters and transparent to radio waves radome structures were considered as the most prospective microwave applications. Interestingly, Brown noted that the idea of synthesis the artificial dielectrics from conducting elements is a return to the starting point of the classical dielectric theory: in 1850 O. Mossotti developed his dielectric model by postulating that a solid dielectric could be represented as a lattice of conducting spheres [26].

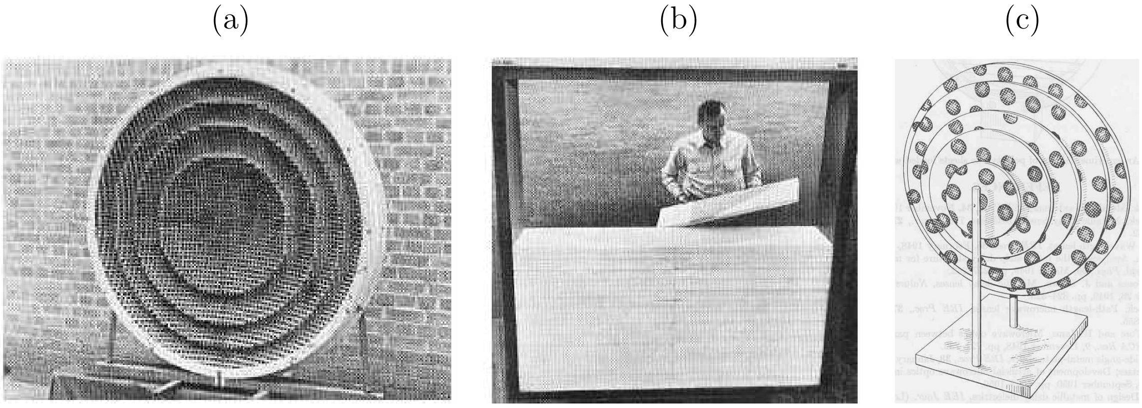

Figure 1.2: Artificial dielectrics lenses. (a) Metal-plate lens (reproduced from [23]). (b) Assembly of a metallic delay lens (reproduced from [23]). (c) Lattice of conducting disks arranged to form a lens. Polystyrene foam sheets support the disks (reproduced from [22]).

In 1962 W. Rotman proposed, that the electric properties of plasma could be imitated with the rodded or parallel plate media, providing rods spacing less than $0.2\lambda_0$, or plate spacing comparable to λ_0, respectively [27]. Extensive waveguide measurements were conducted validating the formulas for the electric characteristics of the rodded media. The measured radiation from an electric aperture covered by a plasma slab, implemented using the rodded and parallel plate media, showed a significant narrowing of the radiated beam. Following these results, the artificial dielectrics in the form of rodded media (called also vividly a "fakir's bed of nails") were commonly used as beam shaping elements in leaky-wave antennas [28] and in the synthesis of surface impedance profiles [29].

The next decades witnessed growing interest in another class of artificial media, namely in *chiral* and *bianisotropic* structures [30–36]. The first definition of chirality came from Lord Kelvin in 1904: "I call any geometrical figure, or group of points, chiral, and say it has chirality, if its image in a plane mirror, ideally realized, cannot be brought to coincide with itself" [37]. The concept of bianisotropic medium, on the other hand, was coined in 1968 by D. Cheng and J. Kong [38, 39], when a suddenly started research boom on electromagnetics of moving media had reached a certain level of maturity [31]. On the level of constitutive relations that characterize bianisotropic and chiral media it is necessary to include cross-coupling terms between the electric and magnetic field excitations and polarization responses (Appendix A).

In chiral media, the special geometrical character of the internal structure (antisymmetry or non-symmetry with respect to mirror reflection, Fig. 1.3a) creates macroscopic effects that are observed as the rotation of the polarization of the propagating field plane due to the magnetoelectric coupling caused by the chiral elements. In classical optics, this phenomenon has been known as *optical activity* since the early 19th century. The potential applications in microwave, millimeter wave and infrared frequencies gave the impetus to the "second wave" of chirality research witnessed in 1990s. The Lindman's experiments with artificial isotropic chiral medium made from randomly dispersed electrically small helices in a host (Fig. 1.3b) were extensively repeated by many research groups leading to several patents granted at that time [40].

At the beginning of this "second wave" of research, the applications of the chiral materials have been seen mainly in the design of antireflection coatings (radar absorbing materials) for reduction of the radar cross-section of aerospace and other vehicles [41]. However, further studies revealed that the introduction of chiral obstacles yields no improvement in the reflection characteristics over the patterns obtained from non-chiral inclusions and that the chiral layers are useless for antireflection coatings purposes [42, 43]. It was identified that the half-wave resonance of the inclusions (and not their handed geometric shape) is the mechanism responsible for observed enhanced absorption [44].

Another potential area of application were the guided-wave structures containing chiral materials (called also *chirowaveguides*), with the coupled TE and TM (hybrid) modes and coupling coefficients proportional to the chirality parameter of the material inside the waveguide [45]. It was postulated that the waveguides loaded with chiral medium could find applications in integrated microwave and optical devices (as directional couplers or switches), optical waveguides, and as substrates or superstrates in planar antennas to reduce the surface-wave power and enhance radiation efficiency (*chirostrip* antennas) [46]. Moreover, it was theoretically shown, that the chirality of the antenna substrate is manifested in the rotation of the radiation pattern around the axis perpendicular to the slab by an angle depending on the chirality parameter, with potential applications in beam-steering systems or simple radiating devices with complex radiation patterns [47].

Since the mid-90s the investigations of chiral materials have been focused on *sculptured thin films*. Sculptured thin films are nanostructured materials with unidirectionally varying properties that can be designed and realized in a controllable manner using physical vapor deposition [48]. Through variation in the direction of the incident vapor flux and substrate rotation during the deposition process, the growth direction of the obtained chiral columnar morphology can be controlled. An example of such a structure in shown in Fig. 1.3c. The interest in chiral sculptured thin films stems from their distinct responses to orthogonal circular polarizations. Within a certain wavelength regime, light of the same handedness as the material is strongly reflected, while the other polarization is mainly transmitted. This phenomenon lead to numerous applications, mainly in linear optics, that started to appear in 1999 [49]. The designed and fabricated structures encompass e.g. circular polarization filters, polarization discriminators, optical fluid sensors and chiral photonic bandgap materials. The prospective applications include optical interconnects (support of propagation modes with different phase velocities in different directions, so-called space-guide concept) and polarization routing (passed and rejected polarizations filtered without loss).

Parallel to the growing interest in the chiral structures, in the late 80s a new class of artificially structured materials was born: *photonic crystals*. In 1987 two milestone papers were published: E. Yablonovitch showed how to use the EM bandgap to control the spontaneous emission of materials embedded within the photonic crystal [50], whereas S. John proposed to use "disordered dielectric microstructures" for the localisation and control of light [51]. The following years have seen an exponential development of research on photonic crystals, summarized in the numerous books [6, 52–58].

Photonic crystals are periodic dielectric or metallic structures (with the lattice constant comparable to the wavelength) that are artificially[4] designed to control and manipulate the propagation of light [52]. A typical photonic crystal can be made either by arranging a lattice of air holes on a transparent background dielectric or by forming a lattice of high refractive index material embedded in a transparent medium with a lower refractive index.

---

[4] Note that the examples of photonic crystals can be found in nature. The photonic crystals give bright colours e.g. to opals, beetles, butterflies, birds, jellyfish [58].

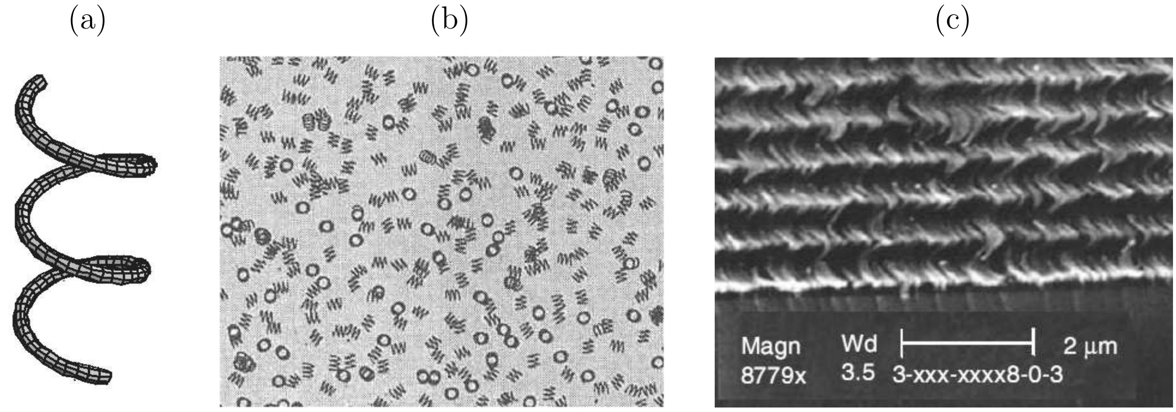

Figure 1.3: Examples of chiral structures. (a) Helix, the most popular chiral particle (adapted from [40]). (b) A manufactured sample of a chiral material (reproduced from [31]). (c) Scanning electron micrograph of a chiral sculptured thin film made of silicon oxide (adapted from [40]).

The idea is to design materials affecting the properties of photons in a similar way as ordinary semiconductor crystals affect the properties of electrons. A photonic crystal could be designed to possess a complete photonic bandgap, i.e. a range of frequencies for which light is forbidden to exist within the interior of the crystal. Most of the applications related to photonic crystals are due to the insertion of defects inside the otherwise periodic structure, analogous to the doping of impurities in semiconductors [59]. A defect in the periodicity leads to localized photonic states in the gap, e.g. a point defect acts like a microcavity (Fig. 1.4a), a line defect like a waveguide (Fig. 1.4b) that allows bending of light through sharp bends with negligible losses (Fig. 1.4c), whereas a planar defect acts like a perfect mirror [60].

The study of the physical and optical properties of photonic crystals has generated new ideas for optical devices and systems. Due to the scaling properties of Maxwell equations, initially the photonic crystals components have been analyzed in the microwave regime, characterized by the relatively easy mode of fabrication and test. These structures included e.g. Y-junctions, directional couplers and Mach-Zehnder interferometers, i.e. the key building blocks enabling almost all applications necessary in optical networks (filters, routers, demultiplexers and power combiners/splitters) [59].

Apart from the above-mentioned microcavities, waveguides and mirrors, the photonic crystal fibres (also called microstructured optical fibres or holey fibres) are likely to become the first application of photonic crystals to the real world of optical communications (Fig. 1.4d) [56]. Some authors point out that photonic crystals may hold the key to the continued progress towards all-optical integrated circuits and could give rise to a technological revolution similar to that caused by semiconductors in the mid 20th century [60].

In 1999 J. Pendry *et al.* proposed, that a microstructure built of non-magnetic conducting sheets in the form of a *split ring resonator* (SRR) could be tuned to negative values of magnetic permeability in a certain frequency range (Fig. 1.5a) [61]. At that time it was already known that a photonic structure consisting of a 3D network of thin wires (Fig. 1.5b) behaves like a plasma characterized by a negative electric permittivity below the plasma frequency [62]. These two properties were combined by D. Smith *et al.*, who demonstrated that a composite medium based on a periodic array of interspaced SRRs and

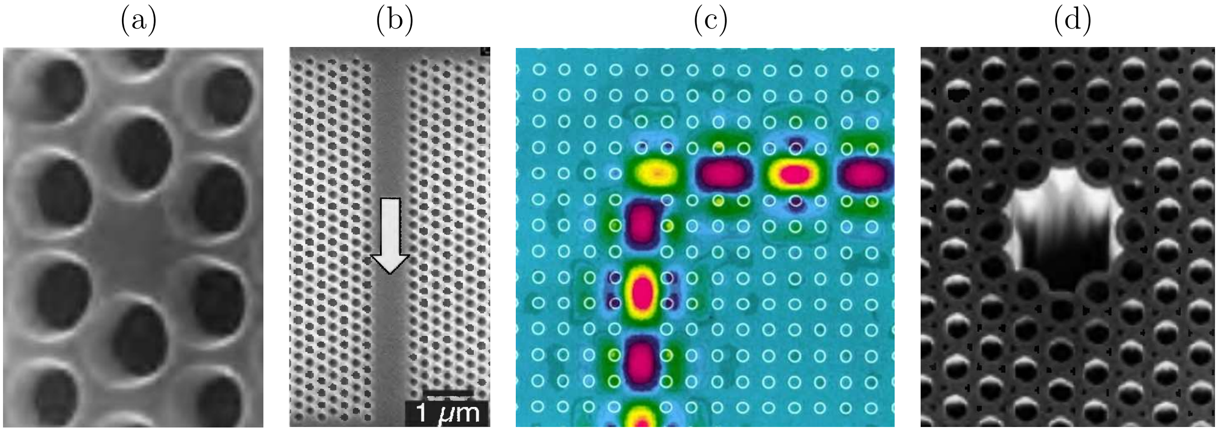

Figure 1.4: Examples of photonic crystals structures. (a) Microcavity formed by a single missing hole (adapted from [6]). (b) Channel optical waveguide fabricated in a 2D photonic crystal (reproduced from [6]). (c) Electric field of light propagating down a waveguide with a sharp bend carved out of a square lattice of dielectric rods. The white circles indicate the positions of the rods (reproduced from [60]). (d) The central part of a microstructured optical fibre with a hollow core. The confinement of light is achieved through a photonic bandgap reflection at the periodic structure which surrounds the central core (adapted from [6]).

wires (Fig. 1.5c) exhibits a frequency region with simultaneously negative values of effective permittivity and permeability [63]. Wave propagation in media with simultaneously negative ε and μ was theoretically analysed in 1968 by V. Veselago, who predicted a number of interesting effects in these media, e.g. negative refraction, reversed Doppler effect or reversed Cerenkov effect [64]. However, due to the lack of a double negative medium in nature, the structure had to be implemented artificially. In 2001 the *negative refraction* phenomenon in a lattice of combined SRRs and wires was experimentally verified [14] and the number of journal and conference papers related to metamaterials started to grow exponentially (see e.g. textbooks [65–70], journals' special issues [71–90] or a new journal focused on metamaterials [91]).

At the moment, there is no universally accepted uniform definition for metamaterials (MTMs) [66]. Most generally, MTMs are understood[5] as artificial structures with unusual properties not observed in the constituent materials and not readily available in nature. Some researchers restrict MTMs to be artificially structured periodic media in which the periodicity is much smaller than the wavelength of the impinging EM wave. The underlying nature of the subwavelength periodic inclusions enables them to act as "artificial molecules" or "atoms" that influence the EM fields in a prescribed manner. This definition of MTMs is directly related to the classical works in artificial dielectrics carried out at microwave frequencies in the mid 20th century. Yet other researchers do not impose strict limits to the size of the constituent unit cells, allowing the period to be of the same order as the signal wavelength and thus extending the definition of MTMs to include structures such as photonic crystals. Others point out, that the periodicity of the "artificial molecules" is not essential, and also a random mixture of complex scatterers can produce emergent properties in the global response of a MTM. Irrespective of the definition, the current

---

[5] For the terminology related to metamaterials and complex EM materials see [92, 93].

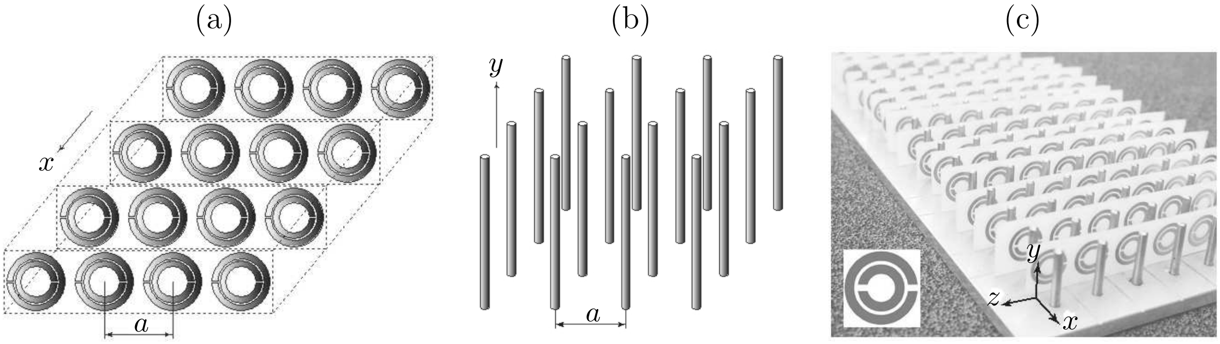

Figure 1.5: Metamaterial structures. (a) Split ring resonators lattice exhibiting negative μ_{eff} if $\vec{H}||x$. (b) Thin wire lattice exhibiting negative ε_{eff} if $\vec{E}||y$. (c) First double negative metamaterial structure constituted of split ring resonators and thin wires. Reproduced from [67].

research clearly favours the periodic structures over the random ones. Therefore, only periodic metamaterials are analysed in this thesis.

The concept of MTMs evolved from artificial dielectrics, chiral structures and photonic crystals. Due to the fact that many MTM implementations show magnetoelectric cross-coupling effects, and principally, can be implemented in the form of a random mixture, the subject of metamaterials simply "swallowed" that of bianisotropy and related topics like chiral and bi-isotropic media [94]. Currently, periodic MTM lattices are being developed parallel to photonic crystals, the difference relying in the EM properties of their unit cells: photonic crystals are composed of conventional, ordinary dielectrics or metals, whereas the functional building blocks of MTMs are engineered to provide tailored properties, e.g. simultaneously negative ε and μ values. However, some of the interesting macroscopic effects observed in MTM arrays arise from their periodicity and have been also observed in the properly designed photonic crystals. Therefore, the MTM structures are closely related to photonic crystals (some of the researchers merge both concepts into *photonic metamaterials* [73,88], whereas others seem to treat the photonic crystals, especially those designed to work in the microwave regime - *electromagnetic bandgap media* - as a subclass of metamaterials [66,68,72,85]).

This section presented a brief history of artificial media in the context of metamaterial structures [93, 94]. For this reason, a lot of topics describing complex media and not directly related to metamaterials are not mentioned. An interested reader is referred to [95] and the references therein for a more comprehensive overview of complex mediums for electromagnetics and optics. Some of the most interesting aspects of the metamaterials research are presented in the following section.

1.3 Milestones in Metamaterials Research

Metamaterials are commonly considered as artificial, effectively homogeneous EM structures with unusual properties not readily available in nature. An effectively homogeneous periodic structure is characterized by the unit-cell size a, which is much smaller than the guided wavelength λ_{m}. If this condition is satisfied the propagated EM wave does not recognize the details of the structure at hand and responds to the effective, macroscopic constitutive parameters, which depend on the nature of the unit cell. The constitutive parameters are the effective relative electric permittivity ε_{eff} and magnetic permeability μ_{eff}, both of which are related to the refractive index n by:

$$n = \pm\sqrt{\varepsilon_{\text{eff}}\ \mu_{\text{eff}}}. \tag{1.1}$$

The four possible sign combinations in the pair $(\varepsilon, \mu \in \mathbb{R})$, i.e. $(+,+)$, $(+,-)$, $(-,+)$, and $(-,-)$, result in a *double positive* (DPS), *single negative* (SNG) or *double negative* (DNG) medium, as illustrated in Fig. 1.6. Whereas the first three combinations are well known in conventional materials, the last one, with simultaneously negative permittivity and permeability, corresponds to the new class of double negative materials. Several fundamental phenomena related to DNG media were predicted by Veselago in 1968 [64, 67]:

- A DNG medium allows the propagation of EM waves with $\vec{E}$, $\vec{H}$ and $\vec{k}$ building a *left-handed* triad ($\vec{E} \times \vec{H}$ antiparallel to $\vec{k}$), compared with a *right-handed* triad ($\vec{E} \times \vec{H}$ parallel to $\vec{k}$) characterizing conventional (DPS) materials[6].
- The phase in a DNG medium propagates backward to the source (backward wave) with the phase velocity opposite (antiparallel) to the group velocity.
- In a medium with negative permittivity and permeability, the index of refraction n given by (1.1) is negative [96].
- A wave incident upon the interface between the DPS and DNG media undergoes negative refraction corresponding to the negative refraction index (a phenomenon called vividly "bending the wave the wrong way").
- The constitutive parameters of a DNG medium have to be dispersive with the frequency dependent ε and μ satisfying the conditions:

  $$\frac{d(\omega\varepsilon)}{d\omega} > 0, \qquad \frac{d(\omega\mu)}{d\omega} > 0. \tag{1.2}$$

  Consequently, ε and μ must be positive in some parts of the spectrum, in order to compensate for their negative values in other frequency regions.

Veselago, the pioneer of the research on DNG media, summarized his early works with the conclusion that a DNG material cannot be found in nature and for more than 30 years no further progress in this area was made.

The breakthrough occurred in 1999 with the work of J. Pendry *et al.* [61], who noticed that a split ring resonator (Fig. 1.7a) with the dimensions much smaller than the free-space wavelength, could respond to microwave radiation of certain polarization as if it had the effective permeability of the form:

$$\mu_{\text{eff}} = 1 - \frac{\frac{\pi r^2}{a^2}}{1 + j\frac{2aR}{\omega r \mu_0} - \frac{3dc_0^2}{\pi\omega^2 \ln(2w/d) r^3}}, \tag{1.3}$$

---

[6] Hence another term used to describe a DNG structure: left-handed medium. This term should not be confused with the handedness property of a chiral medium. On the other hand, a conventional DPS medium is sometimes referred to as a right-handed one.

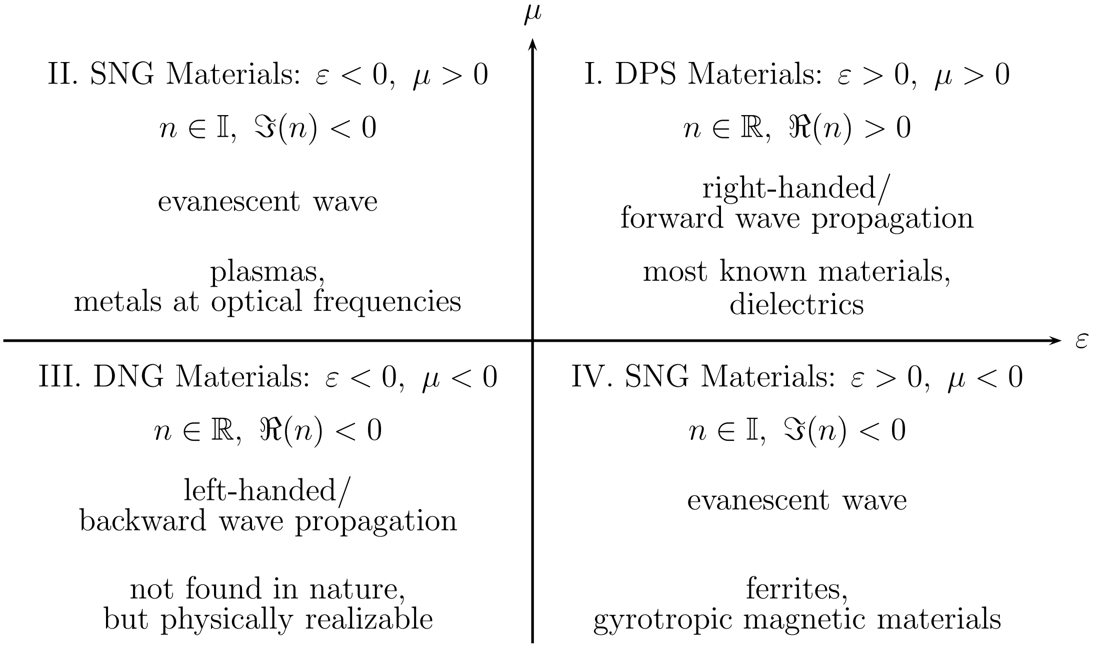

Figure 1.6: Material classification according to ($\varepsilon, \mu \in \mathbb{R}$) pairs, corresponding refractive index n, type of the wave in the medium, and typical examples of the structure.

where R is the resistance of the unit length of the rings, w, d, r are geometrical parameters of the rings and a is the lattice constant. A typical resonant characteristic of $\mu_{\text{eff}}(f)$ is presented in Fig. 1.7b where the frequency region of the negative real part of permeability can clearly be noticed. The microstructure consisting of two concentric metallic split rings was proposed as a lightweight alternative to ferrites, offering the possibility for obtaining customized (including negative) permeability values in a narrow frequency band. When the SRR is excited by a time-varying external magnetic field directed along the x axis, the gaps g on each ring (placed on opposite sides of the SRR) force the electric current to flow from one ring to another across the slot d between them, taking the form of a strong displacement current. The device behaves as a LC circuit driven by an external electromotive force, where C is the distributed capacitance between the rings, and L is the inductance of the rings [97].

On the other hand, although the first results related to negative electric permittivity in artificial materials were reported in 1960s [27], it was the analysis of low frequency plasmons in thin-wire structures published by Pendry *et al.* at the end of 90s that drew the attention of the scientific community[7] to the structures with negative ε_{eff} [62, 99]. It is known that the EM response of metals in the visible and near-ultraviolet part of the spectrum is described by a dielectric function of the form [99]:

$$\varepsilon_{\text{eff}} = 1 - \frac{\omega_p^2}{\omega(\omega - j\nu_c)}, \qquad \omega_p^2 = \frac{n_e e^2}{\varepsilon_0 m_\text{e}}, \tag{1.4}$$

where the parameter ν_c is a damping term representing dissipation, whereas the angular plasma frequency ω_p depends on the density n_e and mass m_e of the electrons e. Pendry showed, that for an artificial material built of very thin metallic wires assembled in a periodic lattice, the effective mass of electrons confined to the wires can be enhanced

---

[7] The author of [27], W. Rotman, characterized the thin wires lattices in terms of a refractive index [98]. It was J. Pendry *et al.*, who attributed effective electric permittivity to these structures.

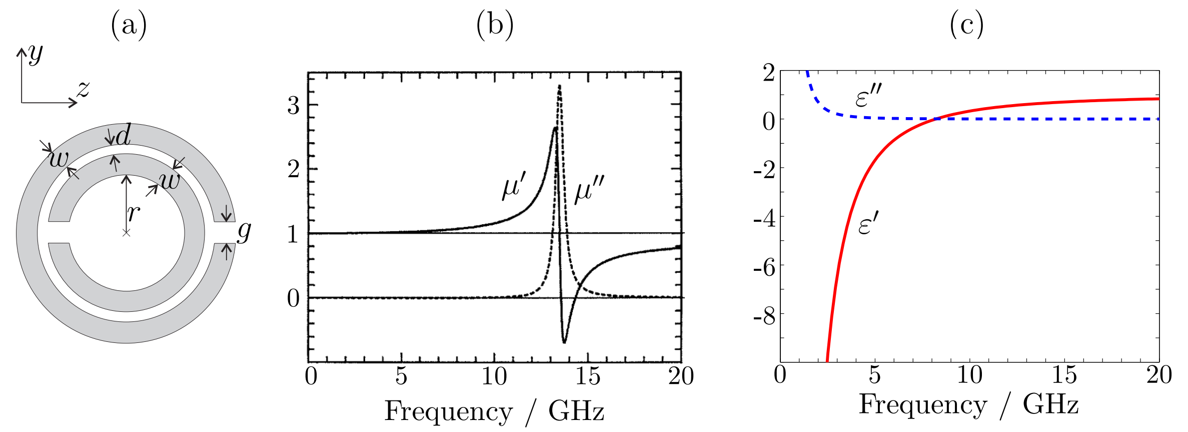

Figure 1.7: (a) Split ring resonator consisted of two metallic rings (adapted from [61]). (b) Effective magnetic permeability of a SRR ($r = 2$ mm, $w = 1$ mm, $d = 0.1$ mm, $a = 10$ mm, $R = 2000\ \Omega$/m; adapted from [61]). (c) Effective electric permittivity of a lattice of thin wires ($r = 10^{-3}$ mm, $a = 5$ mm, $\nu_c = 0.01\omega_p$, plasma frequency 8.2 GHz).

by several orders of magnitude, resulting in the reduction of the plasma frequency from visible and near-ultraviolet to microwave region. The effective electric permittivity of this structure is expressed by (1.4), where the radial plasma frequency and collision frequency are expressed as [99]:

$$\omega_p^2 = \frac{2\pi c_0^2}{a^2 \ln(a/r)}, \qquad \nu_c = \frac{\varepsilon_0 a^2 \omega_p^2}{\pi r^2 \kappa}, \tag{1.5}$$

i.e. ε_{eff} depends on the geometrical parameters of the system - lattice constant a and wire radius r. These results were confirmed experimentally in [62, 100]. A typical characteristic of $\varepsilon_{\text{eff}}(f)$ is presented in Fig. 1.7c.

The results reported by J. Pendry *et al.* regarding negative μ_{eff} from a lattice of SRRs and negative ε_{eff} from a lattice of thin wires were linked together by D. Smith *et al.*, and for the first time an artificial structure characterized by double negative material parameters was proposed [63]. The experimental structure composed of SRRs and metal posts (approximation of wires), providing negative μ_{eff} and ε_{eff}, respectively, is presented in Fig. 1.5c.

D. Smith observed, that the dispersion diagram of a periodic lattice of SRRs is characterized by a band gap in the vicinity of the resonant frequency, implying a region of negative μ_{eff} (Fig. 1.8a). On the other hand, in a medium composed of periodically placed conducting straight wires, there is a single gap in propagation up to a cutoff frequency ω_p (providing that the electric field is polarized along the axis of the wires). When wires are added between the split rings, a passband occurs within the previously forbidden band, indicating that the negative $\varepsilon_{\text{eff}}(f)$ for this region has combined with the negative $\mu_{\text{eff}}(f)$ to allow propagation (Fig. 1.8b).

This prediction was confirmed experimentally [63] and numerically [101, 102] by the measurement and simulation of the transmission through a lattice of SRRs only and a lattice of combined SRRs and wires (Fig. 1.8c). Furthermore, first numerical attempts to describe effective constitutive parameters revealed negative electric permittivity and magnetic permeability of SRR/wire based MTM structures [103, 104].

The milestone in the research of double negative MTMs was a work published by R. Shelby *et al.* in 2001, describing experimental verification of a negative index of refraction

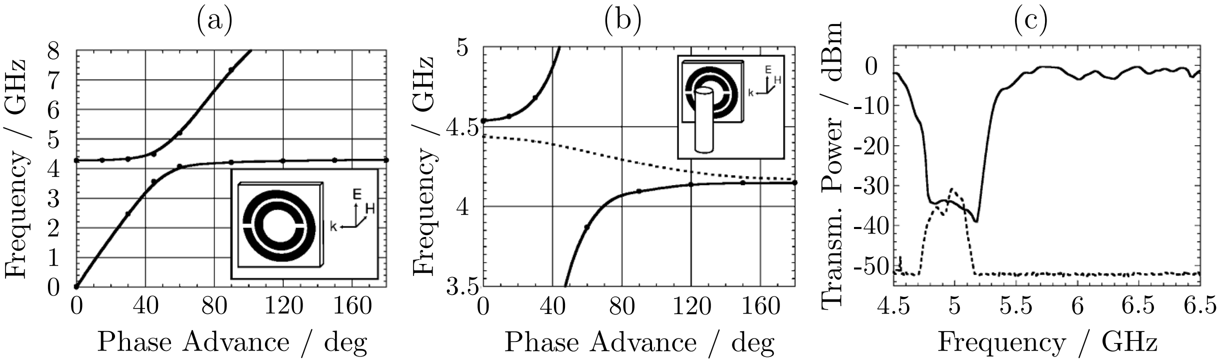

Figure 1.8: (a) Dispersion curve for a lattice of SRRs. The inset shows the orientation of a SRR with respect to the incident radiation. (b) Expanded view of the dispersion curve shown in (a). The dashed line corresponds to SRRs with wires placed uniformly between the rings. (c) Measured transmission for a lattice of SRRs only (solid line) and for SRRs and wires (dashed line). Adapted from [63].

[14]. A MTM sample designed to be double negative in the frequency region 10.2 to 10.8 GHz was assembled from square copper split ring resonators and copper wire strips printed on a circuit board (Fig. 1.9a). To determine the refractive index, the deflection of the beam passing through the boards assembled into a two-dimensional, periodic, wedge-shaped sample was measured. The sample and the microwave absorber were placed between top and bottom parallel aluminum plates and irradiated by a microwave beam (Fig. 1.9b). The incident face of the wedge was illuminated by a beam with an uniform electric field perpendicular to the metal plates and parallel to the wires. After propagating through the sample, the beam encountered the second surface of the wedge, the refraction interface, and was refracted into a direction determined by Snell's law. A microwave detector measured the transmitted power spectrum as a function of the angle from the normal to the wedge interface.

Experiments were performed with a wedge-shaped DNG sample and a similarly shaped Teflon sample. Microwaves were refracted to positive angles for the Teflon sample, whereas for the MTM sample the refraction angle was negative (Fig. 1.9c). At 10.5 GHz, the control sample made of Teflon reported a positive angle of refraction of 27 deg, corresponding to the refractive index of $+1.4$ and calibrating the apparatus. Using the SRR/wire metamaterial, the beam was observed to exit at an angle of -61 deg which yielded an effectively negative index of refraction -2.7. Resonant at 10.5 GHz, the wire and SRR media exhibited a bandwidth of 500 MHz in approximate agreement with the dispersion characteristics predicted by the product of the material parameter expressions of the wire and SRR media (the theoretical and measured index of refraction in function of frequency is presented in Fig. 1.9d).

Following the publication of the negative refraction phenomena, various aspects of the experimental results have been questioned. It was claimed, that for the incidence of a modulated plane wave on an infinite half space of a negative refractive index material, the group refraction is positive even when the phase refraction is negative [105]. This discrepancy was clarified by pointing out that the direction of group velocity is not necessarily parallel to the normal of the interference pattern created (in this case) by two waves of different frequencies [106–109].

Furthermore, critics argued that the experimental detection of the transmitted wave was

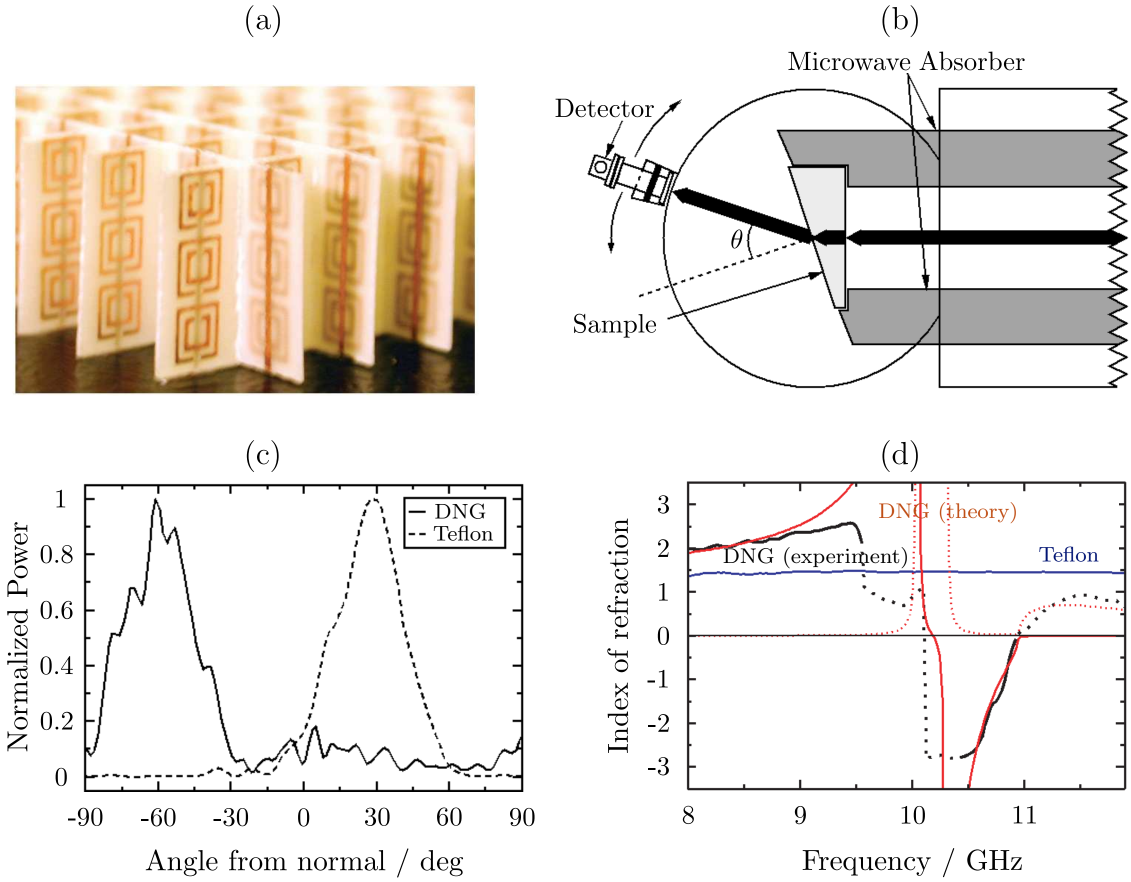

Figure 1.9: (a) DNG metamaterial sample. The rings and wires are on opposite sides of the boards. (b) Top view of the experimental setup. (c) Transmitted power at 10.5 GHz as a function of refraction angle for both a Teflon sample and a DNG sample. (d) Index of refraction vs frequency. Adapted from [14].

done at an intermediate distance to the sample and not in the far field, resulting in a highly ambiguous interpretation of the transmission measurements [110]. Nonetheless, the negative refraction phenomenon has been confirmed in another set of experiments, including the measurement of the EM field profiles at the distance of $28\lambda_0$ [111, 112] and $85\lambda_0$ [113] from the MTM sample. Moreover, numerical simulations of wedge-shaped metamaterials supported the experimental results related to observed negative refraction [114, 115].

Although there are many interesting phenomena related to DNG media, e.g. reversal of Doppler effect, reversal of Cerenkov radiation and negative Goos-Hänchen beam shift, most of them were analysed on the theoretical basis only. The negative refraction experiment had validated the concept of the double negative medium - this brought about revived interest in metamaterials and launched a rapidly growing research area.

1.4 New Trends and Ideas Related to Metamaterials

As mentioned in the previous section, the experimental validation of the negative refraction phenomenon caused a heated discussion in the scientific community. However, apart from the negative refraction, there are many other ideas related to metamaterials[8] that have drawn the attention of scientists and engineers to this field. Several of these new ideas creating the main trends in the current research on MTMs are briefly described in this section.

Perfect Lens

V. Veselago hypothesized, that a medium with a negative refractive index can form a planar lens, i.e. a lens without curved surfaces [64]. The trajectory of each ray that leaves a nearby source is exactly reversed as it enters a $n = -1$ slab, such that all the rays are focused at the centre of the material and then once again on the outside (Fig. 1.10). In 2000, J. Pendry extended the analysis of Veselago's lens, and observed that such lenses could overcome the diffraction limit [116]. Pendry suggested that Veselago's lens would allow perfect imaging if it was completely lossless and its refractive index n was exactly equal to -1 relative to the surrounding medium. The lens achieves imaging with super-resolution by focusing propagating waves, as would a conventional lens, but in addition it supports growing evanescent waves emanating from the source. The restoration of evanescent waves at the image plane allows imaging with super-resolution.

Parallel to the case of negative refraction, the concept of a *perfect lens* was strongly criticised [117–119]; the raised issues, however, were clarified by the author [120–122]. Moreover, the concept of a planar lens made from negative index materials [123] has been experimentally verified, first at microwave frequencies using transmission line structures [124] and resonant composite materials [125], and then in the infrared and optical spectrum, using negative permittivity medium in the form of noble metals layers (silver) or silicon carbide (SiC) compounds [126–128]. The resolution measured at optical frequencies was reported to be in the range of one-sixth of the illumination wavelength [127].

---

[8] Metamaterials can be implemented in the form of planar structures, for example as transmission lines in microstrip technology. This geometries are not analysed in this work. For an overview, see e.g. [67].

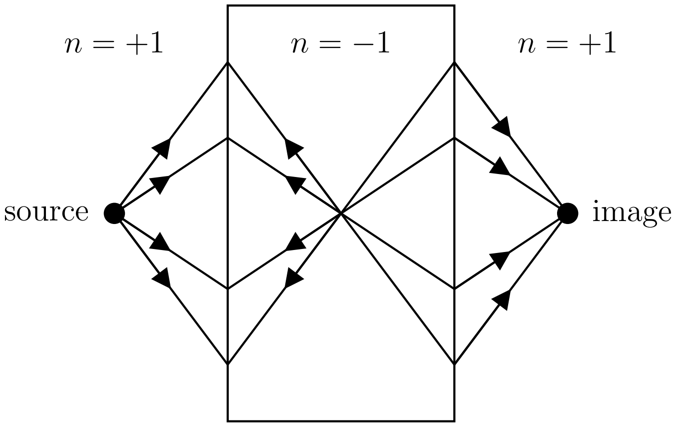

Figure 1.10: Planar lens made of negative refractive index material. The thickness of the lens is half the distance from the source to the image. The arrows show the direction of the wave vector in the medium.

Extreme Parameter Media

The material classification according to permittivity and permeability values presented in Fig. 1.6, allows one to categorize a medium as a double negative, double positive or single negative. However, even for a conventional double positive medium, the permittivity and permeability can be synthesized in a broad range of values. A plane wave propagating in a homogeneous dielectric-magnetic medium can be characterized with the wave impedance $Z = \sqrt{\mu/\varepsilon}$ and the refractive index $n = \sqrt{\mu_{\mathrm{eff}}\,\varepsilon_{\mathrm{eff}}}$. The useful idealized concept in electromagnetics, the perfect electric conductor (PEC) corresponds to $\varepsilon \to \infty, \mu \to 0$ (zero impedance medium), whereas the perfect magnetic conductor (PMC) to $\varepsilon \to 0, \mu \to \infty$ (infinite impedance medium). However, other combinations of either very large or very small values for ε, μ parameters are also possible. It has recently been suggested that materials with such extreme parameters have the potential for interesting applications, e.g. increasing the directivity of planar antennas, cloaking objects, and squeezing EM and optical energy (see e.g. [93] and references therein). The first practical applications of this concept occurred in the microstrip technology of planar circuits, where complementary SRRs etched in the ground plane allowed the realization of impedances not easily achievable through conventional microwave transmission lines [129]. Another area of application is in metamaterial based antenna substrates, e.g. artificial perfect magnetic conductor surfaces (see e.g. [85]).

Electromagnetic Cloak

A new approach to the design of EM structures has recently been proposed, in which the paths of EM waves are controlled within a material by introducing a prescribed spatial variation in the constitutive parameters [130–132]. One possible application of the transform media is that of an *electromagnetic cloak*, i.e. an invisibility device that should guide

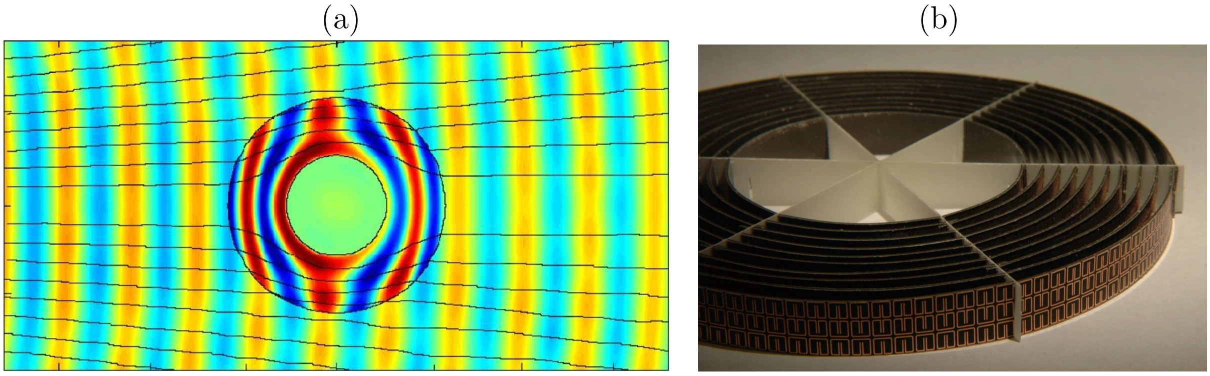

Figure 1.11: (a) Electric field patterns and stream lines indicating the direction of the Poynting vector for the cloak structure. The cloak lies in the region between the black circles and surrounds a copper cylinder at the inner radius. (b) Two dimensional cloaking structure built of ten layers of SRRs. Adapted from [132].

waves around an object as if nothing were there, regardless of where the waves are coming from (Fig. 1.11a). By implementing complex material properties, the concealed volume plus the cloak appear to have properties of free space when viewed externally. The cloak thus neither scatters waves nor imparts a shadow in the transmitted field - either of which would enable the cloak to be detected. Advances in the development of metamaterials with respect to gradient index lenses have made the physical realization of the complex material properties feasible. The EM cloak was implemented in the microwave range by means of 10 layers of SRRs, approximating the optimal magnetic permeability profile with the stepwise values of μ' between 0.1 and 0.3 (structure shown in Fig. 1.11b). Experimental results showed, that the cloak significantly decreases scattering and reduces the shadow of the hidden object (in the described experiment represented by a conducting cylinder), so that the EM behavior of the cloak/object combination resembles that of free space.

Negative Magnetic Permeability at Optical Frequencies

Since the first recipe to design an artificial magnetic material in the form of a SRRs array was suggested by Pendry *et al.* [61] and implemented at X-band frequencies by Smith *et al.* [14, 63], one can observe constant efforts to obtain the negative magnetic permeability at higher frequencies. In the first attempts, the dimensions of SRRs were scaled down and their resonance frequency has been pushed up to 1 THz [133]. Next, it was shown, that double C-shaped SRRs are not required at THz frequencies and the magnetic response of single C-shaped SRRs was demonstrated at 85 THz (3.5 μm) [134]. Further optimization of the structures based on single C-shaped SRRs made it possible to achieve magnetic resonance wavelengths at around 900 nm. Current approaches to create MTMs with a magnetic response in the visible range completely abandoned the classical SRR shape and taken advantage of nanorods, ellipsoidal voids arrays in metal sheets or nano-fishnet (biperiodic cross gratings) structures [135–137].

Chapter 2

Computational Framework

2.1 Analytical Electromagnetics

The electromagnetic fields phenomena are described using a set of equations unified by J.C. Maxwell and reformulated by O. Heaviside and H. Hertz in the second half of the 19th century. Maxwell's equations in the time domain can be denoted in an integral and a differential form as:

$$\oint_{\partial A} \vec{E}(\vec{r},t)\cdot d\vec{s} = -\int_{A} \left(\frac{\partial \vec{B}(\vec{r},t)}{\partial t}\right)\cdot d\vec{A} \;\Leftrightarrow\; \nabla\times\vec{E}(\vec{r},t) = -\frac{\partial \vec{B}(\vec{r},t)}{\partial t}, \tag{2.1}$$

$$\oint_{\partial A} \vec{H}(\vec{r},t)\cdot d\vec{s} = \int_{A} \left(\frac{\partial \vec{D}(\vec{r},t)}{\partial t} + \vec{J}(\vec{r},t)\right)\cdot d\vec{A} \;\Leftrightarrow\; \nabla\times\vec{H}(\vec{r},t) = \frac{\partial \vec{D}(\vec{r},t)}{\partial t} + \vec{J}(\vec{r},t), \tag{2.2}$$

$$\int_{\partial V} \vec{D}(\vec{r},t)\cdot d\vec{A} = \int_{V} \rho(\vec{r},t)\; dV \;\Leftrightarrow\; \nabla\cdot\vec{D}(\vec{r},t) = \rho(\vec{r},t), \tag{2.3}$$

$$\int_{\partial V} \vec{B}(\vec{r},t)\cdot d\vec{A} = 0 \;\Leftrightarrow\; \nabla\cdot\vec{B}(\vec{r},t) = 0, \tag{2.4}$$

for all $A, V \in \mathbb{R}^3$. $\vec{E}$ ($\vec{H}$) refers to the electric (magnetic) field intensity, $\vec{D}$ ($\vec{B}$) is the electric (magnetic) flux density, $\vec{J}$ the electric current density and ρ the electric charge density. The electric current density can be expressed as:

$$\vec{J}(\vec{r},t) = \vec{J}_l(\vec{r},t) + \vec{J}_e(\vec{r},t) + \vec{J}_k(\vec{r},t), \tag{2.5}$$

where $\vec{J}_l$ represents a conduction current density, $\vec{J}_e$ an externally imposed current density and $\vec{J}_k$ a convection current density.

The frequency domain computation is based on the analysis of EM fields at one specific frequency, assuming harmonic time dependence. The steady-state sinusoidal fields and fluxes f are represented by complex phasors $\underline{f}$, i.e.:

$$f(\vec{r},t) \;=\; \Re\{\underline{f}(\vec{r})e^{j\omega t}\}, \tag{2.6}$$

leading to the time derivative being a multiplication of the phasor by the factor $j\omega$:

$$\frac{d}{dt}f(\vec{r},t) \;=\; \Re\{j\omega\underline{f}(\vec{r})e^{j\omega t}\}. \tag{2.7}$$

Maxwell's equations in the differential phasor form become:

$$\begin{aligned}\nabla \times \vec{E}(\vec{r}) &= -j\omega\vec{B}(\vec{r}), && (2.8)\\ \nabla \times \vec{H}(\vec{r}) &= j\omega\vec{D}(\vec{r}) + \vec{J}(\vec{r}), && (2.9)\\ \nabla \cdot \vec{D}(\vec{r}) &= \rho(\vec{r}), && (2.10)\\ \nabla \cdot \vec{B}(\vec{r}) &= 0. && (2.11)\end{aligned}$$

The constitutive relations (relating the flux densities to the field intensities) and Ohm's law in the frequency domain for linear, inhomogeneous, dispersive, bianisotropic media at rest have the form:

$$\begin{aligned}\vec{D}(\vec{r},\omega) &= \overset{\leftrightarrow}{\varepsilon}(\vec{r},\omega)\vec{E}(\vec{r},\omega) + \overset{\leftrightarrow}{\xi}(\vec{r},\omega)\vec{H}(\vec{r},\omega), && (2.12)\\ \vec{B}(\vec{r},\omega) &= \overset{\leftrightarrow}{\mu}(\vec{r},\omega)\vec{H}(\vec{r},\omega) + \overset{\leftrightarrow}{\zeta}(\vec{r},\omega)\vec{E}(\vec{r},\omega), && (2.13)\\ \vec{J}(\vec{r},\omega) &= \overset{\leftrightarrow}{\kappa}(\vec{r},\omega)\vec{E}(\vec{r},\omega), && (2.14)\end{aligned}$$

where $\overset{\leftrightarrow}{\varepsilon}$ denotes the electric permittivity, $\overset{\leftrightarrow}{\mu}$ magnetic permeability and $\overset{\leftrightarrow}{\kappa}$ conductivity of the medium. The magnetoelectric parameters $\overset{\leftrightarrow}{\xi}$ and $\overset{\leftrightarrow}{\zeta}$ describe the cross-polarizability effects in the medium. Neglecting the magnetoelectric couplings, the constitutive relations for the anisotropic medium take the form:

$$\begin{pmatrix} D_x(\vec{r},\omega)\\ D_y(\vec{r},\omega)\\ D_z(\vec{r},\omega)\end{pmatrix} = \varepsilon_0 \begin{pmatrix} \varepsilon_{xx}(\vec{r},\omega) & \varepsilon_{xy}(\vec{r},\omega) & \varepsilon_{xz}(\vec{r},\omega)\\ \varepsilon_{yx}(\vec{r},\omega) & \varepsilon_{yy}(\vec{r},\omega) & \varepsilon_{yz}(\vec{r},\omega)\\ \varepsilon_{zx}(\vec{r},\omega) & \varepsilon_{zy}(\vec{r},\omega) & \varepsilon_{zz}(\vec{r},\omega)\end{pmatrix} \begin{pmatrix} E_x(\vec{r},\omega)\\ E_y(\vec{r},\omega)\\ E_z(\vec{r},\omega)\end{pmatrix}, \quad (2.15)$$

$$\begin{pmatrix} B_x(\vec{r},\omega)\\ B_y(\vec{r},\omega)\\ B_z(\vec{r},\omega)\end{pmatrix} = \mu_0 \begin{pmatrix} \mu_{xx}(\vec{r},\omega) & \mu_{xy}(\vec{r},\omega) & \mu_{xz}(\vec{r},\omega)\\ \mu_{yx}(\vec{r},\omega) & \mu_{yy}(\vec{r},\omega) & \mu_{yz}(\vec{r},\omega)\\ \mu_{zx}(\vec{r},\omega) & \mu_{zy}(\vec{r},\omega) & \mu_{zz}(\vec{r},\omega)\end{pmatrix} \begin{pmatrix} H_x(\vec{r},\omega)\\ H_y(\vec{r},\omega)\\ H_z(\vec{r},\omega)\end{pmatrix}. \quad (2.16)$$

For the isotropic medium the permittivity and permeability tensors reduce to scalars:

$$\begin{aligned}\vec{D}(\vec{r},\omega) &= \varepsilon(\vec{r},\omega)\vec{E}(\vec{r},\omega), && (2.17)\\ \vec{B}(\vec{r},\omega) &= \mu(\vec{r},\omega)\vec{H}(\vec{r},\omega), && (2.18)\end{aligned}$$

where ε and μ are complex quantities described as:

$$\begin{aligned}\varepsilon(\vec{r},\omega) &= \varepsilon_0(\varepsilon'(\vec{r},\omega) - j\varepsilon''(\vec{r},\omega)), && (2.19)\\ \mu(\vec{r},\omega) &= \mu_0(\mu'(\vec{r},\omega) - j\mu''(\vec{r},\omega)). && (2.20)\end{aligned}$$

Dispersive Models

The physics of dispersion is typically illustrated by a simple classical model for the response of a medium to a time-dependent EM field. Under the influence of the EM field charges are perturbed from their equilibrium positions. The motion of an electron (charge $-e$) bound by a harmonic force and acted on by an electric field[1] $\vec{E}(t)$ is described by the damped harmonic oscillator equation [1]:

$$m\left(\frac{d^2\vec{r}}{dt^2} + \delta\frac{d\vec{r}}{dt} + \omega_0^2\vec{r}\right) = -e\vec{E}(t), \quad (2.21)$$

---

[1] The velocities v of the motion of the electrons in the atoms are small compared with the velocity of light [138]. Thus, in the Lorentz force equation one may approximate the force on an electron as $\vec{F} = -e(\vec{E} + \vec{v} \times \vec{B}) \approx -e\vec{E}$ [139].

where m is the mass of the charge, ω_0 the frequency of oscillation about equilibrium and δ the damping constant of the oscillator model. If the field varies harmonically in time with the frequency ω, the corresponding dipole moment $\vec{p}$ is given by:

$$\vec{p} = -e\vec{r} = \frac{e^2/m}{\omega_0^2 + j\omega\delta - \omega^2}\vec{E}. \tag{2.22}$$

If there are N molecules per unit volume with a single electron per molecule, then the electric permittivity is described as [1]:

$$\varepsilon(\omega) = \varepsilon_0 + \frac{Ne^2/m}{\omega_0^2 + j\omega\delta - \omega^2}, \tag{2.23}$$

which is equivalent to the single resonance dispersive Lorentz model [5]:

$$\frac{\varepsilon(\omega)}{\varepsilon_0} = \varepsilon_\infty + \frac{\omega_p^2}{\omega_0^2 + j\omega\delta - \omega^2}, \tag{2.24}$$

where ω_p denotes the angular plasma frequency and ε_∞ the high-frequency permittivity of the material.

The classical Lorentz model of dielectric dispersion due to resonance polarization is of fundamental importance in solid state physics and optics. It provides e.g. accurate description of both normal and anomalous dispersion phenomena in the electromagnetic spectrum from the far infrared up to the near ultraviolet [140]. The model is causal and characterized by a frequency band of anomalous dispersion with high absorption, surrounded by lower and higher frequency regions exhibiting normal dispersion with small absorption.

A special case of the Lorentz model is the Drude model[2], used to describe the optical properties of metals. It comes from (2.24) by letting electrons be free and setting the resonance frequency to zero [5]:

$$\frac{\varepsilon(\omega)}{\varepsilon_0} = \varepsilon_\infty - \frac{\omega_p^2}{\omega^2 - j\omega\delta}. \tag{2.25}$$

In this model, the motion of a single electron in a metal exposed to an electric field is assumed to be the result of two opposite forces: the force associated with the electric field itself and a damping force associated with the collisions occuring in the metallic lattice[3] [6]. The Drude model describes also a neutral non-collisional plasma that presents a negative electric permittivity at frequencies lower than the plasma oscillation frequency.

The dispersive Lorentz model satisfies the conditions of passivity and causality that have to be fulfilled by the constitutive parameters of physical media [138].

The condition of passivity implies, that due to energy conservation the signs of ε'' and μ'' should always be positive, or, equivalently, imaginary parts of electric permittivity and

---

[2] Another special case is the Debye model, for an overview see e.g. [5].

[3] Collisions in the Drude model are instantaneous events that abruptly alter the velocity of an electron. Drude attributed them to the electrons bouncing off the impenetrable ion cores. However, it was found later that this simple mechanical picture of an electron bumping along from ion to ion is misleading and should be avoided. However, a qualitative (and often a quantitative) understanding of metallic conduction can be achieved by simply assuming that there is a scattering mechanism, i.e. one can continue to calculate with the Drude model without any precise understanding of the cause of collisions. For the thorough discussion see [141].

magnetic permeability should always be negative, for all materials and at all frequencies $\omega \neq 0$. The imaginary parts of ε and μ corresponding to electric and magnetic losses determine the absorption (dissipation) of energy in matter that always occurs to some extent in a variable EM field. On the other hand, the signs of the real parts of ε and μ for $\omega \neq 0$ are subject to no physical restriction. As $\omega \to 0$, the function $\varepsilon(\omega)$ in dielectrics tends to the electrostatic permittivity, whereas in conductors to an imaginary term expressed in function of the conductivity for steady currents. In the limit as $\omega \to \infty$, the function $\varepsilon(\omega)$ tends to unity (when the field changes sufficiently rapidly, the polarization processes responsible for the difference between the field $\vec{E}$ and the induction $\vec{D}$ cannot occur at all). Similarly, in the high-frequency limit, magnetic permeability $\mu = 1$.

The condition of causality implies that the response of the matter to an excitation cannot precede the cause [5]. A consequence of the causality principle are Kramers-Kronig equations that relate the real and imaginary parts of constitutive parameters for linear and passive media [1, 138]:

$$\varepsilon'(\omega) = 1 - \frac{1}{\pi} \mathrm{PV}\int_{-\infty}^{\infty} \frac{\varepsilon''(\omega')}{\omega' - \omega}\, d\omega', \tag{2.26}$$

$$\varepsilon''(\omega) = \frac{1}{\pi} \mathrm{PV}\int_{-\infty}^{\infty} \frac{\varepsilon'(\omega') - 1}{\omega' - \omega}\, d\omega', \tag{2.27}$$

where PV denotes principal value of the integral. Kramers-Kronig relations are central to the analysis of optical experiments on solids - empirical knowledge of $\varepsilon''(\omega)$ from absorption studies allows the calculation of the corresponding $\varepsilon'(\omega)$ characteristic[4] [1].

The theoretical analysis of the field energy in dispersive media indicates that the following relations hold [138]:

$$\frac{d(\omega\varepsilon)}{d\omega} > 0, \qquad \frac{d(\omega\mu)}{d\omega} > 0. \tag{2.28}$$

In the region of negligible losses permittivity and permeability are monotonically increasing functions of frequency (normal dispersion), i.e. $d\varepsilon'/d\omega > 0$ or $d\mu'/d\omega > 0$ [138]. In the case of a small absorption extending over a sufficiently wide range of frequencies, the real part of permittivity (permeability) passes through zero [138]. Anomalous dispersion characterized by $d\varepsilon'/d\omega < 0$ or $d\mu'/d\omega < 0$ is observed in the neighbourhood of a resonant frequency [1].

2.2 Discrete Electromagnetics

The analytical solution of Maxwell's equations can be obtained only for a limited range of electromagnetic problems involving simple geometrical structures. In most practical cases the only option to solve Maxwell equations is by using numerical methods. For this purpose, the Finite Integration Technique (FIT) implemented in the software package CST Microwave Studio [142] is used throughout this work. The FIT was proposed in 1977 by T. Weiland [143] and was later completed to a generalized scheme for the solution of electromagnetic problems in a discrete space.

---

[4] Kramers-Kronig relations are also applicable (with slight changes) to magnetic permeability, see [138].

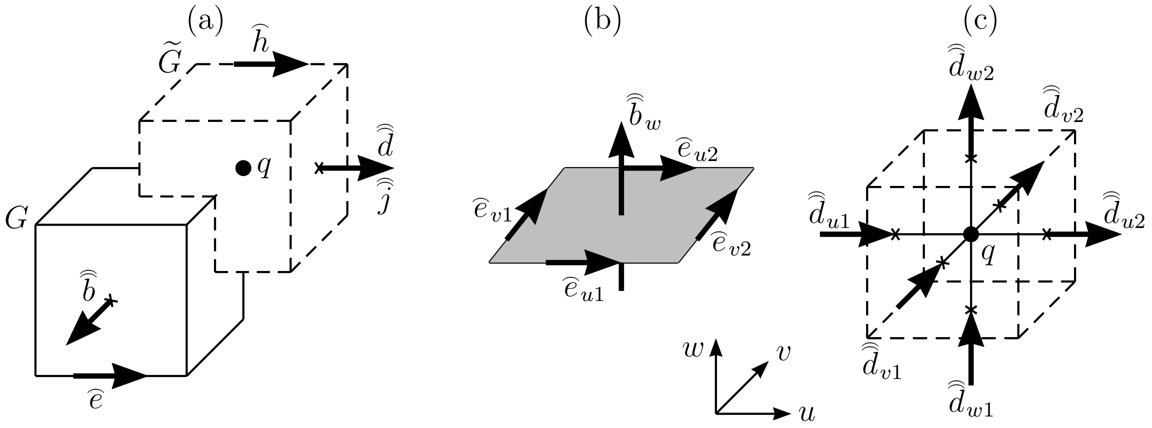

Figure 2.1: Primary (solid line) and dual (dashed line) FIT grids. (a) Allocation of state variables. (b) Discretization of Faraday's law (Eq. 2.1). (c) Discretization of Gauss' law (Eq. 2.3).

Maxwell's Grid Equations

In FIT, Maxwell's equations and the constitutive relations are mapped onto a dual-orthogonal, staggered grid system $\{G, \widetilde{G}\}$, defining a finite computational domain. The procedure of mapping the physical quantities from the continuous space to a discrete subspace defined on a grid is called discretization. The discretization is performed using integral state variables referred to as electric (magnetic) grid voltage $\widehat{e}_i$ ($\widehat{h}_i$), electric (magnetic) grid flux $\widehat{\widehat{d}}_i$ ($\widehat{\widehat{b}}_i$), electric grid current $\widehat{\widehat{j}}_i$, and electric grid charge q_i:

$$\widehat{e}_i(t) = \int_{L_i} \vec{E}(\vec{r},t)\cdot d\vec{s}, \tag{2.29}$$

$$\widehat{h}_i(t) = \int_{\widetilde{L}_i} \vec{H}(\vec{r},t)\cdot d\vec{s}, \tag{2.32}$$

$$\widehat{\widehat{d}}_i(t) = \int_{\widetilde{A}_i} \vec{D}(\vec{r},t)\cdot d\vec{A}, \tag{2.30}$$

$$\widehat{\widehat{b}}_i(t) = \int_{A_i} \vec{B}(\vec{r},t)\cdot d\vec{A}, \tag{2.33}$$

$$\widehat{\widehat{j}}_i(t) = \int_{\widetilde{A}_i} \vec{J}(\vec{r},t)\cdot d\vec{A}, \tag{2.31}$$

$$q_i(t) = \int_{\widetilde{V}_i} \rho(\vec{r},t)\; dV, \tag{2.34}$$

where symbols L_i ($\widetilde{L}_i$) denote the edges, A_i ($\widetilde{A}_i$) the facets and V_i ($\widetilde{V}_i$) the cell volumes allocated on the primary (dual) grid G ($\widetilde{G}$). The allocation of the state variables in the grid space is shown in Fig. 2.1.

Using the definitions of state variables (2.29)-(2.34), Maxwell's equations are transformed into a set of matrix-vector equations, referred to as *Maxwell's Grid Equations* (MGE):

$$\mathbf{C}\widehat{\mathbf{e}} = -\frac{d}{dt}\widehat{\widehat{\mathbf{b}}}, \tag{2.35}$$

$$\widetilde{\mathbf{C}}\widehat{\mathbf{h}} = \frac{d}{dt}\widehat{\widehat{\mathbf{d}}} + \widehat{\widehat{\mathbf{j}}}, \tag{2.36}$$

$$\widetilde{\mathbf{S}}\widehat{\widehat{\mathbf{d}}} = \mathbf{q}, \tag{2.37}$$

$$\mathbf{S}\widehat{\widehat{\mathbf{b}}} = 0. \tag{2.38}$$

The sparse matrix $\mathbf{C}$ ($\widetilde{\mathbf{C}}$) is the discretization of the curl operator, whereas the matrix $\mathbf{S}$

($\widetilde{\mathbf{S}}$) is the discrete div operator on the primary (dual) grid. The entries of the curl matrix C_{ji} ($\tilde{C}_{ji}$) are ± 1 only if boundary of facet A_j ($\tilde{A}_j$) contains edge L_i ($\tilde{L}_i$). Analogously, the entries of the div matrix S_{kj} ($\tilde{S}_{kj}$) are ± 1 only if facet A_j ($\tilde{A}_j$) is contained in the boundary of cell k of the primary (dual) grid.

The discrete equivalent of the constitutive relations and Ohm's law for non-bianisotropic media without permanent polarization or magnetization is based on diagonal material matrices ($\mathbf{M}_{\varepsilon}$, $\mathbf{M}_{\mu^{-1}}$, $\mathbf{M}_{\kappa}$), i.e.:

$$\widehat{\widehat{\mathbf{d}}} = \mathbf{M}_{\varepsilon}\widehat{\mathbf{e}}, \qquad (2.39) \qquad\qquad \widehat{\mathbf{h}} = \mathbf{M}_{\mu^{-1}}\widehat{\widehat{\mathbf{b}}}, \qquad (2.40) \qquad\qquad \widehat{\widehat{\mathbf{j}}}_l = \mathbf{M}_{\kappa}\widehat{\mathbf{e}}. \qquad (2.41)$$

The material matrices are diagonal due to the dual-orthogonality of the grid system, where primary edges and dual facets (or equivalently dual edges and primary facets) intersect with an angle of 90 degrees. The entries of these generalized matrices are defined as:

$$\mathrm{M}_{\varepsilon,ii} = \frac{\widehat{\widehat{\mathrm{d}}}_i}{\widehat{\mathrm{e}}_i} = \frac{\int_{\widetilde{A}_i} \vec{D}\, d\vec{A}}{\int_{L_i} \vec{E}\, d\vec{s}} = \frac{\overline{\varepsilon}\widetilde{A}_i}{L_i}, \tag{2.42}$$

$$\mathrm{M}_{\mu^{-1},ii} = \frac{\widehat{\mathrm{h}}_i}{\widehat{\widehat{\mathrm{b}}}_i} = \frac{\int_{\widetilde{L}_i} \vec{H}\, d\vec{s}}{\int_{A_i} \vec{B}\, d\vec{A}} = \frac{\widetilde{L}_i}{\overline{\mu}A_i}, \tag{2.43}$$

$$\mathrm{M}_{\kappa,ii} = \frac{\widehat{\widehat{\mathrm{j}}}_i}{\widehat{\mathrm{e}}_i} = \frac{\int_{\widetilde{A}_i} \vec{J}\, d\vec{A}}{\int_{L_i} \vec{E}\, d\vec{s}} = \frac{\overline{\kappa}\widetilde{A}_i}{L_i}, \tag{2.44}$$

and describe averaged material coefficients ($\overline{\varepsilon}$ and $\overline{\kappa}$ averaged over dual grid facets $\widetilde{A}_i$, whereas $\overline{\mu}$ averaged over dual grid edges $\widetilde{L}_i$), as well as geometrical dimensions of the particular grid cells [144]. In its standard formulation, FIT is limited to diagonally anisotropic materials (the extension of FIT to general anisotropic, non-magnetoelectric media can be found in [145]).

Time Discretization

The field calculations presented in this thesis are performed in the time as well as frequency domain. The time-domain calculations are based on the leapfrog scheme [146, 147], which samples the values of $\widehat{\mathbf{e}}$ and $\widehat{\widehat{\mathbf{b}}}$ at times separated by half of a time step Δt, i.e. $\widehat{\mathbf{e}}(n\Delta t) = \widehat{\mathbf{e}}^{(n)}$ and $\widehat{\widehat{\mathbf{b}}}((n+1/2)\Delta t) = \widehat{\widehat{\mathbf{b}}}^{(n+1/2)}$. The time allocation of the electric grid voltages and magnetic grid fluxes is shown in Fig. 2.2 corresponding to the substitution in curl equations (2.35)-(2.36) the time derivatives by the central differences:

$$\left(\frac{d}{dt}\widehat{\widehat{\mathbf{b}}}\right)^{(n)} \approx \frac{\widehat{\widehat{\mathbf{b}}}^{(n+\frac{1}{2})} - \widehat{\widehat{\mathbf{b}}}^{(n-\frac{1}{2})}}{\Delta t}, \tag{2.45}$$

$$\left(\frac{d}{dt}\widehat{\mathbf{e}}\right)^{(n+\frac{1}{2})} \approx \frac{\widehat{\mathbf{e}}^{(n+1)} - \widehat{\mathbf{e}}^{(n)}}{\Delta t}. \tag{2.46}$$

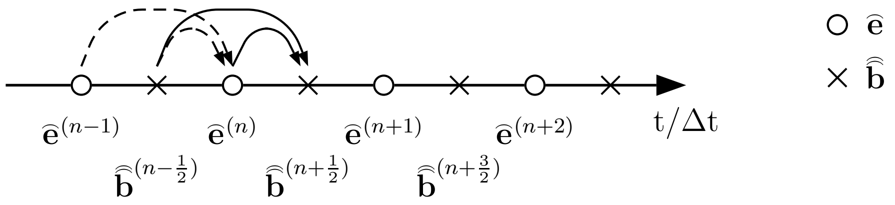

Figure 2.2: The leapfrog scheme for the computation of electric grid voltage and magnetic grid flux in time domain. Each quantity is updated based on the previously computed values of both quantities.

Introducing the central differences in the curl MGE, the updating scheme for the state variables in FIT takes the following form (lossless case):

$$\widehat{\widehat{\mathbf{b}}}^{(n+\frac{1}{2})} = \widehat{\widehat{\mathbf{b}}}^{(n-\frac{1}{2})} - \Delta t \mathbf{C} \widehat{\mathbf{e}}^{(n)}, \tag{2.47}$$

$$\widehat{\mathbf{e}}^{(n+1)} = \widehat{\mathbf{e}}^{(n)} + \Delta t \mathbf{M}_{\varepsilon}^{-1} \left(\widetilde{\mathbf{C}} \mathbf{M}_{\mu^{-1}} \widehat{\widehat{\mathbf{b}}}^{(n+\frac{1}{2})} - \widehat{\widehat{\mathbf{j}}}^{(n+\frac{1}{2})} \right). \tag{2.48}$$

The leapfrog scheme is conditionally stable - the time step Δt is related to the largest eigenvalue (λ_G) of the iteration matrix:

$$\lambda_G = 1 - \frac{(\omega \Delta t)^2}{2} \pm \sqrt{\left(1 - \frac{(\omega \Delta t)^2}{2}\right)^2 - 1}, \tag{2.49}$$

where ω corresponds to the largest eigenvalue of the system matrix [144]. To guarantee the stability of the time-domain solution λ_G has to fulfill the condition:

$$\lambda_G \leq 1. \tag{2.50}$$

Frequency-Domain Formulation

Applying the phasor notation to MGE, the curl equations (2.35)-(2.36) are represented in frequency domain as:

$$\mathbf{C} \underline{\widehat{\mathbf{e}}} = -j\omega \underline{\widehat{\widehat{\mathbf{b}}}}, \tag{2.51}$$

$$\widetilde{\mathbf{C}} \underline{\widehat{\mathbf{h}}} = j\omega \underline{\widehat{\widehat{\mathbf{d}}}} + \underline{\widehat{\widehat{\mathbf{j}}}}, \tag{2.52}$$

whereas the div equations (2.37)-(2.38) are not changed, as they do not contain temporal derivatives. The conduction current ($\underline{\widehat{\widehat{\mathbf{j}}}}_l = \mathbf{M}_{\kappa} \underline{\widehat{\mathbf{e}}}$) can be separated from the imposed one ($\underline{\widehat{\widehat{\mathbf{j}}}}_e$) and the finite conductivity incorporated into the complex permittivity matrix $\underline{\mathbf{M}}_{\varepsilon}$:

$$j\omega \underline{\widehat{\widehat{\mathbf{d}}}} + \underline{\widehat{\widehat{\mathbf{j}}}} = j\omega \left(\mathbf{M}_{\varepsilon} + \frac{1}{j\omega} \mathbf{M}_{\kappa} \right) \underline{\widehat{\mathbf{e}}} + \underline{\widehat{\widehat{\mathbf{j}}}}_e = j\omega \underline{\mathbf{M}}_{\varepsilon} \underline{\widehat{\mathbf{e}}} + \underline{\widehat{\widehat{\mathbf{j}}}}_e. \tag{2.53}$$

Taking into account the material relations and substituting the magnetic flux in the curl MGE (2.51), the discrete wave equation of FIT for the electric field is obtained:

$$\left(\widetilde{\mathbf{C}} \mathbf{M}_{\mu^{-1}} \mathbf{C} - \omega^2 \underline{\mathbf{M}}_{\varepsilon} \right) \underline{\widehat{\mathbf{e}}} = -j\omega \underline{\widehat{\widehat{\mathbf{j}}}}_e, \tag{2.54}$$

called also *curl-curl equation*, due to the double application of the curl operator. In the special case of no excitation ($\underline{\widehat{\widehat{\mathbf{j}}}}_e = 0$), the curl-curl equation is equivalent to the eigenvalue equation of the system, which in the lossless case takes the form:

$$\left(\mathbf{M}_{\varepsilon}^{-1}\widetilde{\mathbf{C}}\mathbf{M}_{\mu^{-1}}\mathbf{C}\right)\underline{\widehat{\mathbf{e}}} \;=\; \omega^2\underline{\widehat{\mathbf{e}}}, \tag{2.55}$$

and whose eigenvalues represent the resonance frequencies of the system, whereas eigenvectors are corresponding electric field solutions (eigenmodes). The problems (2.54) and (2.55) are typically solved using iterative methods (for an overview see e.g. [144]).

Boundary Conditions

The numerical solution of MGE requires a finite computational domain. To limit the numerical space, proper boundary conditions are needed. The types of boundary conditions used throughout this study are briefly described in this section.

The electric and magnetic boundary conditions correspond to enclosing the computational domain with a perfect electric conductor or a perfect magnetic conductor, respectively. At electric walls the tangential components of $\vec{E}$ are shorted out and the normal components of $\vec{B}$ vanish. The FIT implementation of the electric boundary condition relies on setting the columns and rows of the curl matrix $\mathbf{C}$, corresponding to tangential $\widehat{\mathbf{e}}$ and normal $\widehat{\widehat{\mathbf{b}}}$ at the boundary, to zero values. On the other hand, at magnetic walls the tangential components of $\widehat{\mathbf{h}}$ and normal components of $\widehat{\widehat{\mathbf{d}}}$ vanish. The FIT implementation is based on the integration of the Ampere's law over a half of the tangentially oriented boundary facet $\widetilde{A}_i$, where the $\widehat{\mathbf{h}}$ tangential to the boundary is assumed to be zero. An alternative approach takes advantage of the integration over virtually extended dual grid boundary cells and the symmetry condition for tangential $\widehat{\mathbf{h}}$ at magnetic boundary [144].

Periodic boundary condition (PBC) connects two opposite boundaries with a defined phase shift and the calculation domain is simulated as periodically expanded in the given direction. In FIT, the boundary field components located on one side of the computational domain are replaced by the components located on the opposite side of the domain and multiplied by a complex phase factor $e^{j\varphi}$ corresponding to the periodic direction of the structure [148].

Open boundary condition is based on a perfectly matched layer (PML) that absorbs EM waves travelling towards boundaries [149]. The absorbing layers are characterized by electric and (virtual) magnetic conductivities, gradually increasing from zero at the interior interface to certain values at the outer side of the PML. The conductivities represent loss parameters and control the wave attenuation rate in the PML, according to a chosen profile. In order to minimize reflections, several layers are commonly used. A brief description of a PML implementation in FIT can be found e.g. in [150].

Waveguide port boundary condition is based on the quasi-infinite, homogeneous waveguide connected to the boundary of the structure [150]. The ports are typically used to feed the structure with power and to absorb the returning power. The exchange of the EM energy between the structure and the outside space takes place through a discrete number of the orthonormal waveguide modes, obtained from the solution of a two-dimensional eigenvalue problem at the plane of the port. The modes are chosen according to their significant contribution to the field distribution in the waveguide. When a particular mode is not considered by the boundary operator, it undergoes total reflection from the boundary. This undesirable effect can be avoided, when an absorbing boundary operator is applied to the field distribution that remains after subtraction of all considered modes. Waveguide ports are commonly used to the simulation of scattering parameters.

Chapter 3

Homogenization of Metamaterials

The most general description of a linear medium (2.12)-(2.13) requires the determination of 36 frequency dependent, complex constitutive parameters. The extraction of this large number of coefficients is complicated and not required for most of the practical metamaterial structures. The retrieval techniques used for the extraction of effective material parameters typically require certain knowledge of the electromagnetic behavior of the system under consideration, neglecting, for instance, the magnetoelectric coupling effects. The metamaterial homogenization methods are discussed in this chapter with the particular attention paid to the bianisotropic effects, crucial for the extraction of unambiguous constitutive parameters.

3.1 Bianisotropy: How to Recognize It

Most methods for the extraction of effective material parameters neglect the magnetoelectric couplings. On the one hand this significantly simplifies the analysis, but on the other hand it may lead to ambiguous constitutive parameters, should the bianisotropic effects take place in the structure. Therefore, it is of utmost importance to identify if the MTM under test is bianisotropic or not.

The existence of magnetoelectric coupling in a metamaterial (or lack thereof), and consequently, the form of corresponding constitutive relations, are determined from point group theoretical methods based on the symmetries of the underlying resonant particles [151]. A systematic analysis of the symmetries for both constitutive elements and lattices was presented recently in [152].

As a rule of thumb, to avoid the coupling of the electric field to the magnetic resonance of the circular current in the split ring resonator, a mirror symmetry of the SRR plane with respect to the orientation of the electric field should be provided. The problem of magnetoelectric coupling can be easily avoided in 1D and certain 2D (e.g. for 1D propagation with arbitrary polarization, 2D propagation with fixed polarization) metamaterials. For an isotropic 3D material with arbitrary direction and polarization of the incident wave the lack of magnetoelectric coupling can be guaranteed by the inversion symmetry of the design [153].

As an example, let us consider the topologies of edge-coupled and broadside-coupled split ring resonators (EC-SRR, BC-SRR), shown in Fig. 3.1. For the propagation of a quasi-TEM wave in a 2D metamaterial, four different cases of the EC-SRR orientation are shown in Fig. 3.2, equivalent to the following field components and propagation directions [69]:

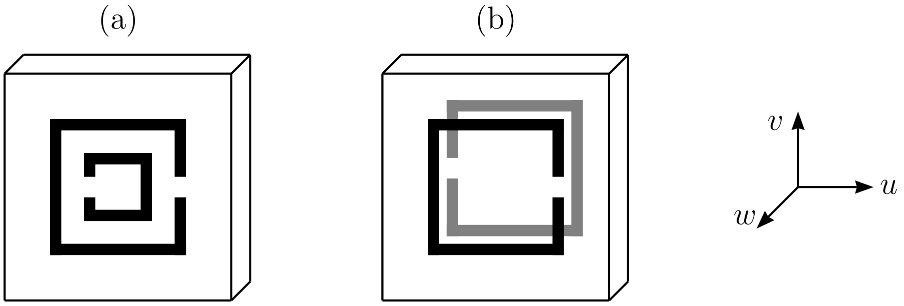

Figure 3.1: Topologies of (a) edge-coupled and (b) broadside-coupled split ring resonators. The conducting rings (copper) are placed on (a) single or (b) both sides of the dielectric substrate ($\varepsilon' = 3.84$, $\tan\delta_\varepsilon = 0.018$, thickness 0.25 mm). Geometrical parameters: strip width 0.25 mm, gap width 0.5 mm, outer SRR height 3 mm, lattice constant 5 mm. EC-SRR rings spacing 0.5 mm.

(a) E_v, H_w, k_u : electric and magnetic excitation.
This configuration is characterized by the asymmetry of the EC-SRR with respect to the electric field direction, indicating the presence of a magnetoelectric coupling. The currents circulating in the rings are excited by the external magnetic field H_w or electric field E_v closing the gaps of the rings.

(b) E_u, H_w, k_v : magnetic excitation.
There is a symmetry of the structure regarding direction u and consequently lack of magnetoelectric coupling in the structure. The magnetic response of the particle is excited solely by the magnetic field H_w.

(c) E_v, H_u, k_w : electric excitation.
EC-SRR is asymmetric regarding direction v that indicates existence of cross-coupling effects. This case is called electric excitation, due to the coupling of the electric field from the incoming wave to the resonance of the currents circulating in the rings.

(d) E_u, H_v, k_w : no excitation.
This orientation is characterized by the symmetry of the resonant element regarding direction u and consequently no magnetoelectric effects are expected in the structure. The EC-SRR is not excited, as the magnetic field H_v is parallel to the plane of the rings (w), and electric field E_u does not close the gaps of the rings.

This theoretical analysis shows, that depending on the orientation of the EC-SRR regarding external EM fields, the structure can exhibit either a bianisotropic or non-bianisotropic behavior. On the other hand, the inherent symmetry of the BC-SRR geometry provides a lack of magnetoelectric couplings in any 2D configuration [13].

Bianisotropy can be also examined experimentally, e.g. from the transmission measurement of a square waveguide loaded by a SRR sample (this method is particularly useful for the analysis of bi-isotropic structures). The input port of a square waveguide is fed with the TE_{10} mode, whereas the TE_{01} mode of orthogonal polarization is measured at the output port. The resulting non-zero cross-polarization transmission coefficient indicates that the

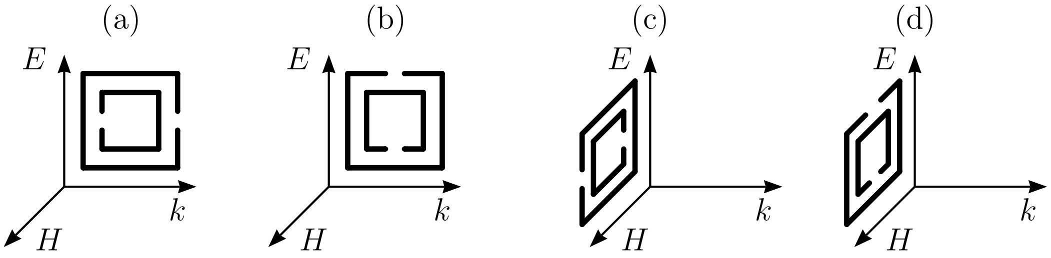

Figure 3.2: Four orientations of the EC-SRR with relation to the field polarization and propagation direction.

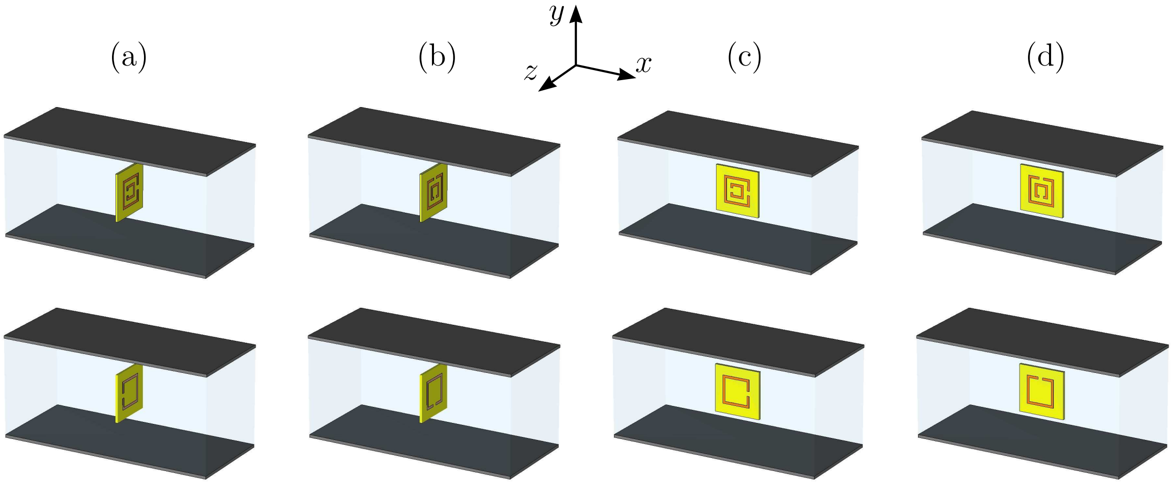

Figure 3.3: Different orientations (a)-(d) of the EC-SRR (top) and BC-SRR (bottom) inside a parallel plate waveguide for magnetic (H_x) or electric (E_y) excitation of particle resonances. Waveguide dimensions: plates separation (y) 1 cm, width (x) 2.28 cm, length (z) 1 cm.

incident electric field can excite not only a parallel electric dipole but also a parallel magnetic dipole (equivalently, an incident magnetic field can excite both magnetic and electric dipoles parallel to the exciting field) [152]. A similar experiment can be performed in a free-space set-up, by measurement of a microwave beam transmitted through the MTM slab. For the examination of cross-polarization, two orthogonally oriented waveguide horn antennas connected to a network analyzer are typically used [154].

The experiments conducted on MTM loaded waveguides allow one to identify the response type (electric/magnetic) of the metamaterial under test [155]. To identify the type of the SRR resonance, the structure is excited either by the electric or magnetic field, for different orientations of the particle inside a rectangular or a parallel plate waveguide (Fig. 3.3). For configuration based on a parallel plate waveguide, TEM mode with H_x and E_y field components is used. Thus, in orientations (a) and (b) the SRR is excited by both electric (E_y) and magnetic (H_x) fields, whereas in positions (c) and (d), since there is no magnetic flux perpendicular to the particle, the SRR is excited solely by the electric field (E_y).

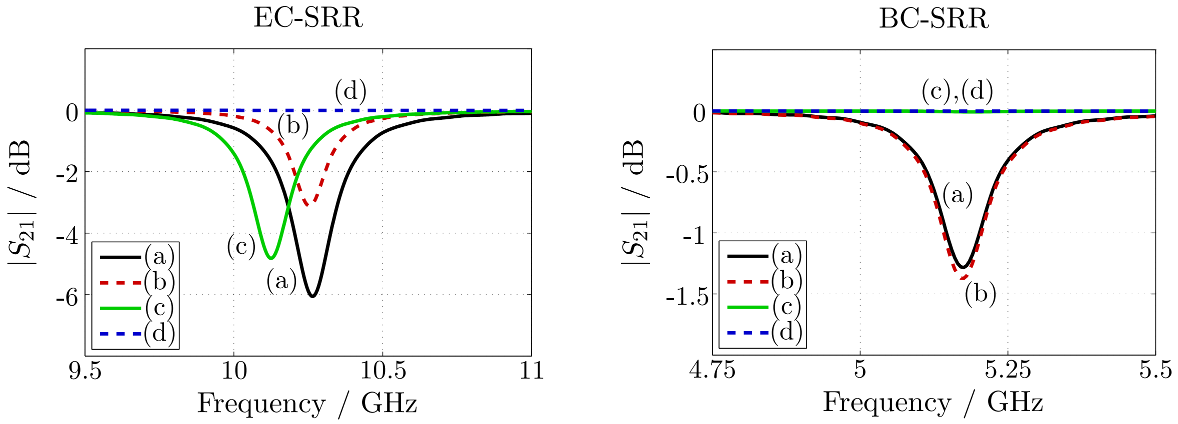

Figure 3.4: Transmission characteristics for different orientations of EC-SRR and BC-SRR in a parallel plate waveguide shown in Fig. 3.3. The cutoff frequency of the first higher order mode (TE_1/TM_1) for the unloaded parallel plate waveguide is equal to 30 GHz.

The simulated transmission coefficients for different configurations of the SRR loading the waveguide are shown in Fig. 3.4, at frequencies near the resonance of the SRR and for propagation assumed in the z direction. The physical dimensions of the parallel plate structure are equivalent to those of the standard X-band (WR-90) rectangular waveguide, whereas PEC/PMC are used as boundary conditions in y/x directions. It can be observed, that the BC-SRR is excited in positions (a) and (b), whereas it is not excited in orientations (c) and (d). Moreover, the transmission characteristics for the cases (a) and (b) are virtually the same, which means that the electric field component E_v (Fig. 3.1b) does not excite the structure. Therefore, it can be concluded, that the BC-SRR resonance is of magnetic type, i.e. it is excited only when the particle is placed in a homogeneous (at the particle scale) magnetic field (B_w). The behavior of the EC-SRR is more complicated than that of the BC-SRR. From the results corresponding to orientation (d) it can be concluded that EC-SRR does not respond to the electric field components polarized along the continuous branches of the rings (E_u). The main particle excitation (the strongest dip in the transmission characteristic) occurs at orientation (a), where both electric (E_v) and magnetic (B_w) field components are present. Weaker responses occur for orientation (b) and (c) corresponding to separate magnetic (B_w) or electric (E_v) field excitations, respectively[1]. These results point out, that the resonance of an EC-SRR is generally of magnetoelectric character and that the cross-coupling effects can be eliminated by a proper geometrical orientation of the rings. Moreover, the results obtained from numerical experiments with MTM loaded waveguides support the conclusions resulting from the theoretical analysis of MTM unit-cell symmetries. Both approaches are valuable tools that can be used for the identification of bianisotropic effects in MTM structures.

---

[1] In the analysed example, the electric resonance (c) is stronger than the magnetic one (b). This is not always the case and depends on the geometry and shape of the EC-SRR. Most often, the magnetic response of EC-SRRs is significantly stronger than the electric one (see e.g. [155]). The particular geometries and dimensions of SRRs analysed in this work are related to those used in the negative refraction experiment published by Shelby *et al.* [14].

3.2 Effective Medium Approach

The goal of assigning electromagnetic parameters to a composite or a mixture of two or more component materials has long been the aim of traditional analytic homogenization theories. All known analytical methods, however, are valid under certain limitations and for particular geometries or classes of structures. Analytical homogenization techniques are unreliable or not applicable for metamaterials comprising resonant elements and characterized by a non-negligible lattice constant. As an alternative for such composites, a numerical approach is feasible in which the local electromagnetic fields of a structure are calculated by solution of Maxwell's equations. This section presents an overview of the most popular schemes used for homogenization of MTM structures. The homogenization methods presented in this work are limited to non-bianisotropic structures.

3.2.1 Retrieval from Scattering Parameters

The most popular approach for the extraction of metamaterial constitutive parameters is retrieval from transmission and reflection characteristics - the method commonly used in laboratories as an experimental way to find effective parameters of a material sample under test (Appendix B) [156]. The scattering parameters are calculated or measured for a finite thickness of a MTM (usually one unit cell) and related to analytical formulas for reflection and transmission of a homogeneous slab with the same thickness a [104, 157, 158]:

$$S_{11} = \frac{(1-T^2)R}{1-R^2T^2}, \qquad S_{21} = \frac{(1-R^2)T}{1-R^2T^2}, \tag{3.1}$$

where R is the reflection coefficient of a wave incident on the interface between a MTM and free space, whereas T is the transmission through the MTM slab:

$$R = \frac{Z-Z_0}{Z+Z_0}, \qquad T = e^{-jk_0na}, \tag{3.2}$$

and Z_0, k_0 are wave impedance and wavenumber in free space, respectively. The normalized wave impedance $z = Z/Z_0$ and refractive index n of the homogeneous slab can be expressed in terms of scattering parameters as:

$$z = \pm\sqrt{\frac{(1+S_{11})^2 - S_{21}^2}{(1-S_{11})^2 - S_{21}^2}}, \tag{3.3}$$

$$n = -\frac{1}{k_0 a}\Big(\big(\Im(\ln T) + 2m\pi\big) - j\Re(\ln T)\Big), \tag{3.4}$$

where $m \in \mathbb{Z}$ is related to the branch index of n' (principal value for $m = 0$) and the transmission term in function of scattering parameters:

$$T = \frac{1 - S_{11}^2 + S_{21}^2}{2\,S_{21}} \pm j\sqrt{1 - \left(\frac{1 - S_{11}^2 + S_{21}^2}{2\,S_{21}}\right)^2}. \tag{3.5}$$

Since the material under consideration is a passive medium, the signs in (3.3) and (3.5) are determined by the requirements:

$$\Re(z) \geq 0, \qquad n'' \geq 0. \tag{3.6}$$

The relative electric permittivity and magnetic permeability characterizing the effective properties of the medium and equivalent to the obtained refractive index n and normalized impedance z are directly calculated as:

$$\varepsilon_{\text{eff}} = \frac{n}{z}, \qquad \mu_{\text{eff}} = nz. \tag{3.7}$$

The retrieval from scattering parameters is a straightforward method that most often allows the characterization of a MTM with sufficient accuracy. However, this procedure in its basic form delivers a variety of artefacts in the retrieved parameters, related to the inherent inhomogeneity of a MTM unit cell. The effective medium picture is often spoiled by significant anomalies, e.g. resonance-antiresonance coupling, truncated resonances of the refractive index, or discrepancy between n and z about the positions of the resonances [11]. These artefacts in the retrieved material parameters are particularly severe for structures that make use of resonant elements, as large fluctuations occuring in n and z result in the wavelength inside the MTM shortened to the order of the unit-cell dimension. Moreover, the retrieval process fails in some cases, e.g. when reflection or transmission coefficients are very small in magnitude [159]. Although some improvements based on the determination of effective boundaries, forced continuity of the dispersive effective refractive index, and the elimination of the measurement/simulation noise influence on effective impedance have been proposed [158], the retrieval method still delivers unsatisfactory results [160].

An example can be seen in the retrieved ε'' and μ'' parameters, which typically differ in sign for a unit cell that has an electric or a magnetic resonance. Fig. 3.6 presents effective material parameters retrieved from scattering matrix obtained from simulation of a circular BC-SRR structure (Fig. 3.5a). The structure is excited by the fundamental mode of a waveguide port located at the $\pm z$ limits of the mesh volume (TEM wave with E_y and H_x components) propagating in the $-z$ direction. PMC applied at the faces along the axis of the rings ($\pm x$ limits) and PEC used at the $\pm y$ faces of the volume act equivalently to periodic boundary conditions in transversal directions having the added benefit that the proper polarization of the solution is selected. The BC-SRR is known to be a SNG structure responding solely to the magnetic field (see Sec. 3.1), but the extracted effective permittivity indicates the presence of the electric response near the SRR resonance. The antiresonant form of ε' and the negative values of ε'' in the SNG frequency range are numerical artefacts typical for the $\boldsymbol{S}$-retrieval method.

The same artefacts occur in the extracted parameters for DNG structures built as combinations of SRRs and wires (structure shown in Fig. 3.5c, excitation with electric field E_y parallel to the strip and magnetic field H_x in the axis of the ring). Also in this case, the extracted ε_{eff} indicates an additional, non-physical response near the SRR resonance frequency (Fig. 3.7).

On the other hand, in Fig. 3.8 the effective parameters retrieved for a unit cell of a wire lattice are shown, for field E_y, H_x propagating in the direction $-z$. The EM response of a periodic array of parallel wires for electric field polarized parallel to the wires is non-resonant and similar to that of a low density plasma, with the plasma frequency in the GHz range (see Sec. 1.3). In this case, the retrieval method delivers physical values of effective parameters.

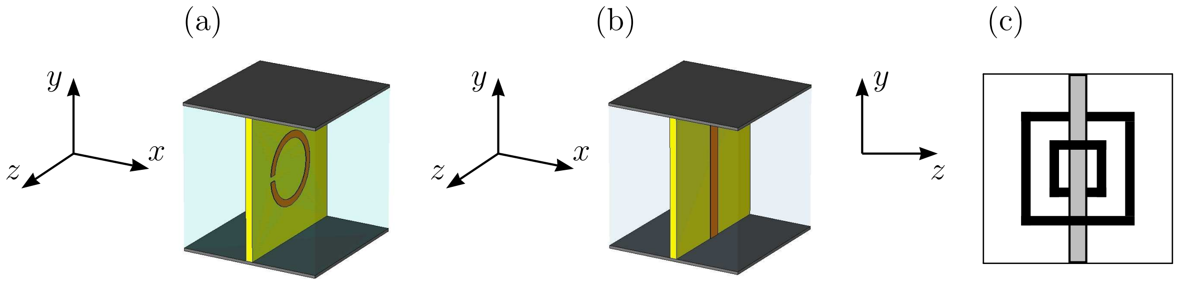

Figure 3.5: (a) Circular BC-SRR (lattice constant 10 mm; substrate: thickness 0.49 mm, $\varepsilon' = 2.43$; SRR: gap 0.4 mm, outer SRR radius 2.6 mm, strip width 0.5 mm). (b) Wire unit cell (lattice constant 5 mm; substrate: thickness 0.25 mm, $\varepsilon' = 3.84$, $\tan\delta_\varepsilon = 0.018$; strip width 0.5 mm). (c) SRR/wire (SRR at the front side, wire at the back side of the substrate). Substrate and wire width as in example (b), outer SRR length 3 mm, inner SRR length 1.5 mm, ring spacing 0.5 mm, SRR conductor width 0.25 mm. All strips and rings are modeled as copper.

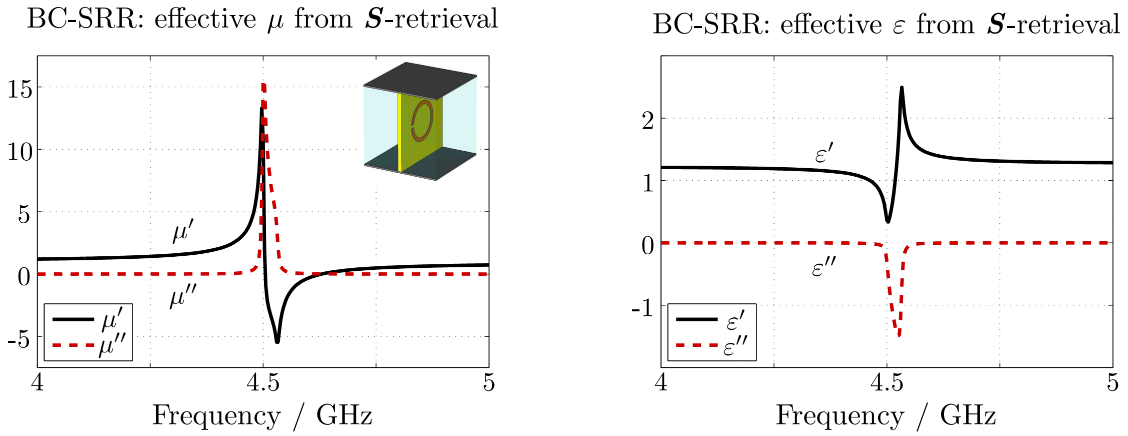

Figure 3.6: $\boldsymbol{S}$-retrieved effective parameters for a BC-SRR with circular rings (resonant structure, Fig. 3.5a). The extracted electric permittivity shows non-physical behavior in the SNG range.

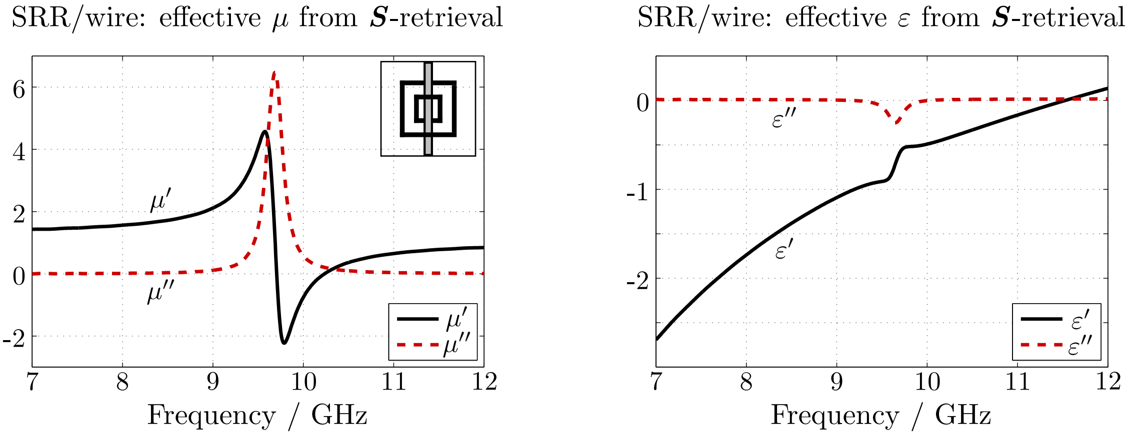

Figure 3.7: $\boldsymbol{S}$-retrieved effective parameters for the SRR/wire combination from Fig. 3.5c. The extracted electric permittivity shows non-physical behavior in the frequency range near the ring resonance.

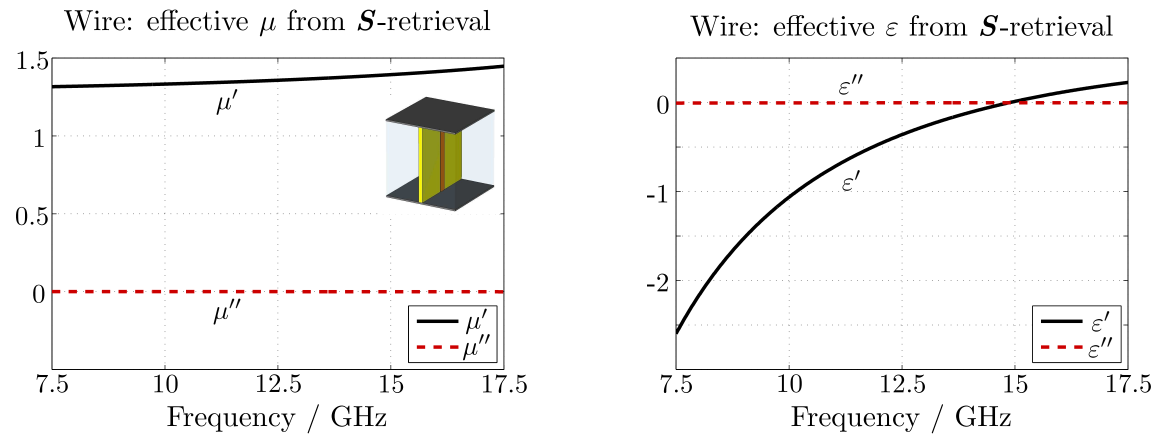

Figure 3.8: $\boldsymbol{S}$-retrieved effective parameters for a wire unit cell (Fig. 3.5b). Both extracted parameters show physical behavior.

The non-physical behavior of extracted effective permittivity or permeability obtained by $\boldsymbol{S}$-retrieval method was criticised in several papers, where it was pointed out that such parameters cannot form the effective description of a homogenized material [12, 161, 162].

3.2.2 Fields Averaging Method

Pendry's Fields Averaging Method

The application of Fields Averaging Method (FAM) to the description of metamaterial structures was first proposed by Pendry *et al.* [61]. The general idea relies on computation of the effective parameters from the electric and magnetic fields and fluxes averaged over certain spaces. A key question in this case is how to average the fields in order to obtain a reasonable representation of the MTM under test. For the structures made of thin wires or sheets of metal, if the averages of fields and fluxes were taken over the same regions of space, ε_{eff} and μ_{eff} would always be constants related to the permittivity and permeability of the host material. Pendry *et al.* presented a straightforward approach based on averaging of the local fields according to:

$$\langle E_u \rangle_L = \frac{1}{L_u} \int_{L_u} \vec{E}(\vec{r}) \cdot d\vec{s}, \qquad (3.8) \qquad \langle D_u \rangle_A = \frac{1}{A_u} \int_{A_u} \vec{D}(\vec{r}) \cdot d\vec{A}, \qquad (3.10)$$

$$\langle H_v \rangle_L = \frac{1}{L_v} \int_{L_v} \vec{H}(\vec{r}) \cdot d\vec{s}, \qquad (3.9) \qquad \langle B_v \rangle_A = \frac{1}{A_v} \int_{A_v} \vec{B}(\vec{r}) \cdot d\vec{A}, \qquad (3.11)$$

where $\langle E_u \rangle_L$ and $\langle H_v \rangle_L$ are obtained from line integrals over the local $\vec{E}$ and $\vec{H}$ fields, and $\langle D_u \rangle_A$ and $\langle B_v \rangle_A$ are obtained from integrals of the local $\vec{D}$ and $\vec{B}$ fluxes over the surfaces of the unit cell. The line integration paths L_u and L_v are located along the

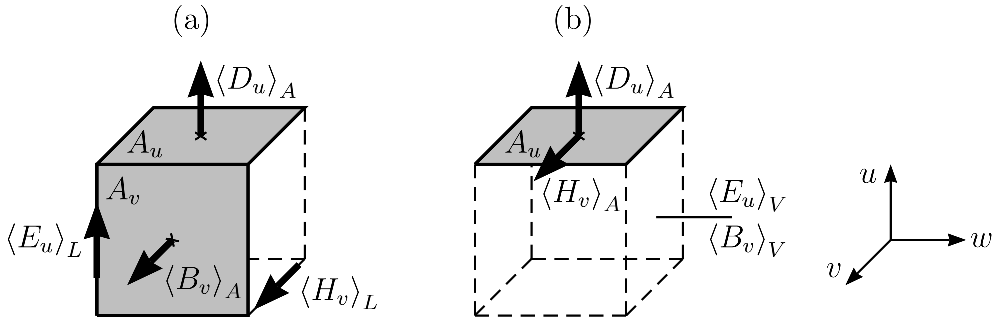

Figure 3.9: The allocation of integrated fields and fluxes in the Fields Averaging Method. (a) Pendry's surface/line based approach (3.8-3.13). (b) Acher's volume/surface based approach (3.18-3.23).

edges of the cubic unit cell and are not allowed to intersect with any of the metallic structures contained within the MTM cell (Fig. 3.9a). The flux integration areas A_u and A_v are equivalent to the faces of the MTM unit cell and perpendicular to the paths L_u and L_v, respectively. The integration surfaces, similar as the integration paths, cannot be crossed by any conducting element passing continuously from one unit cell to the next [163]. This is a serious disadvantage of the method, that limits its application to MTM lattices not including continuous wires. The ratios of the averaged quantities define the effective material parameters in the directions equivalent to the fields orientations:

$$\varepsilon_u = \frac{\langle D_u\rangle_A}{\langle E_u\rangle_L}, \qquad (3.12) \qquad\qquad \mu_v = \frac{\langle B_v\rangle_A}{\langle H_v\rangle_L}. \qquad (3.13)$$

From Fig. 3.9a it can be noticed, that Pendry's formulation of FAM is closely related to the discrete form of Maxwell curl equations used in FIT and FDTD (a MTM unit cell is equivalent to a single cell of the numerical grid - cf. Fig. 2.1; for more details see e.g. [163]).

Smith's Fields Averaging Method

In many MTM geometries, such as a SNG medium of continuous wires or a DNG combination of SRR/wires, a conducting element passes continuously from one unit cell to the next. For the flux averages to be correct in this case, the formulation of the effective medium parameters should be modified in order to include the contribution of the current flowing between the cells. Typically, as a more useful alternative, a gap is introduced in the wire near the integration surface so that the current is no longer continuous. If the gap is very small, the EM properties of the simulated structure may not be significantly affected and the fields within the gap and in the integration plane effectively account for the contribution of the current in the conductor [163]. However, in some cases the introduction of the discontinuity in the wire lattice may shift the resonance frequency, change the character of the resonance, or even entirely spoil the requested behavior of the MTM structure [164, 165]. Moreover, the additional element in the MTM geometry can significantly increase the numerical costs, as the small gap has to be discretized with additional mesh lines of the computational grid.

To avoid this inconvenient approach, the original fields averaging method proposed by

Pendry and based on surface/line averages was modified by D. Smith, who eliminated the requirement for the flux averages [163]. Smith's approach is solely based on line averages of the field quantities (the integration paths L_u, L_v are the same as in Pendry's method), from which the wave impedance characterizing the medium is obtained (3.14).

$$Z = \frac{\langle E_u \rangle_L}{\langle H_v \rangle_L}, \qquad (3.14) \qquad\qquad n = \frac{kc_0}{\omega}. \qquad (3.15)$$

The effective material parameters are computed, as in the $\boldsymbol{S}$-retrieval method, from Z and n values (3.7), where n is the effective refractive index calculated from the results of eigenmode solver simulations of the MTM unit cell. In (3.15), ω represents radial eigenfrequencies of the computed modes, whereas k is the wavenumber ($k = \varphi/a$) obtained from the phase advance φ of the periodic boundary condition and the length of the unit cell a, both in the assumed direction of propagation (cf. Sec. 4.2).

Knowledge of the effective refractive index n (or, equivalently, the propagation constant in the medium k) allows one to introduce a correction factor to Pendry's formulas for effective parameters, accounting for the spatial dispersion effects related to the finite length of the unit cell in the direction of propagation. Corrected ratios of the averaged quantities (3.12-3.13) take the form:

$$\varepsilon_u = \frac{\langle D_u \rangle_A}{\langle E_u \rangle_L} \frac{ka}{\sin(ka)}, \qquad (3.16) \qquad\qquad \mu_v = \frac{\langle B_v \rangle_A}{\langle H_v \rangle_L} \frac{ka}{\sin(ka)}. \qquad (3.17)$$

Application of the eigenmode solver simulations in Smith's FAM approach makes it possible to avoid structure modifications that may be required when using Pendry's FAM approach. Therefore, Smith's method may by applied to a larger class of MTM structures. There are, however, two important consequences of using the eigenmode solver in FAM. Firstly, the losses are neglected (as the lossless solver is commonly used) and consequently the extracted ε_{eff} and μ_{eff} parameters are real. Secondly, the computed eigenfrequencies characterize the MTMs under test only in the passbands of the particular modes. Therefore, the effective constitutive parameters can be extracted only in the frequency bands corresponding to double negative or double positive ε_{eff} and μ_{eff} values (cf. Fig. 1.6). For single negative materials no information can be provided regarding the negative values of permittivity or permeability - that is significant limitation of this method.

Acher's Fields Averaging Method

Another approach to MTM homogenization based on field averaging and related to Pendry's method was proposed by O. Acher *et al.* [166,167]. Being similar to Pendry's method, the fields averaging is based on the Maxwell's curl equations. The impedance and refractive index characterizing the material are expressed in function of EM fields inside the composite, sufficiently far from the interface so that they correspond to a single propagating mode. It is pointed out, that at the vicinity of the interface between the composite and surrounding medium many higher order modes may be present and therefore the line averaging near the interfaces (as in Pendry's approach) should be avoided. The effective constitutive parameters are expressed in terms of the averaged fields and fluxes as [166]:

$$\varepsilon_u = \frac{\langle D_u \rangle_A}{\langle E_u \rangle_V}, \qquad (3.18) \qquad\qquad \mu_v = \frac{\langle B_v \rangle_V}{\langle H_v \rangle_A}, \qquad (3.19)$$

where the averaged quantities are computed according to:

$$\langle E_u \rangle_V = \frac{1}{V} \int_V E_u(\vec{r})\, dV, \quad (3.20) \qquad \langle D_u \rangle_A = \frac{1}{A_u} \int_{A_u} D_u(\vec{r})\, dA, \quad (3.22)$$

$$\langle H_v \rangle_A = \frac{1}{A_u} \int_{A_u} H_v(\vec{r})\, dA, \quad (3.21) \qquad \langle B_v \rangle_V = \frac{1}{V} \int_V B_v(\vec{r})\, dV. \quad (3.23)$$

When examining (3.20)-(3.23) important differences can be noticed when compared to Pendry's formulas (3.8)-(3.11). The electric field and magnetic flux are averaged over the volume of the unit cell, whereas the averages of magnetic field and electric flux components are taken over the same surface A_u, depicted in Fig. 3.9b. As the field quantities are averaged over volume and surfaces instead of surfaces and lines, Acher's FAM is sometimes referred to as volume/surface approach (whereas Pendry's method is called surface/line averaging) [168].

Due to the application of the surface averages in the plane perpendicular to the direction of the electric field, Acher's method is characterized by the same disadvantage as Pendry's approach[2]: it cannot be directly applied to MTMs including continuous wires that would intersect the integration plane. For SRR/wire combinations the MTM geometry has to be modified and the continuous wires replaced by finite pieces separated by planar capacitive elements parallel to the integration surface - with the same consequences that were already mentioned when discussing Pendry's approach.

The authors (Acher *et al.*) claim that their method is restricted to the cases when one single mode propagates in the composite, as is required by the homogenization approach. On the other hand, they present negative magnetic permeability extracted for SRR based structures [167–169]. This is a kind of contradiction, as the SNG frequency range represents a stopband where no single mode can propagate in the periodic lattice. Care is required by the formulation of requirements for MTM homogenization. In fact, the extracted effective parameters for split ring resonators represent the behavior of the structure in the stopband, as well as in (part of) the passbands located above and below the SRR resonant frequency (the passbands are characterized by $\mu' > 0$, see Sec. 4.2).

Fields Averaging Method: applications

The three versions of the fields averaging method, referred to as: (i) Pendry's FAM, (ii) Smith's FAM, (iii) Acher's FAM, are applied to several metamaterial structures, i.e.:

- continuous wire (Fig. 3.5b),
- non-continuous wire (Fig. 3.10a),
- BC-SRR (Fig. 3.5a),
- SRR and continuous wire (Fig. 3.5c),
- SRR and non-continuous wire (Fig. 3.10b).

For the MTMs under test based on non-continuous wires, the substrate is removed and a gap with additional capacitive loading is introduced between the wire and the top PEC

---

[2] The integration surface A_u is in fact the same in both methods.

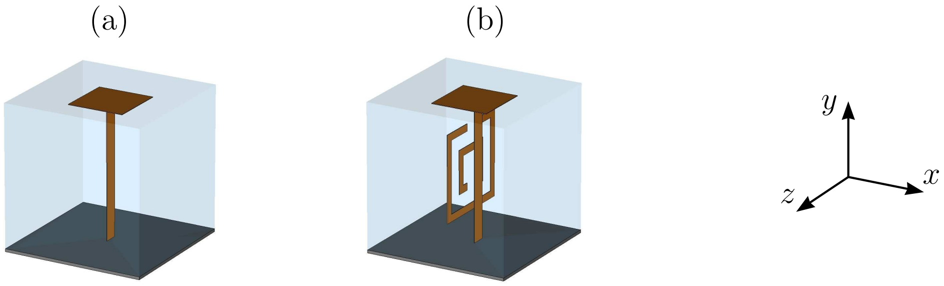

Figure 3.10: Modified MTM unit cells based on non-continuous wires. The geometries are equivalent to those shown in Figs. 3.5b,c. The wire strip is shortened to 4.75 mm (0.25 mm gap between the wire and the top face of the unit cell), the substrate removed (free-space host). The area of the additional metal plate 2 mm × 2 mm. For better visualization the top PEC plate is not shown. (a) Non-continuous wire. (b) SRR and non-continuous wire.

face of the unit cell (the integration plane is located within the gap). Thus, the metallic elements are embedded in free space, whereas the geometric parameters of the additional elements are arbitrarily chosen as 0.05 of the unit cell height for the gap height and 0.16 of the unit cell cross-section for the capacitor plate area.

The EM field distributions used for the determination of effective material parameters in Pendry's and Acher's FAM are obtained by simulations of MTM unit cells with time-domain solver, similar to the $\boldsymbol{S}$-retrieval method (the field distributions are recorded as monitors at particular frequencies in the frequency band of interest). The unit cell is excited by the fundamental mode of the waveguide ports, whereas PEC and PMC boundary conditions limit the structure in the transversal dimensions and guarantee the selection of the proper field polarization (E_y, H_x). For Smith's version of FAM, the unit cell is simulated with the eigenmode solver, assuming PBC (and swept phase shift) in the direction of propagation (z). In the transversal directions, either the combination of electric/magnetic or periodic (with 0 deg relative phase shift) boundary conditions can be used, with no significant difference in the results[3].

The integration surfaces depicted schematically in Fig. 3.9 can be situated anywhere between the face of the unit cell and the metallic scatterer of the MTM. However, as the EM fields have more abrupt variations close to the scatterer, to minimize discretization errors the integration planes are typically located at a distance of $1-2$ mesh nodes from the cell boundary (the same is valid for the integration paths).

Single Negative Metamaterials. The effective parameters obtained by fields averaging method for single negative metamaterials, i.e. continuous wire, non-continuous wire and BC-SRR, are presented in Figs. 3.11-3.15. For comparison, $\boldsymbol{S}$-retrieved results are also shown. In the case of the wires, the frequency dependence of the effective electric permittivity is expected to follow Drude behavior, whereas effective magnetic permeability μ' should be constant and close to unity (non-magnetic host). In the case of the broadside-coupled split ring resonator, effective magnetic permeability is expected to follow Lorentz characteristic, whereas the real part of the effective electric permittivity should have a

---

[3] This supports also the salient assumption, that a unit cell simulated with the time-domain solver and PEC/PMC transversal boundary conditions represents a single layer of (transversally infinite) periodic lattice.

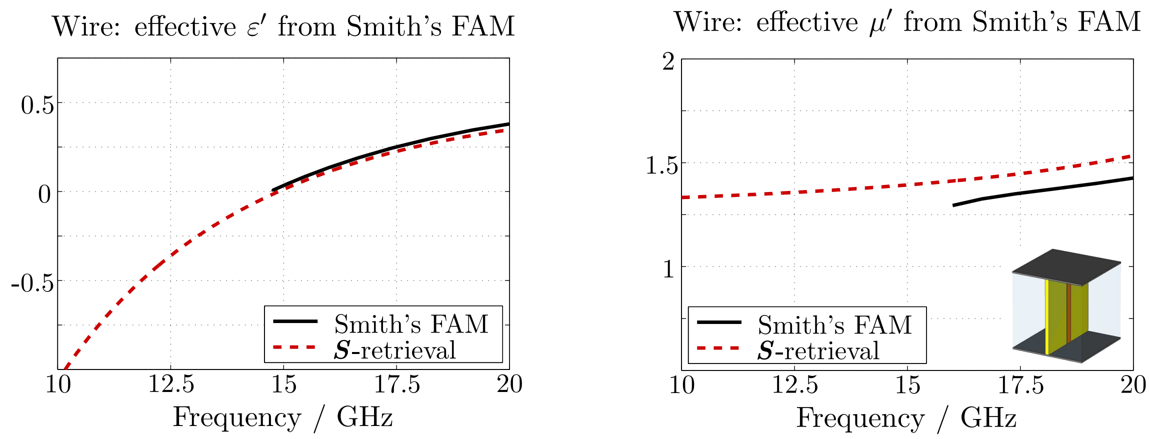

Figure 3.11: Real part of effective electric permittivity and magnetic permeability for a wire unit cell (Fig. 3.5b) extracted with Smith's FAM (solid line). For comparison, $\boldsymbol{S}$-retrieved parameters from Fig. 3.8 are shown (dashed line).

constant value between unity and ε' of the substrate (electric field is distributed partly in the dielectric substrate and partly in the free-space host).

Pendry's FAM provides single negative parameters that are an approximation of the values extracted by other methods under test. The real parts for constitutive parameters of interest (i.e. ε for non-continuous wires and μ for BC-SRRs) are similar to the theoretical Drude and Lorentz curves; the extracted imaginary parts, however, reveal non-physical, negative values of ε'' and μ'' in the observed frequency range (Figs. 3.12-3.13).

For all SNG examples, Smith's FAM delivers parameters that agree with effective permittivity and permeability obtained by $\boldsymbol{S}$-retrieval method. This also refers to the anti-resonant frequency dependence of the effective ε' in the case of the BC-SRR unit cell (Fig. 3.15). The imaginary parts of the constitutive parameters are assumed to be zero. It should be noted, that only positive values of ε' and μ' are extracted with the Smith's FAM.

Acher's formulation of FAM for SNG cells delivers results that closely match the expected frequency behavior of wires (Drude dependence) and BC-SRRs (Lorentz dependence). Concerning SNG parameters of interest, the results are in agreement with the effective description obtained by Smith's FAM and $\boldsymbol{S}$-retrieval method. The advantage of the Acher's method is that it delivers expected, constant values of ε' for the negative magnetic permeability structure (BC-SRR) and constant values of μ' for the negative electric permittivity structure (non-continuous wire), avoiding non-physical antiresonant behavior observed e.g. for Smith's FAM and $\boldsymbol{S}$-retrieved results in case of a BC-SRR (Fig. 3.15).

Double Negative Metamaterials. The constitutive parameters extracted with the fields averaging method for double negative metamaterials (SRR/continuous wire and SRR/non-continuous wire) are compared with $\boldsymbol{S}$-retrieved results in Figs. 3.16-3.18.

The effective magnetic permeability extracted with Pendry's FAM closely matches the values obtained from Smith's FAM and $\boldsymbol{S}$-retrieval method (Fig. 3.17). On the other hand, although the qualitative behavior of the extracted ε' corresponds to the expected Drude characteristic, there are significant differences between the absolute values obtained from Pendry's FAM and from other methods under test (Fig. 3.18). Moreover, the imaginary

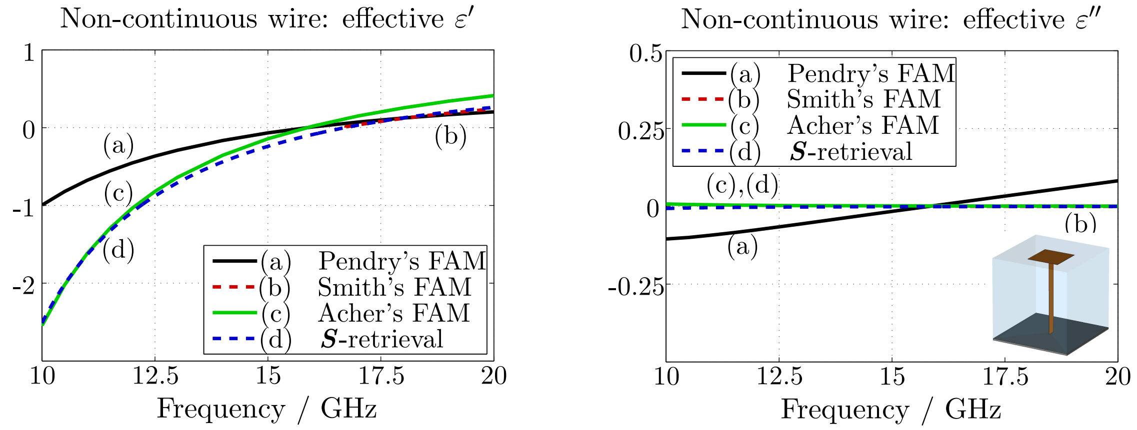

Figure 3.12: Effective electric permittivity for a non-continuous wire unit cell (Fig. 3.10a) extracted with FAM. For comparison, $\boldsymbol{S}$-retrieved parameters are shown.

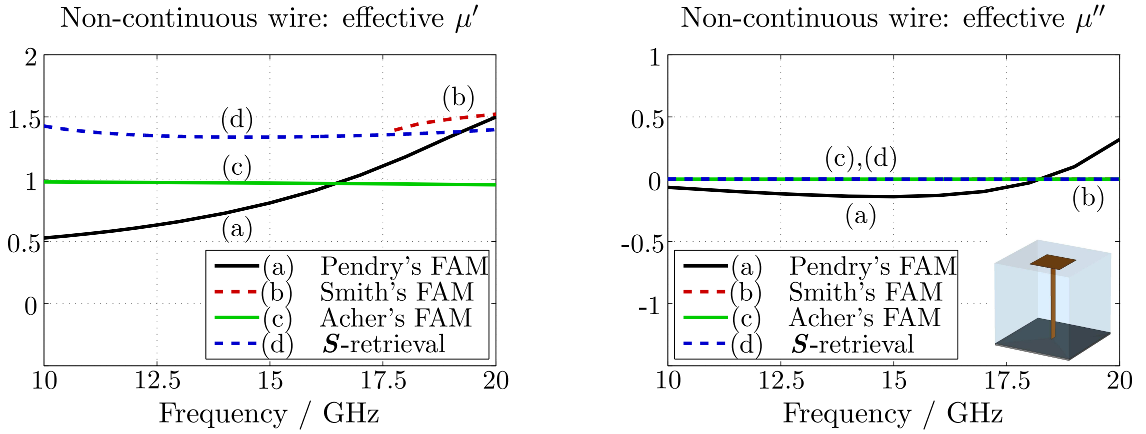

Figure 3.13: Effective magnetic permeability for a non-continuous wire unit cell (Fig. 3.10a) extracted with FAM. For comparison, $\boldsymbol{S}$-retrieved parameters are shown.

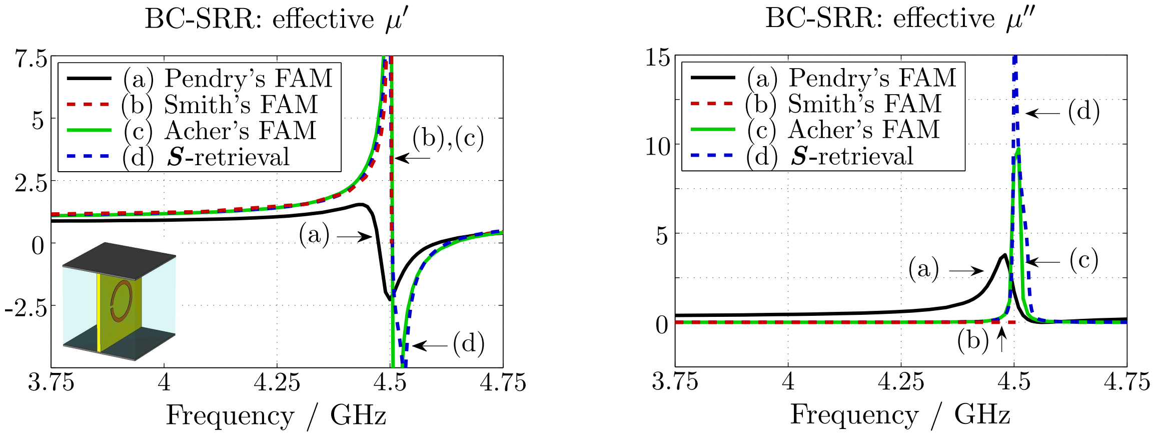

Figure 3.14: Effective magnetic permeability for a broadside-coupled split ring resonator (Fig. 3.5a) extracted with FAM. For comparison, $\boldsymbol{S}$-retrieved parameters from Fig. 3.6 are shown.

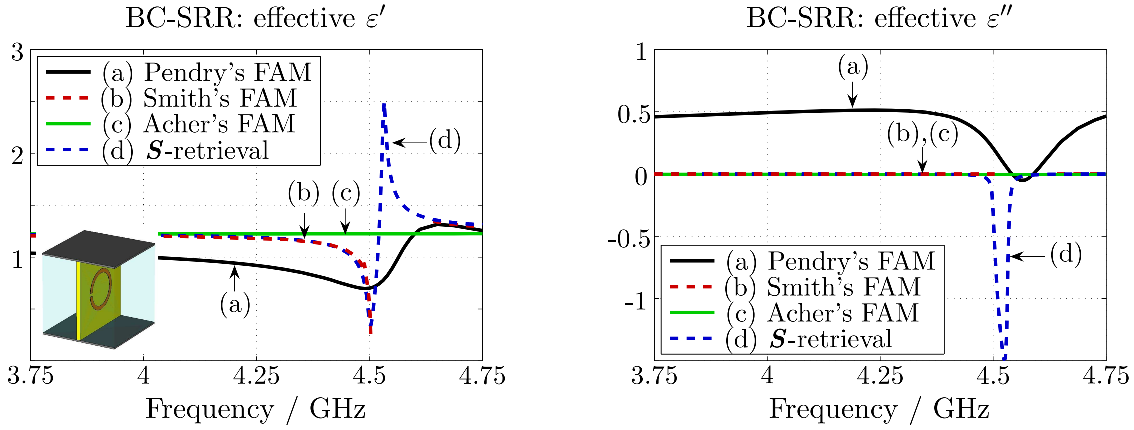

Figure 3.15: Effective electric permittivity for a broadside-coupled split ring resonator (Fig. 3.5a) extracted with FAM. For comparison, $\boldsymbol{S}$-retrieved parameters from Fig. 3.6 are shown.

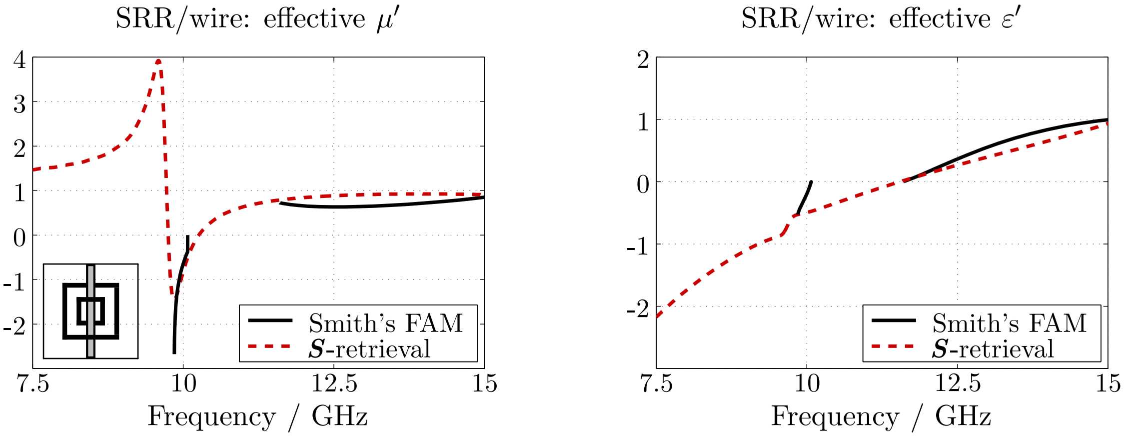

Figure 3.16: Effective magnetic permeability and electric permittivity for a SRR/wire unit cell (Fig. 3.5c) extracted with FAM. For comparison, $\boldsymbol{S}$-retrieved parameters from Fig. 3.7 are shown.

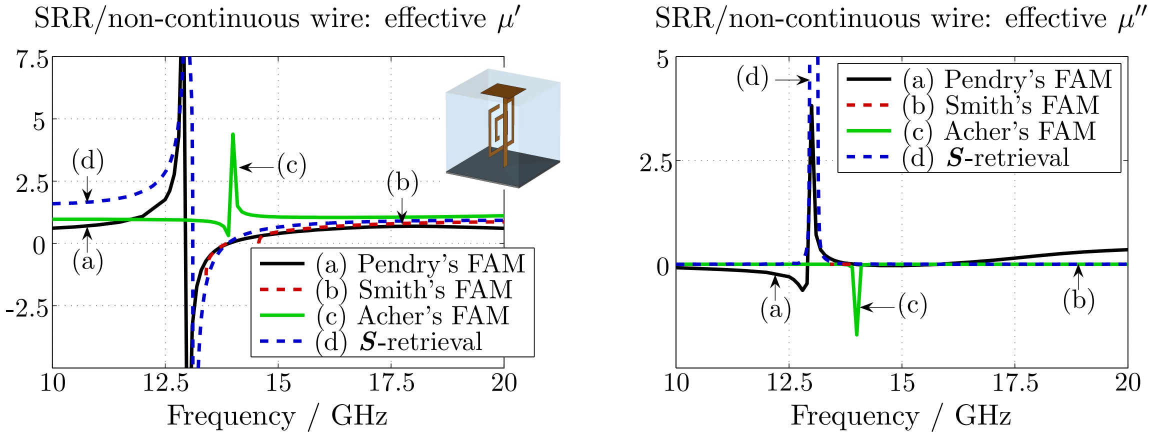

Figure 3.17: Effective magnetic permeability for a SRR/non-continuous wire unit cell (Fig. 3.10b) extracted with FAM. For comparison, $\boldsymbol{S}$-retrieved parameters are shown.

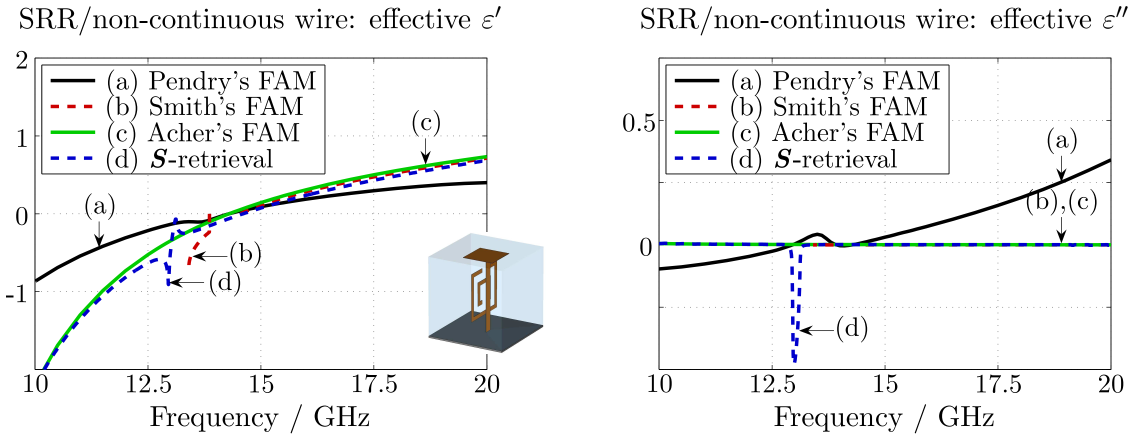

Figure 3.18: Effective electric permittivity for a SRR/non-continuous wire unit cell (Fig. 3.10b) extracted with FAM. For comparison, $\boldsymbol{S}$-retrieved parameters are shown.

parts of both extracted parameters, μ'' and ε'', acquire non-physical negative values in a part of the observed frequency range.

The real parts of constitutive parameters delivered by Smith's version of fields averaging method form an approximation of the results retrieved from the corresponding scattering matrix. There are some discrepancies in the effective permittivity values that can be noticed in the DNG frequency range, near the SRR resonance, for both versions of the MTM unit cell under test. The extracted constitutive parameters describe the metamaterial in DNG and DPS frequency ranges.

Acher's FAM fails for the tested DNG metamaterial structure based on the SRR and non-continuous wire. Although the extracted effective ε is equivalent to the Drude characteristic, μ' curve shows displaced antiresonant behavior, whereas μ'' is characterized by non-physical negative values (Fig. 3.17). Moreover, the extracted μ' is positive in the whole investigated frequency range, despite the fact that the structure is known to be DNG near the particle resonance.

Conclusions. Fields averaging method is suitable for the effective description of single negative metamaterials not including continuous wires. In such cases, the most reliable, physical results are obtained with Acher's version of FAM. For the unit cells based on continuous wires, applied geometry modifications result in the qualitative description of the "true MTM" behavior, as the structure characteristics are shifted in frequency due to additional capacitive elements. In the case of double negative metamaterials, FAM is prone to fail, delivering non-physical results in terms of negative ε'' or μ'' values. On the other hand, Smith's version of FAM can describe every metamaterial structure, but it neither provides effective parameters in important, single negative frequency bands, nor are the imaginary parts of the effective description obtained due to the neglection of losses. A potential advantage of FAM is that it can be used for the extraction of magnetoelectric parameters in bianisotropic media [154, 170].

3.2.3 Parameter Fitting of Dispersive Models

The methods commonly used for extraction of effective metamaterial parameters, i.e. retrieval from transmission and reflection coefficients and averaging of EM fields, often deliver results that violate physical laws. However, constitutive parameters that describe any physical material should satisfy the conditions of passivity and causality (cf. Sec. 2.1) [138].

From the observation of the frequency characteristics for MTM effective parameters, in most cases it can be noticed that extracted curves closely follow Drude or Lorentz behavior with additional artefacts occuring near the resonance frequency of the MTM. These non-physical artefacts can be prevented by applying predefined dispersive models representing the electric permittivity and magnetic permeability of the metamaterial.

The Lorentz model can be used for prediction of the frequency dependence for the magnetic permeability function of a MTM under test, according to[4]:

$$\mu_{\text{eff}}(\omega) = \mu_\infty + \frac{(\mu_s - \mu_\infty)\omega_0^2}{\omega_0^2 + j\omega\delta - \omega^2}, \tag{3.24}$$

where:

μ_s	magnetic permeability at the low-frequency limit of the model,
μ_∞	magnetic permeability at the high-frequency limit of the model,
ω_0	angular resonance frequency ($2\pi f_0$),
δ	damping frequency.

In metamaterials related research, the Drude characteristic is typically used as an analytical description of the electric properties for a lattice of continuous wires (cf. Sec. 1.3). The Drude model has the following form:

$$\varepsilon_{\text{eff}}(\omega) = \varepsilon_\infty - \frac{\omega_p^2}{\omega(\omega - j\nu_c)}, \tag{3.25}$$

where:

ε_∞	electric permittivity at the high-frequency limit of the model,
ω_p	angular plasma frequency ($2\pi f_p$),
ν_c	collision frequency.

A new approach to the homogenization of metamaterial structures, based on the predefined physical models, is proposed in the frame of this work: parameter fitting of dispersive models (PFDM) [171]. This method is related to the extraction from scattering matrix (Sec. 3.2.1). The main difference relies on the fact that the shape of the parameterized characteristics for effective permittivity and permeability is assumed a priori, whereas their parameters are optimized in order to obtain the best fitting to the reference responses.

Within the presented method, effective material description is found by fitting scattering parameters of the equivalent representation to the scattering parameters of the reference structure. The reference structure is a detailed metamaterial geometry simulated with the EM solver (Fig. 3.5), whereas the effective representation is a slab of an isotropic, homogeneous material described by the dispersive Drude or Lorentz model, according to

---

[4] The constitutive MTM parameters are extracted in a limited frequency range, in the vicinity of the first resonance frequency. Therefore, the first order dispersion model (3.24) is used here. In general, higher order terms describing higher order resonances can be used in the Lorentz model [1].

the type (single/double negative) of the homogenized MTM structure. The coefficients of the dispersive models (3.24)-(3.25) are the parameters in the optimization process (the details are given in Tab. 3.1). For single negative metamaterials, the positive constitutive parameter is assumed to be a real constant. Strictly speaking, it could be argued that a constant, real value of the constitutive parameter does not fulfill the physical requirements of the real part growing with frequency ($d\varepsilon'/d\omega > 0$, $d\mu'/d\omega > 0$) and non-zero imaginary part at $\omega \neq 0$ (cf. Sec. 2.1). However, as the single negative description is valid in the limited frequency range, the corresponding positive constitutive parameter is expected to be virtually constant in this range with a negligible imaginary part. Moreover, the analysed SNG metamaterials are assumed to be non-bianisotropic, i.e. there should be no resonant response to the electric field in the negative permeability material, or equivalently, no resonant response to the magnetic field in the negative permittivity material. A further consequence of extraction of effective material parameters in a limited frequency range is that the permittivity and permeability representing the low- or high-frequency limit of the model (μ_s, μ_∞, ε_∞) do not have to strictly satisfy the physical requirements at $\omega \to 0$ or $\omega \to \infty$.

The optimization goal of the PFDM method is to minimize the difference between the scattering parameters obtained for the reference structure and the homogeneous structure. The homogeneous cell should provide the same transmission/reflection coefficients as the SRR or wire based MTM unit cell.

Table 3.1: Parameter fitting of dispersive models: predefined constitutive description and model coefficients optimized for various types of MTM structures. All optimized coefficients are positive, real values.

Metamaterial type	μ model	ε model	Optimized coefficients
SNG: $\mu' < 0$, $\varepsilon' > 0$	Lorentz	Constant: ε_c	μ_s, μ_∞, ω_0, δ, ε_c
SNG: $\mu' > 0$, $\varepsilon' < 0$	Constant: μ_c	Drude	μ_c, ε_∞, ω_p, ν_c
DNG: $\mu' < 0$, $\varepsilon' < 0$	Lorentz	Drude	μ_s, μ_∞, ω_0, δ, ε_∞, ω_p, ν_c

The reference results are scattering parameters ($S_{11,\mathrm{ref}}$, $S_{21,\mathrm{ref}}$) computed for a detailed implementation of the MTM unit cell under test, as in the $\boldsymbol{S}$-retrieval method. On the other hand, the scattering parameters for the homogenized MTM cell are obtained analytically. Based on the assumed models for constitutive parameters, normalized effective impedance and refractive index of the homogenized model are computed according to:

$$z = \sqrt{\frac{\mu_{\mathrm{eff}}}{\varepsilon_{\mathrm{eff}}}}, \qquad n = \sqrt{\mu_{\mathrm{eff}}\,\varepsilon_{\mathrm{eff}}}. \tag{3.26}$$

As the predefined dispersive models fulfill the condition of causality and the MTM structure under test is a passive medium, the square root signs in (3.26) are determined by the requirements:

$$\Re(z) \geq 0, \qquad n'' \geq 0. \tag{3.27}$$

The reflection coefficient R at the boundary free space/MTM slab and the transmission coefficient T through the homogenized slab of effective impedance z, refractive index n, and thickness a (equal to the thickness of the detailed MTM unit cell) are given as:

$$R = \frac{z-1}{z+1}, \qquad T = \exp(-j\,\frac{\omega}{c_0}\,n\,a), \tag{3.28}$$

where ω is radial frequency and c_0 velocity of light in free space. The dependence between reflection/transmission and scattering parameters is given by [156]:

$$S_{11,\mathrm{eff}} = \frac{(1-T^2)R}{1-R^2T^2}, \qquad S_{21,\mathrm{eff}} = \frac{(1-R^2)T}{1-R^2T^2}. \tag{3.29}$$

The expressions (3.26)-(3.29) set the scattering parameters $S_{11,\mathrm{eff}}$, $S_{21,\mathrm{eff}}$ as functions of the effective material parameters μ_{eff}, $\varepsilon_{\mathrm{eff}}$ and form the basis for the PFDM approach. For the optimization of the parameters in the constitutive relations, the differential evolution algorithm is used, characterized by good convergence properties and straightforward choice of few control variables used to steer the optimization process [172,173]. The optimization procedure minimizes the goal function of the form:

$$G = \sum_i \left(\left|S_{11,\mathrm{eff}} - S_{11,\mathrm{ref}}\right|_{f_i} + \left|S_{21,\mathrm{eff}} - S_{21,\mathrm{ref}}\right|_{f_i} \right), \tag{3.30}$$

by fitting the scattering parameters at i frequencies f_i in the frequency range of interest.

Applications

The PFDM method is applied to three basic MTM structures, i.e. single negative circular BC-SRR, single negative wire and double negative SRR/wire combination. The reference scattering coefficients are obtained from simulations with the time-domain solver, as in the $\boldsymbol{S}$-retrieval method (Sec. 3.2.1). The optimized model coefficients are given in Tab. 3.2.

Table 3.2: Optimized coefficients values for the predefined effective description of MTM structures.

Model		Metamaterial		
type	parameter	BC-SRR	wire	SRR/wire
Constant	μ_c	–	1.39	–
	ε_c	1.10	–	–
Lorentz	μ_s	0.90	–	1.26
	μ_∞	0.85	–	1.12
	f_0 / GHz	4.52	–	9.67
	δ / MHz	89.2	–	1240
Drude	ε_∞	–	0.82	1.62
	f_p / GHz	–	13.57	14.63
	ν_c / MHz	–	77.3	30.7

The scattering parameters of the homogenized BC-SRR based metamaterial (structure shown in Fig. 3.5a), fitted to the reference results, are presented in Fig. 3.19, whereas the optimized constitutive parameters are given in Figs. 3.20-3.21. From the figures it can be noticed, that the predefined Lorentz characteristic of the effective magnetic permeability

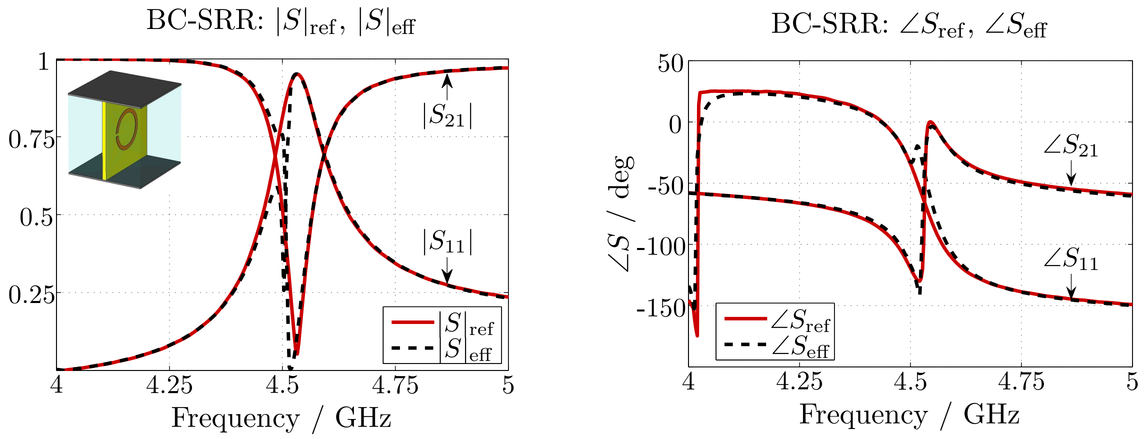

Figure 3.19: Scattering parameters of the homogenized single negative metamaterial (circular BC-SRR shown in Fig. 3.5a) fitted with PFDM (dashed line) to the reference results (solid line).

closely follows the curve extracted with the $\boldsymbol{S}$-retrieval method. On the other hand, the assumed constant value of the effective electric permittivity eliminates the antiresonant, non-physical behavior observed for the $\boldsymbol{S}$-retrieved characteristic. Constituting a negative magnetic permeability medium, the effective permittivity of the BC-SRR is expected to be a positive constant in the SNG frequency range with a negligible imaginary part. This assumption is confirmed by the resulting scattering parameters that are very well fitted to the reference results, apart from a slight mismatch between S_{eff} and S_{ref} close to the resonance frequency of the SRR. The reason for this discrepancy is the influence of higher order modes described in more detail in Chapter 5.

The effective electric permittivity of the BC-SRR equal to 1.1 indicates that the electric properties of the structure are similar to that of the free space, with a slight influence of the substrate. The effective magnetic permeability at the low- and high-frequency limit of the model (0.9 and 0.85, respectively) is close to unity, which is also the expected value, equivalent to free space (it should be noted, however, that higher order resonances can occur in the structure, e.g. at frequencies being a multiplicity of f_0 [155]). The optimized damping frequency (89.2 MHz) influences the width of the SNG band and the values of μ' and μ'' in this band (lower values of δ result in sharper resonances). BC-SRR is characterized by single negative parameters in the frequency range $4.51-4.65$ GHz, whereas double positive description is valid in $4-4.51$ GHz and $4.65-5$ GHz frequency bands (Tab. 3.3).

Table 3.3: BC-SRR: frequency bands of the effective description obtained with PFDM.

BC-SRR

Modeled frequency range	$4-5$	GHz
DPS: $\mu' > 0$, $\varepsilon' > 0$	$4-4.51$	GHz
SNG: $\mu' < 0$, $\varepsilon' > 0$	$4.51-4.65$	GHz
DPS: $\mu' > 0$, $\varepsilon' > 0$	$4.65-5$	GHz

In the case of the single negative wire metamaterial (Fig. 3.5b), there is virtually no difference between scattering parameters fitted with PFDM and the reference results obtained

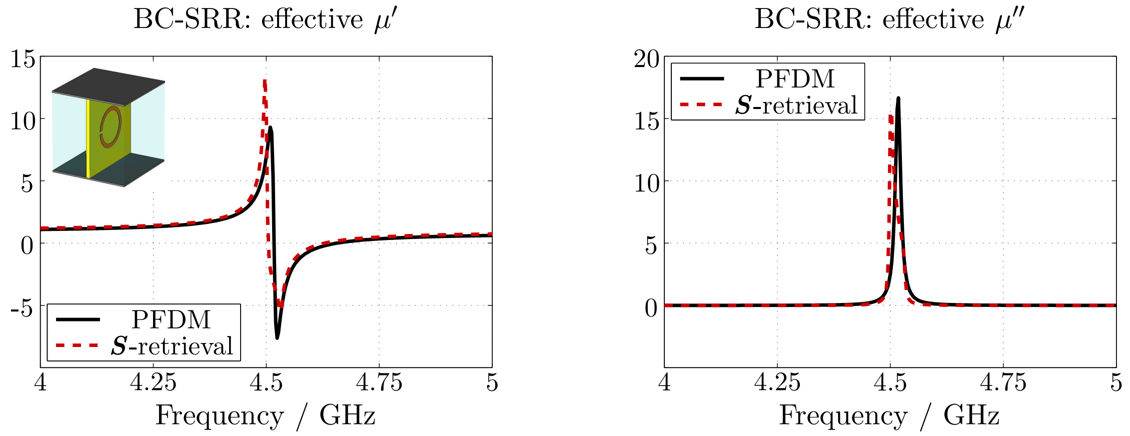

Figure 3.20: Effective magnetic permeability for a circular broadside-coupled split ring resonator (Fig. 3.5a) extracted with PFDM (solid line). For comparison, $\boldsymbol{S}$-retrieved results from Fig. 3.6 are shown (dashed line).

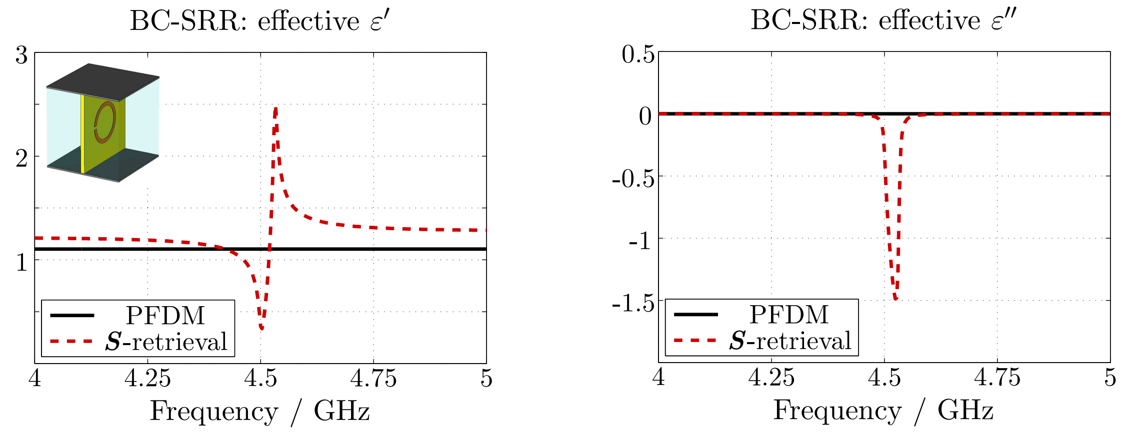

Figure 3.21: Effective electric permittivity for a circular broadside-coupled split ring resonator (Fig. 3.5a) extracted with PFDM (solid line). For comparison, non-physical results obtained by the $\boldsymbol{S}$-retrieval method (Fig. 3.6) are shown (dashed line).

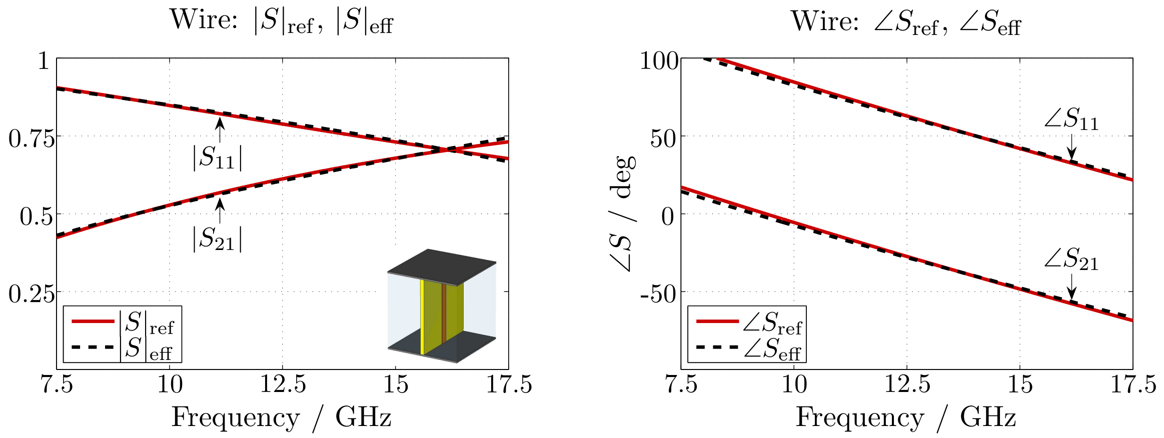

Figure 3.22: Scattering parameters of the homogenized single negative metamaterial (wire shown in Fig. 3.5b) fitted with PFDM (dashed line) to the reference results (solid line).

by simulations of the detailed structure (Fig. 3.22). There is also a very good agreement between the effective ε and μ retrieved from scattering parameters and obtained by PFDM (Fig. 3.23). As mentioned in Sec. 3.2.1, the $\boldsymbol{S}$-retrieval method works quite well for the case of weakly and non-resonant structures. The metamaterial based on a lattice of wires forms an example of such a structure and its effective permittivity is described by the dispersive Drude model. From the frequency characteristic of magnetic permeability it can be noticed that μ' is very well approximated by a constant value assumed in PFDM method and equal to 1.39. The accuracy of this approximation depends on the width of the frequency range in which the effective description is valid (the narrower the frequency band, the better the approximation). For the wire metamaterial under consideration, the constitutive parameters obtained with PFDM are valid in the relatively broad frequency range 7.5 – 17.5 GHz covering single negative ($\varepsilon' < 0$, $\mu' > 0$) and double positive bands ($\varepsilon' > 0$, $\mu' > 0$). The imaginary parts of permittivity and permeability are negligible in the considered frequency range (the value of ε'' depends mainly on the optimized parameter equivalent to the collision frequency). The electric permittivity at the high-frequency limit of the structure is equal to 0.82, which is in good agreement with the physical requirement that the value of ε' should tend to unity in the limit $f \to \infty$. The wire structure is modeled as a single negative medium for frequencies between 7.5 and 14.9 GHz, and double positive medium in the frequency band 14.9 – 17.5 GHz (Tab. 3.4).

Table 3.4: Wire: frequency bands of the effective description obtained with PFDM.

Wire		
Modeled frequency range	7.5–17.5	GHz
SNG: $\mu' > 0$, $\varepsilon' < 0$	7.5–14.9	GHz
DPS: $\mu' > 0$, $\varepsilon' > 0$	14.9–17.5	GHz

The SRR and wire are the sub-components of the most interesting, double negative version of the SRR/wire metamaterial structure (Fig. 3.5c). With the assumed Drude characteristic for effective electric permittivity and Lorentz characteristic for effective magnetic permeability, the scattering parameters obtained with PFDM are very well matched

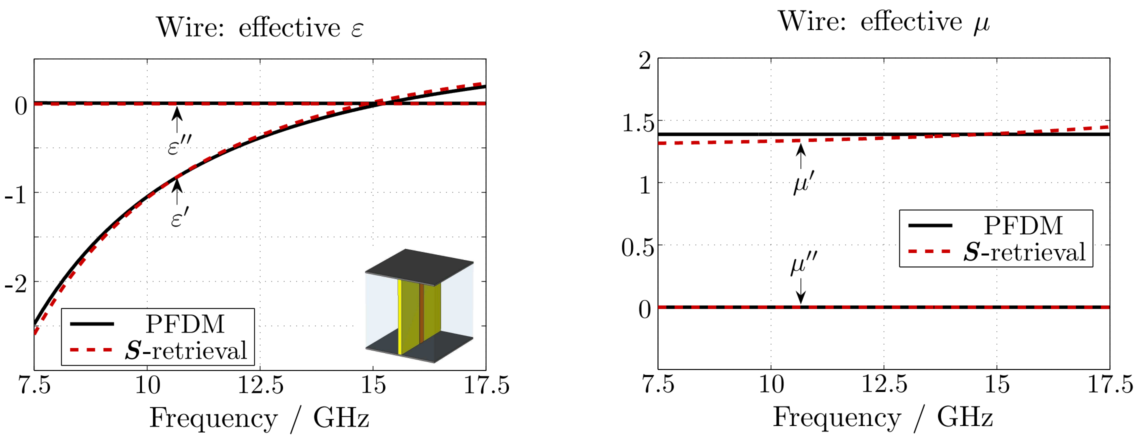

Figure 3.23: Effective constitutive parameters for a wire (Fig. 3.5b) extracted with PFDM (solid line). For comparison, $\boldsymbol{S}$-retrieved results from Fig. 3.8 are shown (dashed line).

to the reference results (Fig. 3.24). The corresponding optimized dispersive curves are shown in Figs. 3.25-3.26. While the effective magnetic permeability obtained by PFDM is indistinguishable from the $\boldsymbol{S}$-retrieved results, the effective electric permittivity optimized by PFDM eliminates the problem of non-physical negative values of ε'' retrieved from $\boldsymbol{S}$-parameters in the vicinity of the SRR resonance frequency. The effective magnetic permeability at the low- and high-frequency limit of the model is equal to 1.26 and 1.12, respectively, which is in good agreement with the physical requirement that these values should be close to unity (however, as with the BC-SRR structure, higher order resonances are expected in the spectrum above the high-frequency limit of the model). The electric permittivity of the Drude model at the high-frequency limit is equal to 1.62 which is a reasonable approximation of the physically expected value of unity. The relatively high value of the optimized damping frequency δ (1.24 GHz) influences the significant values of μ'' near the resonance, whereas the collision frequency ν_c (30.7 MHz) is reflected in the negligible values of ε''. The SRR/wire metamaterial is modeled as a double negative medium for the frequencies between 9.7 and 10.24 GHz. In the frequency band $10.24 - 11.6$ GHz single negative description is valid, whereas in the bands $7 - 9.7$ and $11.6 - 12$ GHz the structure is characterized by double positive parameters. The Drude/Lorentz description is valid for frequencies between 7 and 12 GHz (Tab. 3.5).

Table 3.5: SRR/wire: frequency bands of the effective description obtained with PFDM.

SRR/wire

Modeled frequency range	7–12	GHz
SNG: $\mu' > 0$, $\varepsilon' < 0$	7–9.7	GHz
DNG: $\mu' < 0$, $\varepsilon' < 0$	9.7–10.24	GHz
SNG: $\mu' > 0$, $\varepsilon' < 0$	10.24–11.6	GHz
DPS: $\mu' > 0$, $\varepsilon' > 0$	11.6–12	GHz

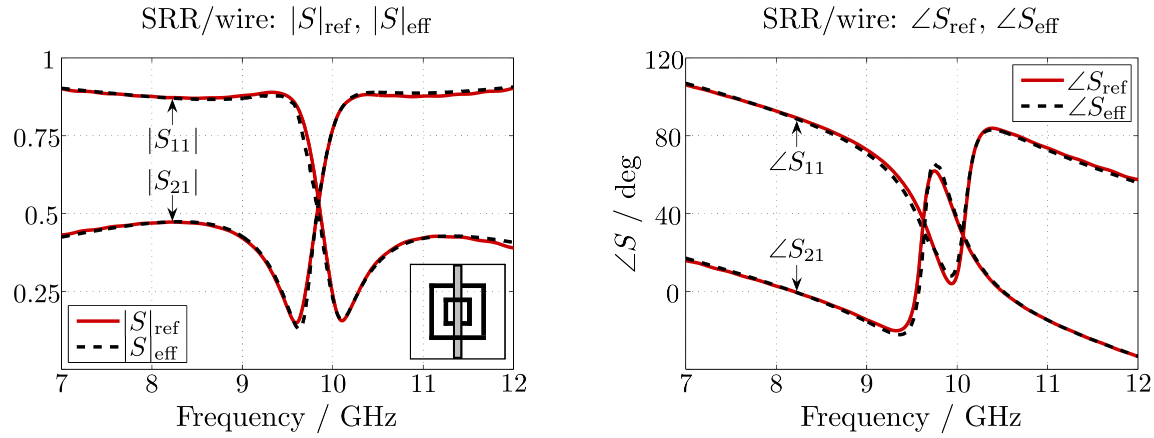

Figure 3.24: Scattering parameters of the homogenized double negative metamaterial (SRR/wire shown in Fig. 3.5c) fitted with PFDM (dashed line) to the reference results (solid line).

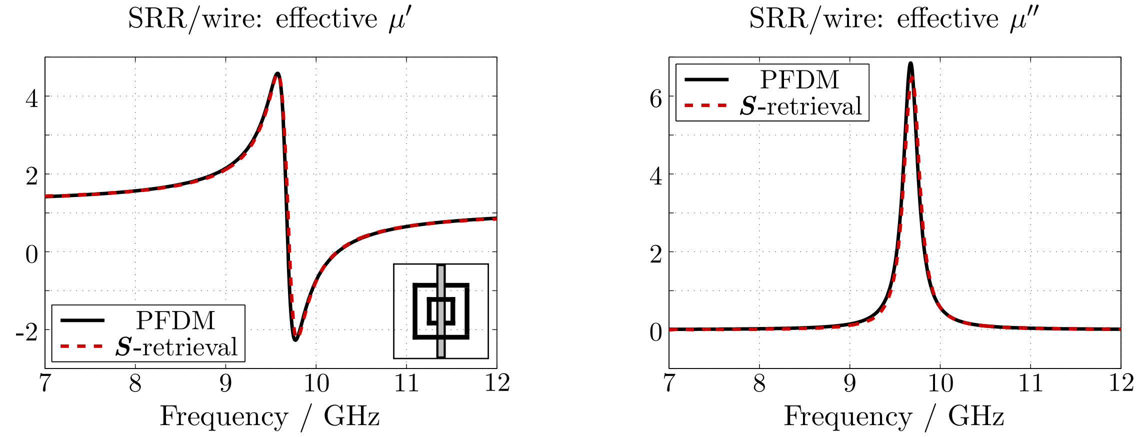

Figure 3.25: Effective magnetic permeability for a SRR/wire (Fig. 3.5c) extracted with PFDM (solid line). For comparison, $\boldsymbol{S}$-retrieved results from Fig. 3.7 are shown (dashed line).

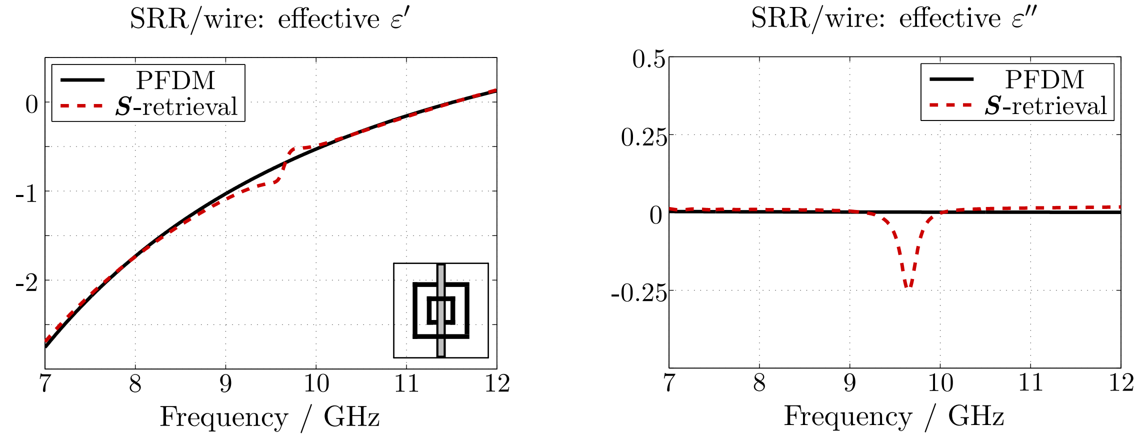

Figure 3.26: Effective electric permittivity for a SRR/wire (Fig. 3.5c) extracted with PFDM (solid line). For comparison, $\boldsymbol{S}$-retrieved results from Fig. 3.7 are shown (dashed line).

3.2.4 Discussion of Extraction Methods

The results presented in Sec. 3.2.1-3.2.3 allow general conclusions to be drawn regarding the extraction methods analysed in the frame of the effective medium approach.

The **S**-retrieval method allows one to extract effective parameters for every type of a metamaterial described by a 2-port model. However, for highly resonant structures, i.e. including various kinds of split ring resonators, the extracted constitutive parameters are most often non-physical.

On the other hand, the constitutive parameters delivered by fields averaging methods satisfy[5] physical requirements in the case of single negative resonant structures based on split ring resonators. However, these methods are not applicable in the case of metamaterials based on continuous wires. For such structures, the fields averaging methods require a modification of the metamaterial geometry that inevitably affects the EM properties of the medium. As most of the double negative MTM structures to date are based on the wire model that provides negative electric permittivity of the system, fields averaging methods cannot be directly applied to DNG designs. The alternative method combining FAM with eigenmode solver simulations does not solve the problem, as it does not deliver constitutive parameters in single negative bands and neglects imaginary parts of the effective description.

The method based on the parameter fitting of dispersive models allows one to avoid the common pitfalls of the **S**-retrieval and fields averaging methods. It can be applied to single as well as to double negative metamaterials containing continuous wires and highly resonant split ring resonators. Due to the application of predefined dispersive models the physical requirements for the constitutive description are always fulfilled. The PFDM implementation presented in the previous section is based on the Drude and Lorentz models, but in principle, arbitrary dispersive models can be used, including e.g. Debye model [5], or two-time derivative Lorentz model [174–176].

A priori assumed dispersive models of the PFDM method can be regarded as a limitation of the homogenization approach. However, due to the strong resonant behavior of metamaterial lattices, their effective constitutive parameters are typically close to the Lorentz shape, or in the case of a weak resonant behavior, close to the Drude type characteristic. Consequently, in most cases the predefined models capture the spectral properties of the metamaterial under test and are the natural choice for its effective description. However, for certain complex metamaterials the predefined models may constitute too simplified a picture. In such cases the **S**-retrieval method could be used as an indication of the resonance mechanism taking place in the MTM under test.

It should be kept in mind that the extracted material parameters represent the effective metamaterial properties for a certain polarization of the exciting field - in all analysed examples a plane wave excitation with the E_y and H_x field components is assumed, whereas the MTM geometry under test is properly oriented to show the desired single/double negative characteristic. Consequently, the extracted effective electric permittivity and magnetic permeability represent ε_{yy} and μ_{xx} principal axes components of the corresponding constitutive tensors.

The successful application of the parameter fitting of dispersive models method requires certain basic knowledge of EM properties of the system under test, including e.g. the character of the structure (single/double negative) or the type of electric and magnetic

---

[5] Depending on the particular implementation, see Sec. 3.2.2.

responses. This information can be easily obtained from the results delivered by the $\boldsymbol{S}$-retrieval method, or from dispersion diagrams computed through eigenmode solver simulations (Sec. 4.2).

Chapter 4

Bloch Analysis

In the previous section the problem of homogenization of metamaterial structures is approached from the point of view of the effective medium. As metamaterials do not rigorously satisfy the effective medium limit and are located conceptually between homogeneous materials and photonic crystals (cf. Fig. 1.1), in the present section they are analysed as lattices of periodically ordered single or double negative unit cells. The photonic crystal description of a periodic structure is valid for any ratio of the wavelength related to the scale of the inhomogeneity.

4.1 Homogenization of Photonic Crystals

A photonic crystal emerges from translations of its unit cell and can be characterized by a various set of structural symmetries (e.g. rotation, mirror-reflection, or inversion symmetry) called the point group of the crystal. Due to these symmetries, the infinite periodic lattice is represented by its irreducible Brillouin zone, i.e. a uniquely defined primitive cell of the reciprocal lattice that is reduced by all the symmetries in the point group of the lattice [52].

A typical example of a two-dimensional photonic crystal, consisting of a square lattice of dielectric columns embedded in free space, is shown in Fig. 4.1. The photonic crystal is periodic along the x, y axes and homogeneous (i.e. the rods are infinitely extended) along the z axis. The lattice has a square reciprocal zone in wave vector space, whereas the irreducible Brillouin zone is the triangular wedge (infinite in the z direction) in the upper-right corner - the rest of the Brillouin zone can be related to this wedge by rotational symmetry. The three special points Γ, X and M correspond to $\vec{k} = 0$, $\vec{k} = \frac{\pi}{a}\vec{e}_x$ and $\vec{k} = \frac{\pi}{a}\vec{e}_x + \frac{\pi}{a}\vec{e}_y$, respectively, and the propagation is limited to the z plane. The field solutions in the structure are separated into TE ($\vec{E}$ in the z plane) and TM ($\vec{H}$ in the z plane) modes [52]. In the analysed example, the dielectric rods embedded in free-space host are characterized by the radius $0.2a$, lattice constant[1] a equal to 1 cm and electric permittivity $\varepsilon = 11.4$.

Photonic crystals are typically characterized by band gap diagrams, called also dispersion diagrams. Dispersion diagrams are plotted from the pairs $\omega(\vec{k})$ that are obtained from the solution of the eigenvalue equation of a unit cell limited numerically with periodic

---

[1] Due to the scaling properties of Maxwell's equations, the absolute value of the lattice constant a is most often not relevant. The dispersion diagrams are typically shown in terms of the normalized quantities, e.g. normalized frequency $\frac{\omega a}{2\pi c_0}$ (note that $\frac{\omega a}{2\pi c_0}$ is equivalent to a/λ_0).

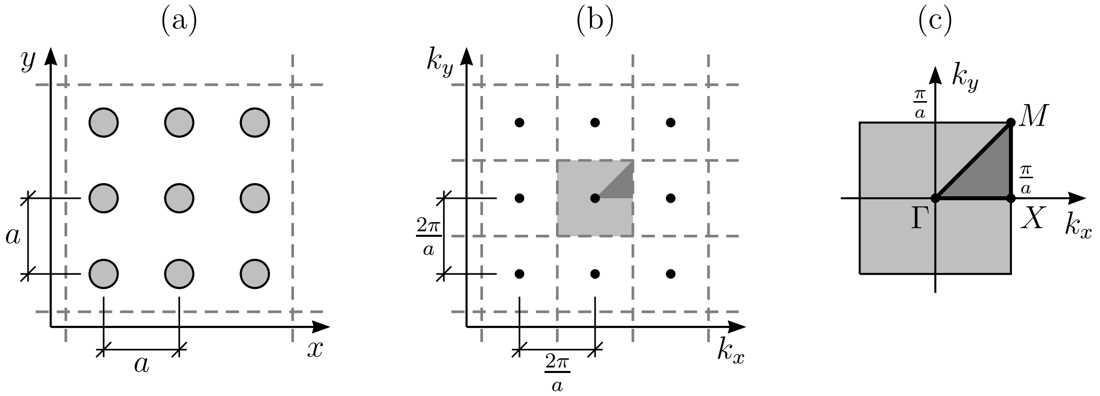

Figure 4.1: (a) Square lattice of a 2D photonic crystal - network of lattice points in real space. (b) Reciprocal lattice representation in wave vector space. The unit cell in the middle represents the Brillouin zone. (c) The enlarged view of the Brillouin zone. The dark gray area represents the irreducible part. The special points at the center, face and corner of the unit cell are conventionally depicted as Γ, X and M.

boundary conditions (this approach is referred to as PBE, i.e. periodic boundary eigenvalue problem). The assumed phase shift in the given direction (or directions) of periodicity in combination with the lattice constant imposes the Bloch[2] wave vector $\vec{k}$, whereas the computed ω values represent the eigenfrequencies of the analysed periodic lattice. The squared angular eigenfrequencies are equivalent to the eigenvalues of the system, whereas the corresponding eigenvectors represent the EM field distributions of the Bloch modes supported by the periodic structure. In case of the square lattice of dielectric rods, the eigenvalues of the system matrix are computed with the FIT eigenmode solver for the k_x and k_y values that cover the wave vector space of the irreducible Brillouin zone presented in Fig. 4.1c.

The dispersion diagram can be presented in various ways, depending on the application of the considered photonic crystal. Usually, the dispersion curve is represented by a 2D graph of eigenfrequencies on the edge of the first reduced Brillouin zone (Fig. 4.2). The dispersion diagram in a 3D form covers the entire Brillouin zone, where each band is represented by a curved sheet (Fig. 4.3). The 3D dispersion diagram includes much more information than the 2D version. For instance, it may be useful to consider the intersection of the sheets with a horizontal plane corresponding to the wavelength of interest. This leads to a curve in the wave vector plane (Fig. 4.4) called an isofrequency dispersion diagram [177] or an equifrequency surface [7].

The investigation of the dispersion relation of Bloch modes allows for prediction of some of the important properties specific to photonic crystals. From Fig. 4.2, the photonic crystal has a complete band gap for TM modes in the frequency range $0.29 < a/\lambda_0 < 0.41$. Up to the normalized frequency 0.29 there is one TM mode propagating in the lattice, whereas the frequency band of the second TM mode is limited to $0.41 - 0.54\ a/\lambda_0$.

From the isofrequency diagram one can determine the number of refracted waves and directions within the photonic crystal in which they propagate. The direction of propagation for a given mode in a 2D photonic crystal is normal to the contour of the isofrequency dispersion diagram and points towards the increasing values of ω on the sheet of Fig. 4.3,

---

[2] Propagation of EM fields in photonic crystals is represented by Bloch waves, in a similar way to plane waves in continuous materials.

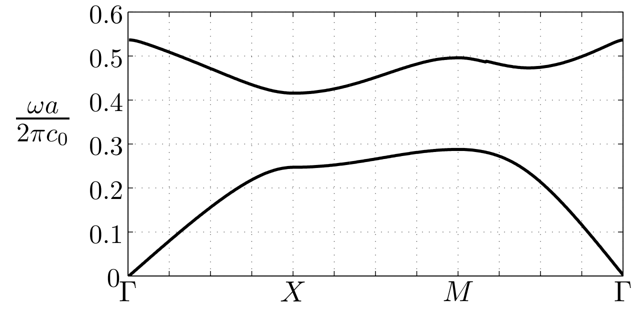

Figure 4.2: Two-dimensional dispersion diagram for TM polarization in a square lattice of dielectric rods from Fig. 4.1 (the first two TM modes are shown). The abscissa represents the Bloch wave vector on the edge of the first reduced Brillouin zone shown in Fig. 4.1c.

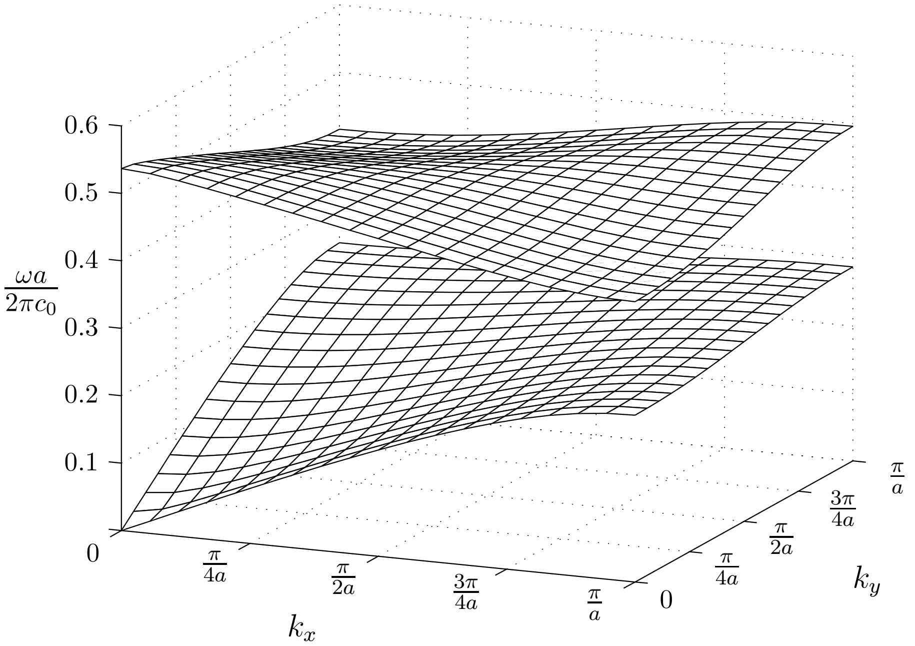

Figure 4.3: Three-dimensional dispersion diagram of the first two TM modes in a square lattice of dielectric rods from Fig. 4.1. The horizontal plane represents the components of the Bloch wave vector $\vec{k}$. The vertical axis gives the normalized frequency.

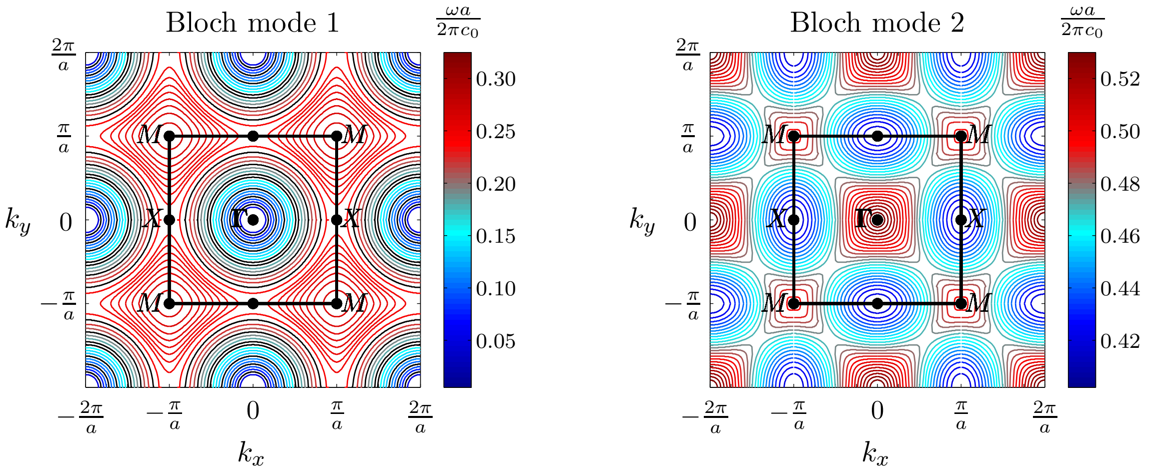

Figure 4.4: Isofrequency diagrams for the first two TM bands of a square lattice from Fig. 4.1. Each curve obtained from the intersection of the horizontal plane with the 3D dispersion diagram shown in Fig. 4.3 corresponds to a specific frequency.

according to the formula [177]:

$$\vec{v}_g = \frac{\partial \omega}{\partial k_x}\vec{e}_x + \frac{\partial \omega}{\partial k_y}\vec{e}_y. \tag{4.1}$$

From the shape of the isofrequency contours, a lot of interesting refraction and diffraction effects can be predicted, such as e.g. superprism or supercollimation effects [52, 178]. Also the negative refraction phenomenon can be predicted from these contours (observed e.g. in hexagonal lattices of dielectric rods [179]), although the mechanism behind it is conceptually different from the one occuring in metamaterials [58].

It was mentioned in Sec. 1.1 that in some cases the photonic crystals can be homogenized, i.e. their EM properties can be described by the effective refractive index[3] [7]. In order to consider the crystal lattice under test as a homogeneous material described by the effective optical index, the constant-frequency dispersion diagram should tend to a circle centered on the Γ point. The circular shape of the isofrequency diagram indicates that there are uniform propagation conditions in z plane, regardless of the particular direction of propagation. For the constant magnitude of the wave vector $\vec{k}$ in z plane, the effective refractive index can be assigned from the radius of the isofrequency contour [7].

In the analysed example of the square lattice of dielectric rods, the isofrequency curves in Fig. 4.4 are characterized by the circular shape for the frequencies up to 0.22 a/λ_0 (first mode) and above 0.52 a/λ_0 (second mode). In other words, in the frequency ranges $0-0.22$ a/λ_0 (long-wavelength limit) and $0.52-0.54$ a/λ_0 (upper band edge of the second mode, cf. [7]) the photonic crystal behaves as a continuous isotropic material and can be described by the effective refractive index. The circular shape of the isofrequency contours in the second mode range indicates that the photonic crystal can be homogenized for wavelengths comparable to the lattice period and well beyond the low-frequency limit.

From the observation of the circular isofrequency contours shown in Fig. 4.4 it can be noticed, that with growing frequency the constant-frequency circles of the first mode

---

[3] The effective properties of homogenized photonic crystals are typically described in terms of the refractive index, and not constitutive parameters ε and μ. Nonetheless, both descriptions are equivalent, as conventional photonic crystals (e.g. the one shown in Fig. 4.1a) are non-magnetic ($\mu_{\text{eff}} = 1$) and consequently $n = \sqrt{\varepsilon_{\text{eff}}}$. This may not hold for metamaterials.

expand gradually from the Γ point, whereas for the second mode they are successively more and more confined to the center of the Brillouin zone. In connection with (4.1), this has important consequences regarding respective directions of the phase and group velocities in the photonic crystal (for a thorough discussion see e.g. [7]). In case of the circular contours growing in size with frequency (first Bloch mode), the crystal lattice is characterized by the positive refractive index, whereas for the circular contours shrinking with frequency (second Bloch mode) the structure is described by the negative refractive index. This relationship can also be noticed from the 3D illustration of the dispersion diagram in the vicinity of the Γ point. The slope of the surface representing the first mode is positive near the center of the Brillouin zone which in connection with the circular shape of the isofrequency diagrams means that the wave vector $\vec{k}$ and group velocity $\vec{v}_g$ are parallel [forward wave, medium described by a positive refractive index, cf. (4.1)]. On the other hand, the negative slope of the second mode surface near the Γ point and the circular shape of the corresponding constant-frequency curves indicate that $\vec{k}$ and $\vec{v}_g$ are antiparallel for this mode in the frequency range $0.52 - 0.54\ a/\lambda_0$ [backward wave, medium characterized by a negative refractive index, cf. (4.1)].

4.2 Metamaterials as Photonic Crystals

In photonic crystals, the period of the lattice is typically comparable to the operating free-space wavelength (e.g. the complete photonic band gap of the Yablonovite crystal occurs for frequencies corresponding to the lattice constant $0.5 < a/\lambda_0 < 0.6$, see p. 83 in [52]). On the other hand, for metamaterials analysed in this work the ratio of the lattice constant to free-space wavelength is about $1/7 - 1/6$ for BC-SRR and SRR/wire, whereas it can approach $1/4$ in the case of the single negative wire medium (see Tab. 4.1). As most metamaterials are periodic structures[4] with a finite size of the unit cell, the methods used for the analysis of photonic crystals may also be valuable for the characterization of metamaterials.

Table 4.1: Lattice constant a related to free-space wavelength λ_0 for metamaterial structures analysed with the effective medium approach (Sec. 3.2). The frequency band describes the range corresponding to the extracted single/double negative constitutive parameters.

Structure	Fig.	Type	f / GHz	a / mm	a / λ_0
BC-SRR	3.5a	SNG	4.51 – 4.65	10	$\sim 1/7$
Wire	3.5b	SNG	< 14.9	5	$< 1/4$
SRR/wire	3.5c	DNG	9.7 – 10.24	5	$\sim 1/6$

The metamaterial lattice analysed as a photonic crystal is formed by the double negative SRR/wire based unit cells, used in the first experiments related to the negative refraction and described in Sec. 1.3 (Fig. 1.9a). The measurements of the lattice formed by three layers of metallic patterns printed on a substrate, reported in [14], were conducted for the structure inserted in the parallel plate waveguide that ensures a proper polarization of the

---

[4] In principle, metamaterials can be build as random mixtures of complex scatterers [93]. These structures, however, are less popular and not considered within this work.

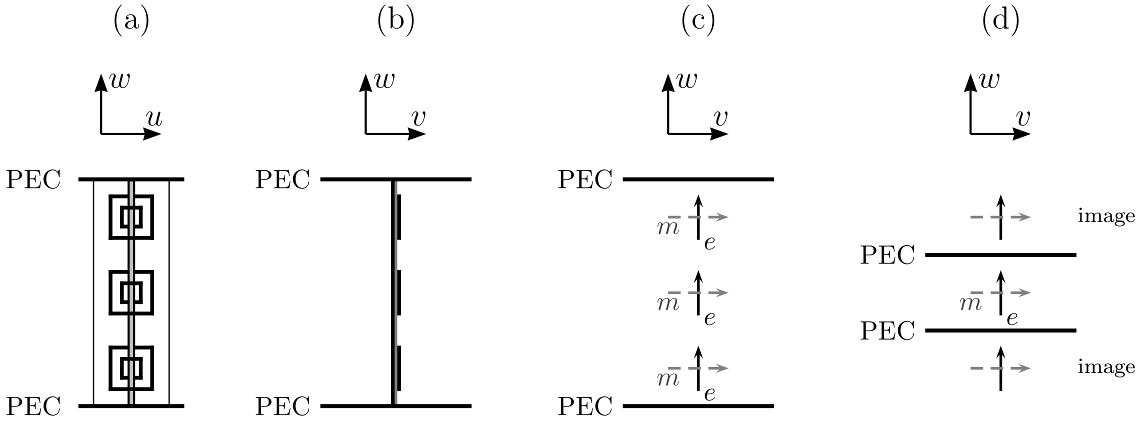

Figure 4.5: (a)/(b) Front/side view of a unit cell of the three-layered metamaterial lattice used in the negative refraction experiment (Fig. 1.9a). Field components in the structure: E_w, H_v, propagation in the u direction. (c) Equivalent representation of SRRs and wire by magnetic and electric dipoles. (d) Single layer model of the lattice, the top and bottom dipoles are represented by the corresponding images of the middle ones.

EM fields in the metamaterial (Fig. 1.9b). The PEC boundaries at the top and bottom of the three-layered periodic lattice allow to represent it by a single layer of SRRs and wires [according to the image theory the layers are effectively repeated in the vertical direction (Fig. 4.5)].

The corresponding top view of the lattice is shown in Fig. 4.6a. As the propagation in the negative refraction experiment is limited to the u direction (cf. Fig. 1.9b), the EM fields (E_w, H_v) interact mainly with the metallic inclusions patterned in the v plane and the lattice is effectively one-dimensional. This conclusion is supported by the study of transmission characteristics of parallel plate waveguides loaded with different orientations of split ring resonators (cf. EC-SRR configuration from Fig. 3.3d and the corresponding results shown in Fig. 3.4). Consequently, the two-dimensional metamaterial lattice can be modeled by its one-dimensional equivalent[5] shown in Fig. 4.6b. In the 2D case, the irreducible Brillouin zone of this lattice contains four characteristic points: Γ, X and M, analogous to the case of a square lattice of dielectric rods, and additional Y point representing the face of the unit cell in the v plane and resulting from the lack of a rotational symmetry of the MTM unit cell in the w plane (Fig. 4.6c). For the 1D representation and propagation in the MTM limited to the u direction, the relevant part of the irreducible Brillouin zone is its $\Gamma - X$ edge.

The band diagram of the metamaterial lattice, computed with the eigenmode solver and corresponding to the $\Gamma - X$ edge of the irreducible Brillouin zone is presented in Fig. 4.7. PEC limits the unit-cell structure (shown in Fig. 3.5c) at the w boundaries of the unit cell, whereas in the u and v directions periodic boundary conditions are used. The transversal wavenumber k_v is assumed equal to zero and k_u corresponding to the direction of propagation in the metamaterial is swept in the range $0 - \pi/a$.

---

[5] Indeed, recent works reported negative refraction phenomena observed in metamaterials with one-dimensional metallic patterns [111].

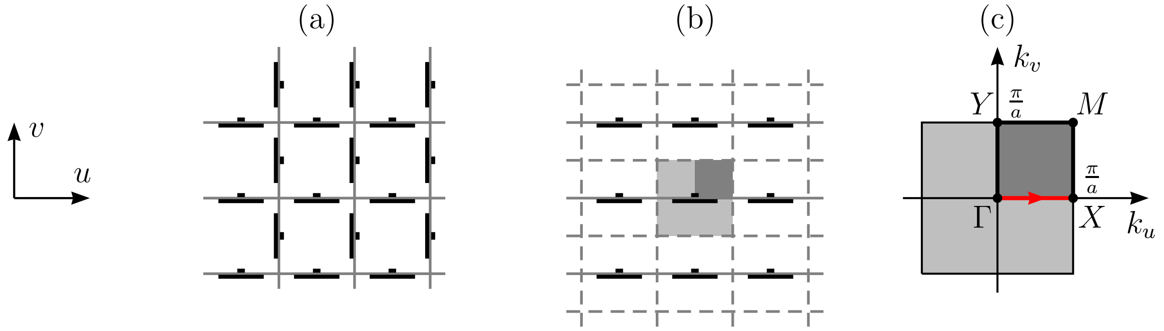

Figure 4.6: (a) Top view of a part of the SRR/wire metamaterial lattice. (b) Equivalent lattice model composed from the translated unit cells. The unit cell in the middle represents the Brillouin zone. (c) The enlarged view of the Brillouin zone. The dark gray area represents its irreducible part. The principal direction of propagation in the lattice is schematically depicted.

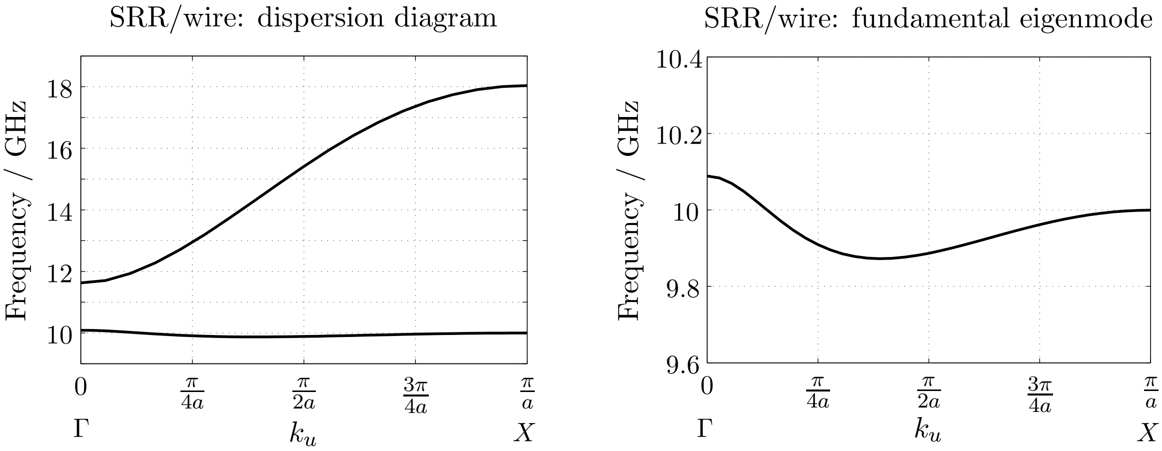

Figure 4.7: Dispersion diagram for the array of SRR/wires: first eigenmode range $9.9 - 10.1$ GHz (Δf-PBE), second eigenmode range $11.6 - 18$ GHz.

The dispersion diagram of the SRR/wire unit cell shows two eigenmodes supported by the lattice up to the frequency of 20 GHz. The fundamental mode, within the frequency range 9.9−10.1 GHz (Δf-PBE) is characterized by the negative slope of the dispersive curve, as long as the wave vector magnitude k_u is less than $\pi/(3a)$ (or equivalently, the electrical size of the unit cell a/λ_{m}, where λ_{m} is the wavelength in the medium, is smaller than 1/6). According to (4.1) the negative slope of the dispersive curve indicates that the propagating mode is a backward wave and the medium is characterized by a negative refractive index that corresponds to double negative constitutive parameters (see the discussion of isofrequency contours in Sec. 4.1). In the range $\pi/(3a) < k_u < \pi/(2a)$ ($1/6 < a/\lambda_{\mathrm{m}} < 1/4$) the dispersion curve tends to flatten, corresponding to a very low group velocity ($d\omega/dk \approx 0$) and longer time constants in the interaction between the metamaterial and the propagating wave [6]. Recent reports suggest, that this type of mode is composed of counterpropagating waves which results in the extremum away from the edge of the Brillouin zone [180]. For larger lattice constants [$k_u > \pi/(2a)$] the fundamental mode changes its character to the forward wave.

The second eigenmode is supported in 11.6 − 18 GHz range, and the positive slope of the dispersive curve indicates its forward type. In the frequency band of the second mode, the MTM structure is described by a positive effective refractive index equivalent to double positive constitutive parameters ($\varepsilon' > 0$ and $\mu' > 0$).

The frequency ranges obtained by eigenmode solver simulations and corresponding to single or double negative constitutive parameters (i.e. stopbands and passbands, respectively) are related to the results extracted with parameter fitting of dispersive models method in Fig. 4.8. From the figure it can be seen that the backward wave band of the first eigenmode Δf-PBE (9.9 − 10.1 GHz) fits in the double negative frequency range Δf-PFDM (9.7 − 10.24 GHz) extracted from scattering matrix. Moreover, the frequency band of the second eigenmode matches the double positive constitutive parameters between 11.6 and 12 GHz (note that the predefined Drude/Lorentz description is valid in the spectrum range 7 − 12 GHz). The results of both approaches summarized in Tab. 4.2 show a good agreement between the solution of the periodic boundary eigenvalue problem and the effective description extracted from scattering parameters. The discrepancy between the frequency bands related to the DNG range (Δf-PBE vs Δf-PFDM) is discussed in Chapter 5.

Table 4.2: SRR/wire: frequency bands of single/double negative constitutive parameters extracted with PFDM vs solution of the PBE problem. (PFDM is valid in the range 7 − 12 GHz).

PFDM		PBE			
description type	Δf / GHz	band	eigenmode	wave	Δf / GHz
SNG: $\mu' > 0$, $\varepsilon' < 0$	7−9.7	stopband	–	–	<9.9
DNG: $\mu' < 0$, $\varepsilon' < 0$	9.7−10.24	passband	first	backward	9.9−10.1
SNG: $\mu' > 0$, $\varepsilon' < 0$	10.24−11.6	stopband	–	–	10.1−11.6
DPS: $\mu' > 0$, $\varepsilon' > 0$	11.6−12	passband	second	forward	11.6−18

The band diagrams are also computed for single negative metamaterials, i.e. BC-SRR (Fig. 3.5a) and wire (Fig. 3.5b) unit cells analysed in Sec. 3.2 (field polarization and the direction of propagation are assumed analogous to the case of the SRR/wire unit cell).

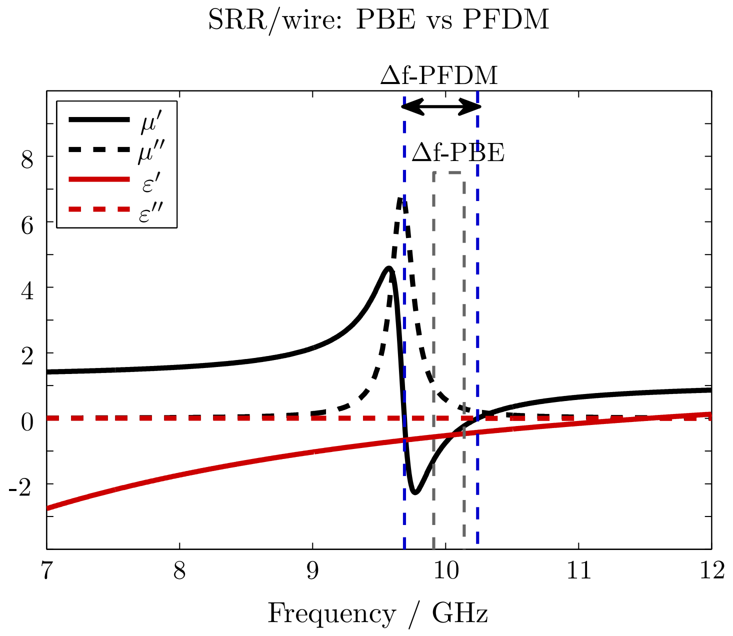

Figure 4.8: Double negative frequency range extracted from scattering parameters (Δf-PFDM) vs frequency band of the first eigenmode (Δf-PBE) for the SRR/wire structure.

The dispersion diagram obtained for the broadside-coupled split ring resonator is shown in Fig. 4.9. Up to the frequency of 4.51 GHz, there is one mode in the periodic structure, and the positive slope of its dispersion curve indicates the forward wave type. The first band gap occurs for frequencies between 4.51 and 4.65 GHz and matches the single negative frequency band obtained by the PFDM method as shown in Fig. 4.10. The second eigenmode propagates in the lattice in the spectrum range 4.65 – 10.3 GHz and is also characterized by $\partial\omega/\partial k_u > 0$. The frequency bands of both forward waves correspond to double positive constitutive parameters of the BC-SRR effective description. A good agreement between PFDM and PBE is summarized in Tab. 4.3.

Table 4.3: BC-SRR: frequency bands of single negative constitutive parameters extracted with PFDM vs solution of the PBE problem. (PFDM is valid in the range 4 – 5 GHz).

PFDM		PBE			
description type	Δf / GHz	band	eigenmode	wave	Δf / GHz
DPS: $\mu' > 0$, $\varepsilon' > 0$	4–4.51	passband	first	forward	<4.51
SNG: $\mu' < 0$, $\varepsilon' > 0$	4.51–4.65	stopband	–	–	4.51–4.65
DPS: $\mu' > 0$, $\varepsilon' > 0$	4.65–5	passband	second	forward	4.65–10.3

The dispersion diagram of a wire unit cell is shown in Fig. 4.11a. The first eigenmode of the periodic lattice describes the structure in the frequency range 14.9 – 24.8 GHz and is characterized by the positive slope of the dispersion curve that corresponds to the forward wave type. This eigenmode starts to propagate at the frequency where effective electric permittivity ε' changes its sign from negative to positive (Fig. 4.11b), which means that the solution of the eigenvalue problem is in agreement with the effective description extracted

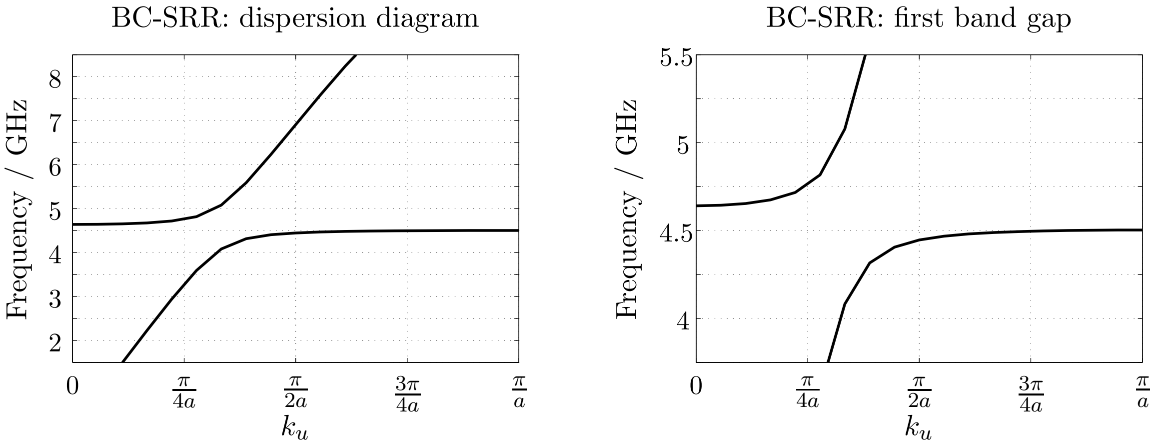

Figure 4.9: Dispersion diagram for the array of BC-SRRs: first band gap range $4.51 - 4.65$ GHz.

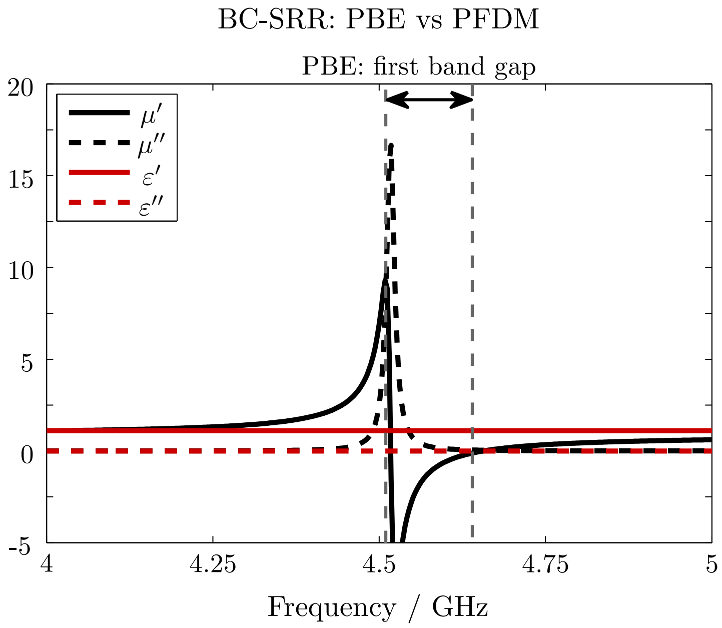

Figure 4.10: Frequency band of the first band gap for the BC-SRR structure, related to the effective constitutive description extracted from scattering parameters with PFDM.

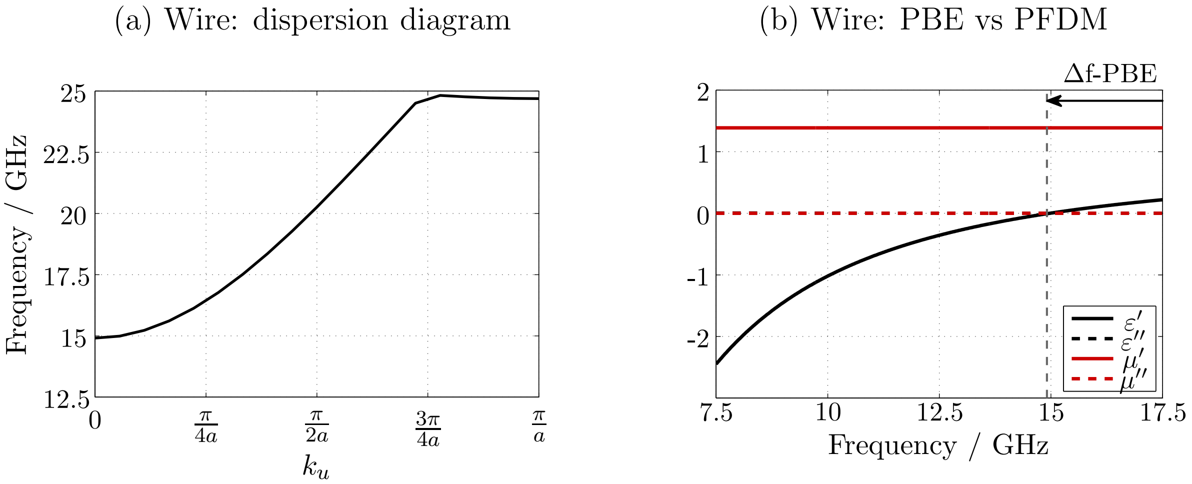

Figure 4.11: (a) Dispersion diagram for the array of wires: first eigenmode range 14.9 – 24.8 GHz (Δf-PBE). (b) Frequency band of the first eigenmode related to the effective constitutive description extracted from scattering parameters with PFDM.

from time-domain simulations. The results of PFDM and PBE approaches applied to the wire unit cell are summarized in Tab. 4.4.

Table 4.4: Wire: frequency bands of single negative constitutive parameters extracted with PFDM vs solution of the PBE problem. (PFDM is valid in the range 7.5 – 17.5 GHz).

PFDM		PBE			
description type	Δf / GHz	band	eigenmode	wave	Δf / GHz
SNG: $\mu' > 0$, $\varepsilon' < 0$	7.5–14.9	stopband	–	–	<14.9
DPS: $\mu' > 0$, $\varepsilon' > 0$	14.9–17.5	passband	first	forward	14.9–24.8

The solution of a periodic boundary eigenvalue problem presents a valuable tool that allows one to identify frequency ranges of forward and backward waves in a lattice, corresponding to double positive and double negative constitutive parameters, respectively. On the other hand, the band gaps represent the frequencies at which the structure is characterized by single negative parameters. Therefore, a PBE solution can be used for validation of the effective parameters extracted from a scattering matrix. Moreover, it can be used for extraction of the effective refractive index for the metamaterial structure under test. The band diagrams obtained with PBE approach are also useful in the design of metamaterial based arrays, e.g. metamaterial loaded waveguides.

4.3 Metamaterial Loaded Waveguides

To show the usefulness of the photonic crystal approach to the modeling of metamaterial structures, several MTM loaded waveguides have been designed, manufactured and measured, with respect to different potential applications including[6] [181]:

---

[6] This work was conducted in the scope of the Dipl.-Ing. thesis of Bastian Bandlow, co-supervised by the author and Dipl.-Ing. Christian Damm, in cooperation with Prof. Dr.-Ing. Rolf Jakoby and Dr.-Ing. Martin

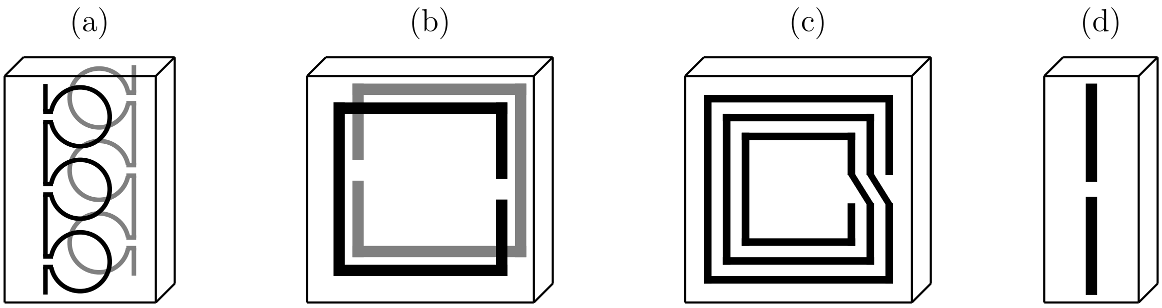

Figure 4.12: Topologies of the metamaterial structures loading the waveguide. (a) Ω-particle, (b) BC-SRR, (c) spiral resonator, (d) electric dipole element. The dimensions of the particular geometries are given in [182–185].

(a) subwavelength waveguide filters [182, 183]

(b) miniaturized subwavelength waveguides [184],

(c) metamaterials as transversal or longitudinal dipoles loading the waveguides [185].

The term subwavelength waveguide in this context means a rectangular waveguide loaded with a metamaterial array and operating in the frequency regime below the cutoff frequency of the hollow structure, i.e. for wavelengths significantly longer than the cross-sectional dimensions of the waveguide [186, 187].

In the frame of this study different resonant and non-resonant inclusions are considered, including Ω-particles, BC-SRRs, spiral rings and electric dipole elements (Fig. 4.12). Ω-element is a bianisotropic realisation of an inductively loaded wire used in the frequency selective surfaces and filters [188]. The double-sided configuration shown in Fig. 4.12a minimizes the bianisotropic effects in the structure. BC-SRR is a modified version of a split ring resonator, where the magnetoelectric coupling effects are avoided and which does not present bianisotropic effects [13]. Spiral resonators are well-known structures in microwave engineering, commonly used as lumped inductors, usually in the presence of a ground plane. The usefulness of planar spiral rings for the design of artificial magnetic media relies on the significant reduction in the electrical size of the MTM unit cell [189]. The array of dipole elements printed on a dielectric substrate forms a frequency selective surface that can lower the cutoff frequency of the dominant waveguide mode when placed in its symmetry plane [190].

As the housing a standard X-band rectangular waveguide with the dimensions 22.86 mm × 10.16 mm and TE_{10} mode cutoff frequency 6.56 GHz is chosen. The 11 cm long X-band waveguide used in the experiments was milled from a brass block and plated with gold to provide good conductivity. The experimental set-up shown in Fig. 4.13 is equipped with coaxial connectors fixed to the casing with the threaded screws. There is a possibility to close the waveguide at both ends by using metal plates. The metallic inclusions are etched in the dielectric laminate and inserted in the symmetry plane of the waveguide - there is a slot along the waveguide suited to the thickness of the dielectric substrate that ensures its centered and stable position.

Schüßler, Fachgebiet für Mikrowellentechnik at TU Darmstadt.

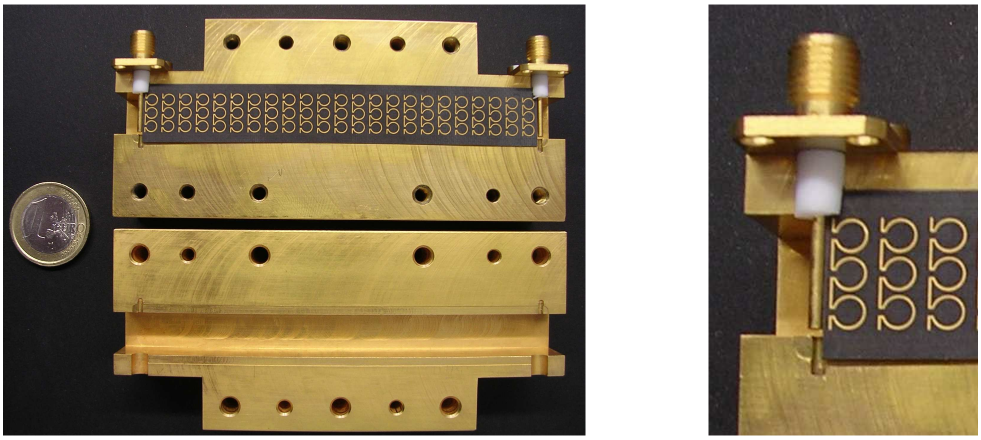

Figure 4.13: X-band waveguide used in the experiments with attached coaxial connectors and inserted array of 23 Ω-cells [182].

The computer-aided analysis (CAA) process involves simulations of the MTM unit cells shown in Fig. 4.12 with the eigenmode solver, assuming PEC boundary conditions in the transversal directions of the structure (equivalent to the PEC walls of the rectangular waveguide used in the experiments) and periodic boundary conditions in the direction of propagation. The geometrical dimensions of the unit cells inclusions are optimized regarding various optimization goals, according to the passbands and stopbands obtained from dispersion diagrams. In the next CAA step, based on the time-domain solver simulations, the geometry of the coaxial excitation part is tuned for a proper matching at the input and output to the MTM loaded waveguide. The final design step consists of the time-domain simulation of the entire waveguide geometry, including coaxial connectors and metamaterial arrays loading the waveguide. The CAA procedure delivers dispersion diagrams of the modes propagating in the array as well as transmission characteristic of the metamaterial loaded waveguide.

The simulation and measurement results of the different types of MTM inclusions show that depending on the required transmission characteristic, it is possible to obtain a user defined frequency band below the cutoff frequency of the hollow waveguide [183]. If a broad bandwidth of a passband filter is required, Ω-type scatterers can be used [182]. The geometry of the Ω-element is optimized for minimization of the goal function $G = 1 - \frac{|f_1 - f_2|}{f_c}$, where f_1 and f_2 denote the eigenfrequencies of the second mode corresponding to 0 and π/a values of the wavenumber k_u and f_c is the cutoff frequency of the hollow waveguide. The dispersion diagram of the optimized geometry shown in Fig. 4.14a indicates two modes below the waveguide cutoff, in the bands $3.22 - 3.26$ GHz and $3.82 - 6.44$ GHz. The simulated and measured transmission characteristics of the waveguide loaded with the array of 23 Ω-elements presented in Fig. 4.14b show that the first mode is not excited in the waveguide, whereas the second mode band (relative bandwidth 50%) is in very good agreement with the S_{21} parameter.

The same optimization procedure is applied to a BC-SRR array shown in Fig. 4.15. Below the cutoff frequency of the hollow waveguide, there are two propagating modes, in accordance with the eigenmode solver simulations shown in Fig. 4.16a. The first mode in the frequency range $1.74 - 2.52$ GHz is a backward wave with the relative bandwidth of 36%, whereas the second mode for frequencies $3.02 - 4.53$ GHz is a forward wave with the relative

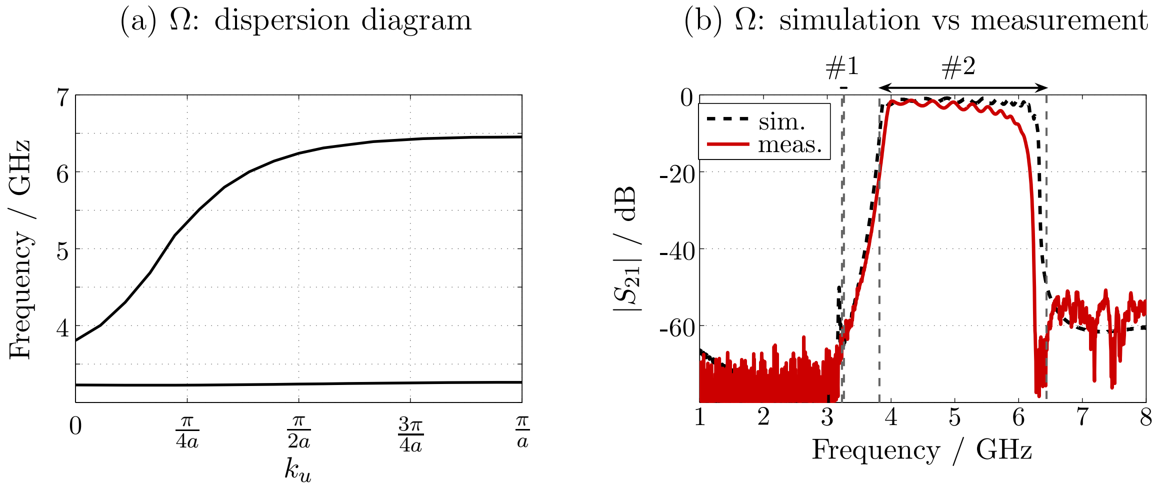
(a) Ω: dispersion diagram

(b) Ω: simulation vs measurement

Figure 4.14: Simulation and measurement results of the waveguide loaded with the Ω-structure [182]. (a) Dispersion diagram: first eigenmode 3.22 − 3.26 GHz, second eigenmode 3.82 − 6.44 GHz. (b) Frequency bands of the two eigenmodes related to the simulated and measured transmission characteristics. The first mode is not excited.

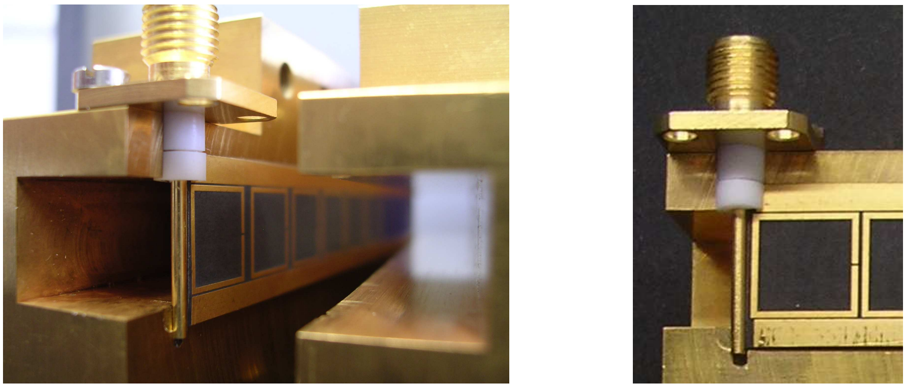

Figure 4.15: Fabricated array of 10 BC-SRRs acting as transversal magnetic dipoles and inserted in the X-band waveguide [182].

bandwidth of 40%. The different type of the propagating modes is an interesting property - by switching between the modes one could change the character of the propagating wave, that is used e.g. for frequency scanning from negative (backward wave) to positive (forward wave) angles of radiation in metamaterial based leaky-wave antennas [191]. The measured transmission characteristic of a waveguide loaded with 10 BC-SRR elements shown in Fig. 4.16b validates the simulation results obtained with both eigenmode and time-domain solvers.

The metamaterial loaded waveguides operating for frequencies far below cutoff can be applied as miniaturized waveguides. This application is proposed e.g. in [192], where ring inclusions loaded with lumped capacitors are used in order to obtain high miniaturization ratios. The additional lumped capacitors loading the rings provide the reduction of the metamaterial resonance frequency, but on the other hand they are bulky and complicate the fabrication process. The introduction of lumped elements can be avoided by using resonant structures characterized by small resonance frequency, e.g. spiral resonators (Fig. 4.12c) [184]. Due to their uniplanar character, spiral resonators are easy to manufacture and allow

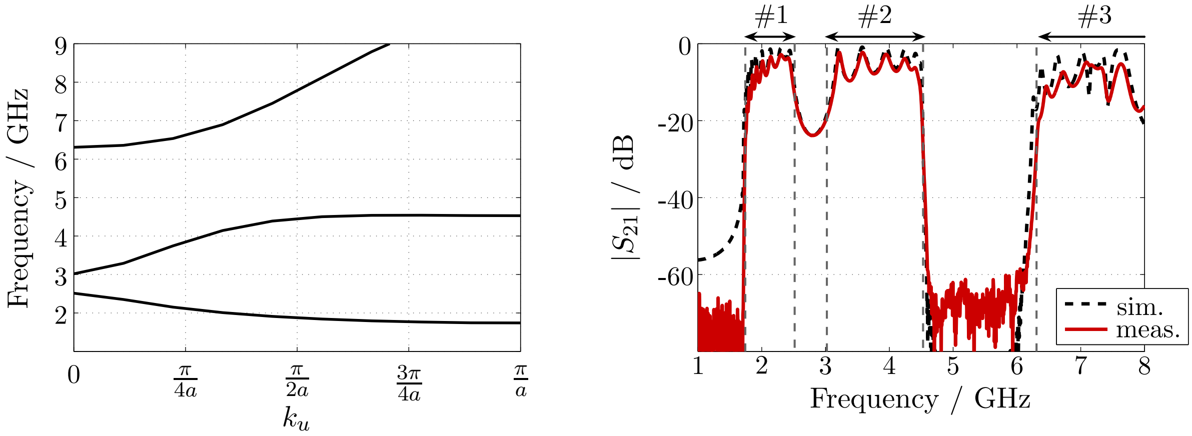
(a) BC-SRR (transversal magnetic dipole): dispersion diagram

(b) BC-SRR (transversal magnetic dipole): simulation vs measurement

Figure 4.16: Simulation and measurement results of the waveguide loaded with the array of transversally oriented BC-SRRs [182]. (a) Dispersion diagram: first eigenmode $1.74 - 2.52$ GHz, second eigenmode $3.02 - 4.53$ GHz, third eigenmode $6.31 - 9.90$ GHz. (b) Frequency band of the three eigenmodes related to the simulated and measured transmission characteristics.

for a significant reduction of the electrical size of the unit cell when compared e.g. with split ring resonators. Moreover, introduction of additional turns in the spiral structure makes it possible to increase the equivalent capacitance and reduce the resonant frequency of the metamaterial.

The geometry of the spiral resonator designed in the frame of this study is optimized for high miniaturization ratio, i.e. for minimization of the goal function $G = f_1/f_c$, where f_1 denotes the center frequency of the first mode band and f_c is the cutoff frequency of the hollow waveguide. The spectrum range of the first mode $0.68 - 0.80$ GHz is characterized by the negative slope of the dispersive curve (Fig. 4.17a) and the relative bandwidth of 17%. Below the waveguide cutoff, the dispersion diagram indicates several other eigenmodes of the forward type (#2 : $2.24 - 2.25$ GHz, #3 : $3.55 - 3.79$ GHz, #4 : $4.08 - 5.36$ GHz, #5 : $5.56 - 7.07$ GHz). Due to the field distribution of the particular eigenmodes, not all of them are excited in the designed configuration of 9 spiral rings loading the waveguide, e.g. the second mode in the range $2.24 - 2.25$ GHz is not excited in the structure. This can be noticed in the simulated and measured transmission characteristics shown in Fig. 4.17b, where a very good agreement between both S_{21} curves is observed, supported by the frequency bands of particular modes predicted by the PBE approach. The first mode of the fabricated structure shown in Fig. 4.18a provides the miniaturization ratio (f_c/f_1) of the order of 10 [184].

An experimental demonstration of the transmission below the cutoff frequency of a rectangular waveguide filled with an array of split ring resonators was one of the first applications of the negative magnetic permeability structures [186, 187]. Initially, the hollow waveguide below the cutoff frequency of the fundamental mode was considered as an equivalent of a negative electric permittivity material, whereas the array of SRRs represented a negative magnetic permeability structure. When the frequency range for a negative μ' of the SRRs array was chosen below the cutoff frequency of the waveguide, one obtained

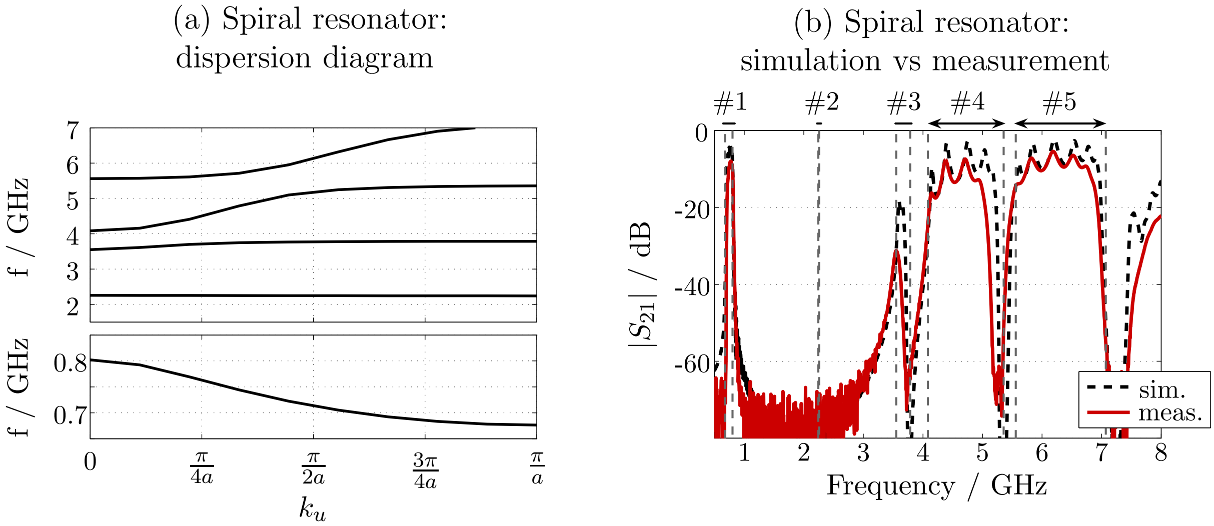

Figure 4.17: Simulation and measurement results of the waveguide loaded with the array of spiral resonators [184]. (a) Dispersion diagram, eigenmodes: #1 0.68−0.80 GHz, #2 2.24−2.25 GHz, #3 3.55 − 3.79, #4 4.08 − 5.36 GHz, #5 5.56 − 7.07 GHz. (b) Frequency bands of the five eigenmodes related to the simulated and measured transmission characteristics.

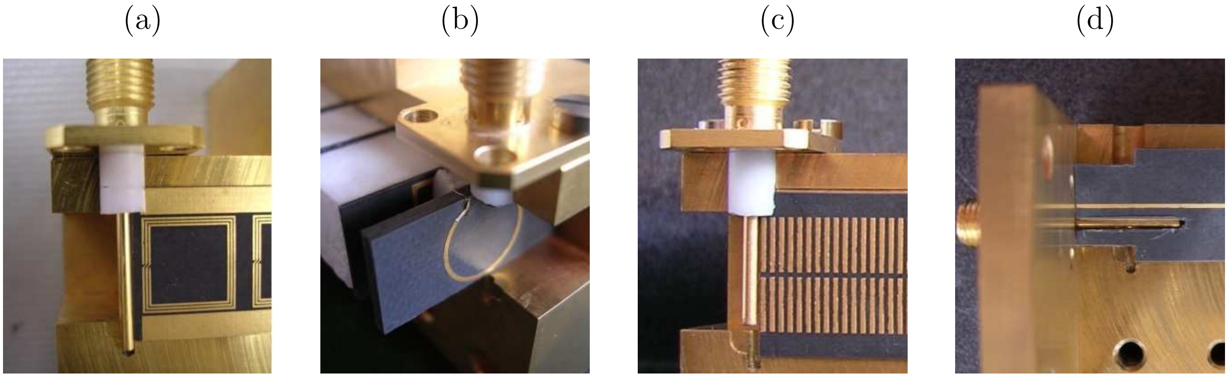

Figure 4.18: (a) Spiral resonator. (b) Loop excitation of the longitudinally oriented magnetic dipole implemented in the form of a BC-SRR. (c) Transversal electric dipole. (d) Longitudinal electric dipole. After [185].

an equivalent of a double negative material. The propagating wave in this case was of the backward type, and the array of SRRs was applied to the design of subwavelength waveguides.

However, it was shown in the later studies that the passband below the cutoff frequency of a rectangular waveguide loaded by resonant scatterer chains is caused by the properties of the periodic array itself and has nothing to do with double negative media [193]. The backward wave that appears for frequencies below the waveguide cutoff in a special case of transversally oriented magnetic scatterers is not a necessary attribute of such a passband - in a similar way the double negative constitutive description is not a prerequisite for a transmission band below cutoff. The four possible cases of scatterer orientation with respect to the waveguide walls, analysed theoretically in [193] and consisted of transversally and longitudinally oriented magnetic and electric dipoles, are shown in Fig. 4.19a.

The theoretical predictions given in [193] are confirmed experimentally in the frame of the present work on metamaterial loaded waveguides [185]. The transversally and longitudinally oriented magnetic and electric dipoles are realized in the form of BC-SRRs and narrow microstrips and gaps, respectively, as shown in Fig. 4.19b. The dimensions of the array elements are optimized with the PBE approach in order to provide propagation of the fundamental modes below the cutoff frequency of the hollow waveguide. In Fig. 4.19c the field patterns of the fundamental modes in the analysed cases are shown. For the transversally oriented magnetic dipole the dominant component of the magnetic field is H_u, whereas for the longitudinal magnetic dipole it is H_w. In the case of electric dipoles the electric field is concentrated in the gaps between metallic strips, pointing along the strips. For the transversal orientation of the electric dipole the dominant component is E_v, whereas in the longitudinal case it is E_w. The field distributions correspond to the fundamental modes obtained with the PBE approach and illustrated in the form of dispersive curves in Figs. 4.16a, 4.20a, 4.21a and 4.22a.

The transversally oriented magnetic dipole is already described in the context of a broadband transmission below the waveguide cutoff. The dispersion diagram and transmission characteristics shown in Fig. 4.16 are in very good agreement and indicate that there are two modes propagating below the waveguide cutoff. The first mode in the frequency range $1.74 - 2.52$ GHz is a backward wave, whereas the second one is of no importance for the present analysis (the field of this mode is concentrated between the top/bottom of the BC-SRR and the top/bottom of the enclosing waveguide).

The array of longitudinally oriented magnetic dipoles is excited by the loop etched in a planar substrate, shown in Fig. 4.18b. The loop geometry is optimized for a proper excitation of the first mode in the structure, which is a forward wave propagating in the spectrum range $1.90 - 1.96$ GHz and characterized by the dominant longitudinal component of the magnetic field. The dispersion diagram shown in Fig. 4.20a indicates two modes below the waveguide cutoff, the second mode, however, is of no importance here. The fabricated array consists of 9 BC-SRRs inserted in the rectangular waveguide and separated with the Rohacell 71 foam providing equal spacing and stable mechanical position, as shown in Fig. 4.23a. The simulated and measured transmission characteristics confirm the results predicted from eigenmode solver simulations (Fig. 4.20b). The discrepancy between the simulated and experimental S_{21} in the range $4.7 - 6$ GHz is caused by the mechanical inaccuracy by closing the BC-SRRs and foam in the waveguide housing.

The array of transversally oriented electric dipoles consists of 118 unit cells composed of vertically oriented metallic strips (a part of the structure is shown in Fig. 4.18c). The

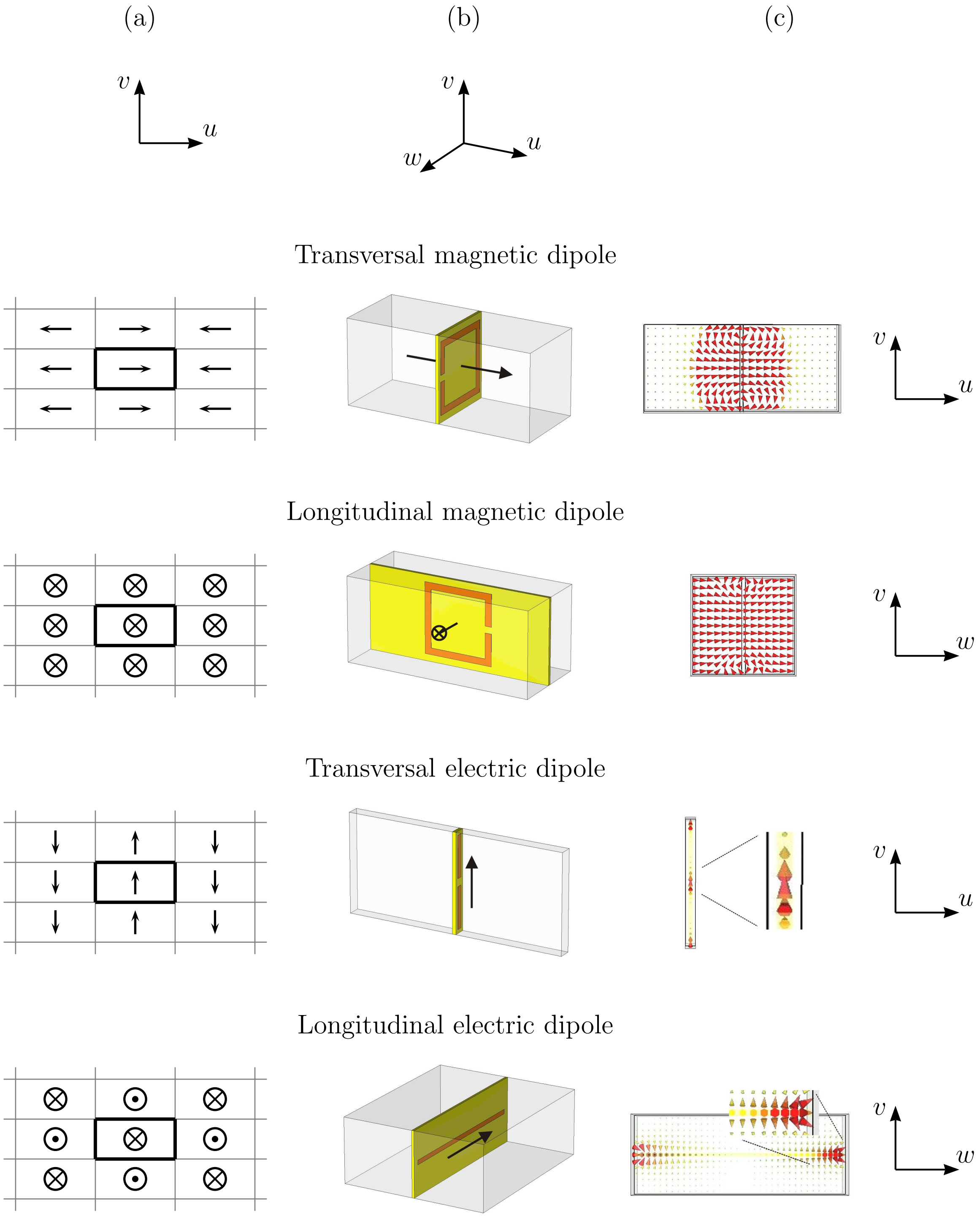

Figure 4.19: Rectangular waveguide loaded with magnetic and electric dipole arrays [185]. (a) Transformation of the waveguide problem to the lattice one based on the image principle proposed in [193]. (b) Unit cells of the MTM arrays loading the waveguide. (c) Field pattern of the first mode obtained by eigenmode solver simulations.

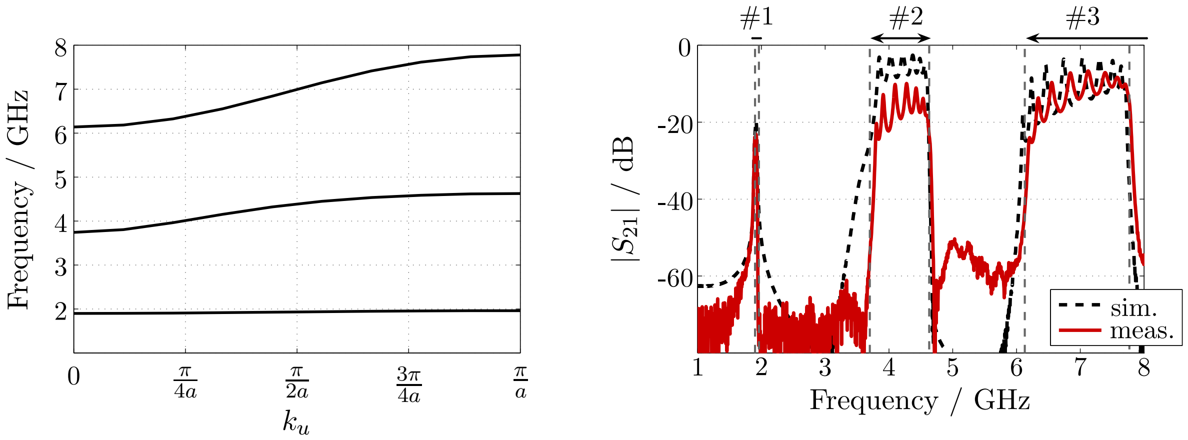

(a) BC-SRR (longitudinal magnetic dipole): dispersion diagram

(b) BC-SRR (longitudinal magnetic dipole): simulation vs measurement

Figure 4.20: Simulation and measurement results of the waveguide loaded with the array of longitudinally oriented BC-SRRs [185]. (a) Dispersion diagram, eigenmodes: first $1.90-1.96$ GHz, second $3.74-4.63$ GHz, third $6.14-7.78$ GHz. (b) Frequency band of the three eigenmodes related to the simulated and measured transmission characteristics.

electric field is oriented vertically and concentrated in the gaps between the strips. This configuration reduces the cutoff frequency from 6.56 GHz in the case of the hollow waveguide to 4.77 GHz in the case of the loaded one. The dispersion diagram shown in Fig. 4.21a reveals the frequency band $4.77-23.9$ GHz and the forward wave type of the fundamental mode. The transmission characteristics confirm the cutoff frequency of the loaded waveguide (Fig. 4.21b). The small shift in frequency between the simulated and measured S_{21} curves is caused by the inaccuracies in positioning the fabricated dipole array in the experimental waveguide.

In the case of longitudinally oriented electric dipoles the coaxial excitation is placed parallel to the array elements and the coupling from the coaxial line to the loaded waveguide takes place through the magnetic field (excitation part of the structure is shown in Fig. 4.18d). Due to the physical limitations of the housing, in order to provide a transmission band below the waveguide cutoff only 4 metallic strips are used in the array (Fig. 4.23b). The dispersion diagram shown in Fig. 4.22a indicates a single mode up to the cutoff frequency of the hollow waveguide, in the frequency range $4.11-5$ GHz and of the forward wave type. The simulated and measured transmission characteristics are in good agreement and validate the eigenmode solver results (Fig. 4.22b). From the presented S_{21} curves it can be noticed that the second mode of the structure, related to the TE_{10} field solution of the hollow rectangular waveguide, is not observed due to the applied excitation geometry. The transmission peaks in the range of the second mode are related to internal resonances introduced by the longitudinally oriented probe excitation.

The work of Belov and Simovski [193] predicts propagation of a backward wave in the arrays of transversally oriented magnetic dipoles, and a forward wave in all remaining cases, i.e. for longitudinally oriented magnetic dipoles and transversally or longitudinally oriented electric dipoles. Furthermore, the bandwidth of the eigenmodes in the case of longitudinally oriented dipoles is expected to be significantly narrower than for their transversal orientation. The results obtained experimentally in the frame of this work fully confirm the theoretical predictions given in [193] and show that the waves propagating in a loaded

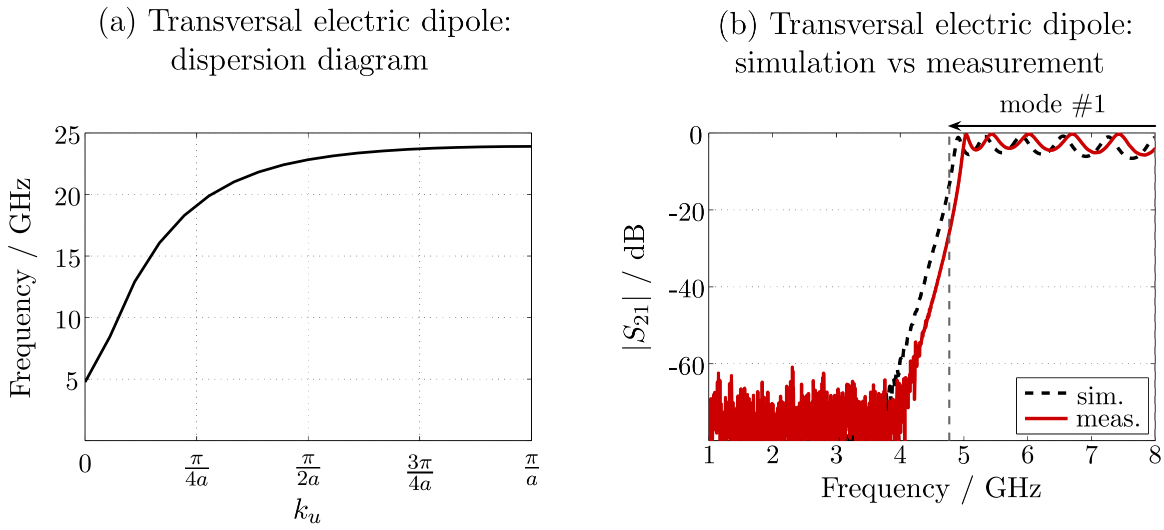

Figure 4.21: Simulation and measurement results of the waveguide loaded with the array of transversal electric dipoles [185]. (a) Dispersion curve of the first eigenmode supported for frequencies between 4.77 – 23.9 GHz. (b) Frequency band of the first eigenmode related to the simulated and measured transmission characteristics.

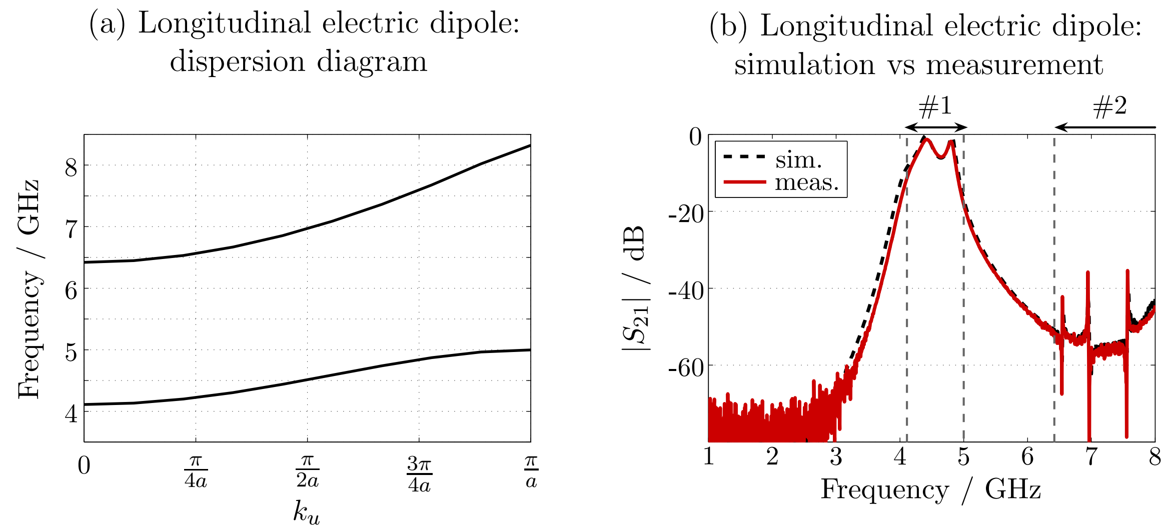

Figure 4.22: Simulation and measurement results of the waveguide loaded with the array of longitudinally oriented electric dipoles [185]. (a) Dispersion diagram, eigenmodes: first 4.11 – 5 GHz, second 6.42 – 8.32 GHz. (b) Frequency band of the two eigenmodes related to the simulated and measured transmission characteristics. The second mode is not excited.

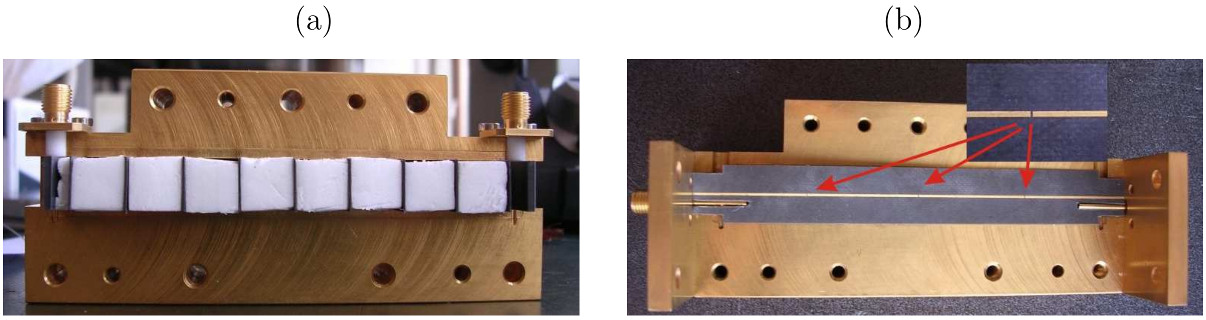

Figure 4.23: (a) Array of 9 longitudinally oriented BC-SRRs inserted in the waveguide. The unit cells are supported by Rohacell foam. (b) Array of 4 longitudinally oriented electric dipoles inserted in the waveguide (the arrows indicate the location of the gaps). After [185].

waveguide below the cutoff frequency of the hollow structure can be of the backward as well as of the forward type [185].

Chapter 5

Higher Order Mode Analysis

The homogenized effective description and dispersion diagrams constitute valuable tools that allow one to predict properties of a metamaterial from the analysis of its single unit cell. However, the frequency ranges of stopbands and passbands obtained by eigenmode solver simulations do not always match the spectrum bands characterizing effective parameters retrieved from transmission and reflection coefficients.

For the metamaterial under test based on the SRR/wire structure, the backward wave band obtained by eigenmode solver simulations ($9.9 - 10.1$ GHz) fits in the DNG frequency band extracted by PFDM from the time-domain solver simulations ($9.7 - 10.24$ GHz). In order to explain the discrepancy between both frequency bands (cf. Tab. 4.2), the analysis of higher order modes is conducted[1] [194].

5.1 Port Modes vs Eigenmodes

Within the scope of the effective medium approach (Sec. 3.2), the MTM unit cell is treated as a two-port structure with incoming and outgoing waves, the amplitudes of which are related to each other by the scattering matrix. The unit cell is excited by a broadband pulse in the time domain, and the $\boldsymbol{S}$-matrix is calculated from recorded reflected and transmitted wave amplitudes. The exchange of the energy between the structure and the outside space takes place through the port modes characterizing quasi-infinite waveguides virtually connected to the ports of the simulated structure (waveguide port boundary condition, cf. Sec. 2.2). The fundamental mode of the ports is a TEM wave, equivalent to a plane wave illuminating the structure, whereas the higher order port modes correspond to TE and TM solutions in the waveguides. Within the effective medium approach the higher order modes at the port planes are systematically neglected and single-mode-based scattering parameters are used for the extraction of ε_{eff} and μ_{eff}.

On the other hand, within the scope of the PBE approach (Sec. 4.2), the periodicity of the MTM is directly modeled through a periodic boundary condition. The eigenmode-solver-based approach works in the frequency domain, relating two opposite faces of the unit cell by a fixed phase angle. In combination with the unit-cell size this defines the wavenumber of a macroscopic wave in the DNG macrostructure. The eigenvalues of the resulting system matrix specify the frequencies at which such a wave can propagate. A

---

[1] The higher order mode analysis presented in this chapter is the result of a joint work between the author and Dipl.-Ing. Bastian Bandlow, in cooperation with Prof. Dr.-Ing. Rolf Schuhmann, Fachgebiet Theoretische Elektrotechnik at Universität Paderborn.

dispersion diagram is obtained by solving the system matrix for different phase shifts. As the 3D full wave field solution represents a steady state for a specific frequency, the field distribution at the port planes may contain a lot of superposed port modes. Thus, the physical modes in the MTM structure are represented at the port planes by a linear combination of the waveguide port modes.

Although all the higher order port modes may be far below cutoff in the DNG frequency band, they can still contribute to the energy exchange between the unit cells of the array in cases where the lattice constant a is small enough. To find out how many port modes have to be considered for an accurate scattering matrix representation, the periodic case is first constructed by enforcing the Bloch condition:

$$b_1(\omega) = a_2(\omega)e^{-j\varphi(\omega)}, \qquad b_2(\omega) = a_1(\omega)e^{j\varphi(\omega)}, \tag{5.1}$$

where a_i (b_i) represents an incident (reflected) wave at the ith port. This approach is then extended by consideration of the $(n-1)$ higher order port modes. For n waveguide modes at the ports the vectors $\mathbf{a}_i(\omega)$ and $\mathbf{b}_i(\omega)$ contain the n wave amplitudes for each of these modes at port i and are related by a multimode block scattering matrix:

$$\begin{pmatrix} \mathbf{b}_1(\omega) \\ \mathbf{b}_2(\omega) \end{pmatrix} = \begin{pmatrix} \mathbf{S}_{11}(\omega) & \mathbf{S}_{12}(\omega) \\ \mathbf{S}_{21}(\omega) & \mathbf{S}_{22}(\omega) \end{pmatrix} \cdot \begin{pmatrix} \mathbf{a}_1(\omega) \\ \mathbf{a}_2(\omega) \end{pmatrix}. \tag{5.2}$$

In order to solve for the unknown phase angle φ at a given radial frequency ω, the multimode scattering parameters are converted into the transfer parameters according to the well-known relation:

$$\begin{pmatrix} \mathbf{T}_{11} & \mathbf{T}_{12} \\ \mathbf{T}_{21} & \mathbf{T}_{22} \end{pmatrix} = \begin{pmatrix} \mathbf{S}_{21} - \mathbf{S}_{22}\mathbf{S}_{12}^{-1}\mathbf{S}_{11} & \mathbf{S}_{22}\mathbf{S}_{12}^{-1} \\ -\mathbf{S}_{12}^{-1}\mathbf{S}_{11} & \mathbf{S}_{12}^{-1} \end{pmatrix}, \tag{5.3}$$

where both $\boldsymbol{S}$ and $\boldsymbol{T}$ are block matrices. The obtained transfer matrix gives the quantities at port 1 in terms of the quantities at port 2:

$$\begin{pmatrix} \mathbf{b}_1(\omega) \\ \mathbf{a}_1(\omega) \end{pmatrix} = \begin{pmatrix} \mathbf{T}_{11}(\omega) & \mathbf{T}_{12}(\omega) \\ \mathbf{T}_{21}(\omega) & \mathbf{T}_{22}(\omega) \end{pmatrix} \cdot \begin{pmatrix} \mathbf{a}_2(\omega) \\ \mathbf{b}_2(\omega) \end{pmatrix}. \tag{5.4}$$

Applying the Bloch condition (5.1) to (5.4) and solving:

$$\mathbf{T}\mathbf{v} = \gamma\mathbf{v} \tag{5.5}$$

for eigenpairs $(\mathbf{v}_m, \gamma_m)$ of the matrix $\boldsymbol{T}$ at particular frequencies in the spectrum of interest, the eigenvalues (γ_m) and eigenvectors:

$$\mathbf{v}_m = (\cdots a_{2i} \cdots, \cdots b_{2i} \cdots)^T \tag{5.6}$$

are obtained. For the lossless structure, the propagating eigenstates are identified according to the condition $|\gamma_m| = 1$, whereas the cases $|\gamma_m| \neq 1$ represent evanescent eigenstates [178]. The relation between a specific eigenvalue and the phase is given by $\varphi(\omega) = \angle(\gamma_m)$. Linking the wavenumber with the obtained phase value $[k(\omega) = \varphi(\omega)/a]$, this leads to the dispersion diagram computed by multimode scattering matrix approach (SMA).

The presented approach is applied to the analysed DNG unit cell from Fig. 3.5c. Through numerical simulation with the time-domain solver, a multimode scattering matrix with $n = 25$ port modes is obtained. The matrix contains reflection (r_{ij}) and transmission

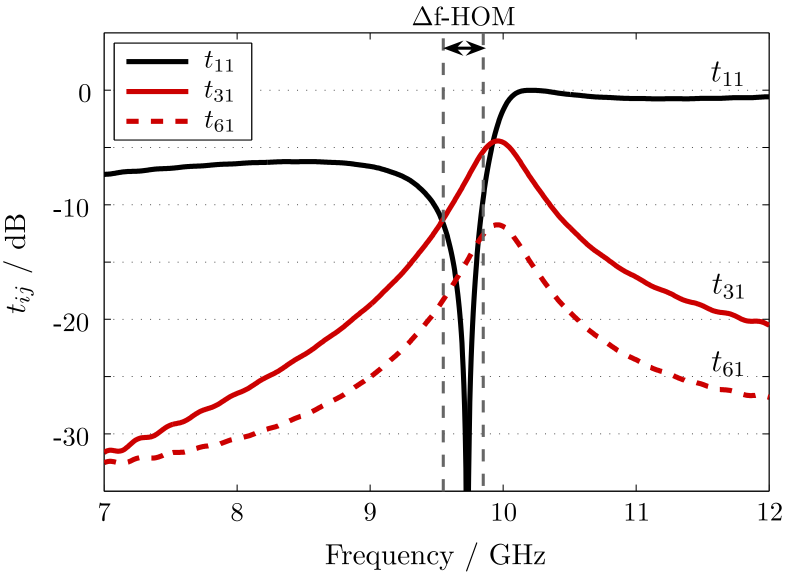

Figure 5.1: Simulated magnitude of the multimode transmission coefficients, the dashed vertical lines limit the frequency range of significant higher order modes transmission (Δf-HOM, 9.55 – 9.85 GHz).

(t_{ij}) coefficients for the ith mode with jth mode incident ($i, j = 1, 2, \ldots, n$). The magnitude of several components of this $\boldsymbol{S}$-matrix is shown in Fig. 5.1. A strong contribution of the higher order port modes in the frequency range close to the extracted DNG band can be noticed. At some frequencies in the range 9.55 – 9.85 GHz (Δf-HOM) the transmission from the first into the third and sixth port mode is higher than transmission into the first mode. From the observation of the corresponding field patterns (Fig. 5.2), the common property of all these modes is the dominant role of E_y and H_x field components. On the other hand, the field distributions corresponding to eigenmodes of the periodic lattice are shown in Fig. 5.3. It can be noticed that a simple plane wave description of the fields in the aperture is merely an approximation, as the field pattern is contaminated by higher order modes. The higher order modes are excited by inhomogeneities and discontinuities in the MTM structure, e.g. sharp corners and edges near the interface planes. The field distribution at the port planes indicates that a significant higher order modes interaction takes place between adjacent unit cells of this MTM.

From the scattering parameters, a 50-by-50 $\boldsymbol{T}$-matrix is constructed at frequencies of interest in the analysed range, according to (5.3). At each frequency point, its eigenvalues and eigenvectors are obtained. From the identified propagating eigenstates, the dispersion diagram based on $n = 25$ port modes is constructed. The same procedure is repeated taking into account only the fundamental TEM mode ($n = 1$). The corresponding single-mode dispersion curve is compared with the multimode solution and related to the reference values obtained by eigenmode solver simulations in Fig. 5.4a. It can be noticed from the figure that including 24 higher order port modes significantly improves the approximation of the dispersion curve. This clarifies the difference between the frequency bands of single/double negative constitutive parameters and the solution of the PBE problem (Tab. 4.2). The result of higher order modes interaction is to modify the

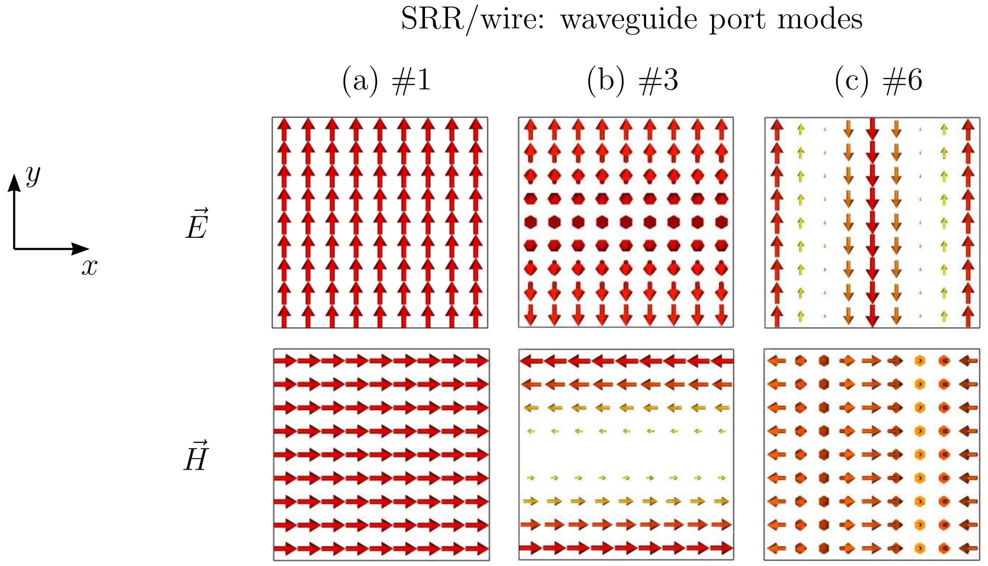

Figure 5.2: (top) Electric and (bottom) magnetic field patterns of the selected waveguide port modes characterizing SRR/wire MTM unit cell from Fig. 3.5c [195]. (a) Fundamental TEM. (b) Third mode. (c) Sixth mode.

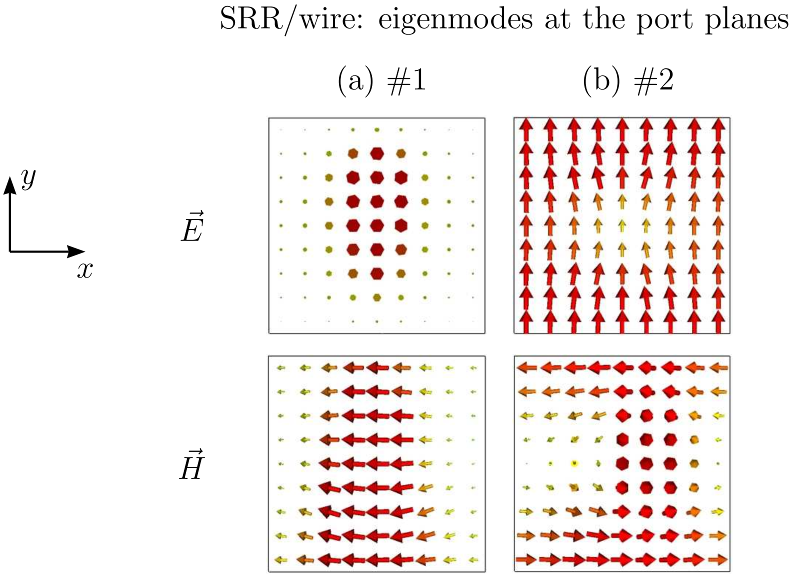

Figure 5.3: (top) Electric and (bottom) magnetic field patterns of the eigenmodes characterizing SRR/wire MTM unit cell from Fig. 3.5c at the port planes [195]. (a) First eigenmode (10.1 GHz). (b) Second eigenmode (11.6 GHz). The field distributions correspond to the center of the Brillouin zone (Γ point).

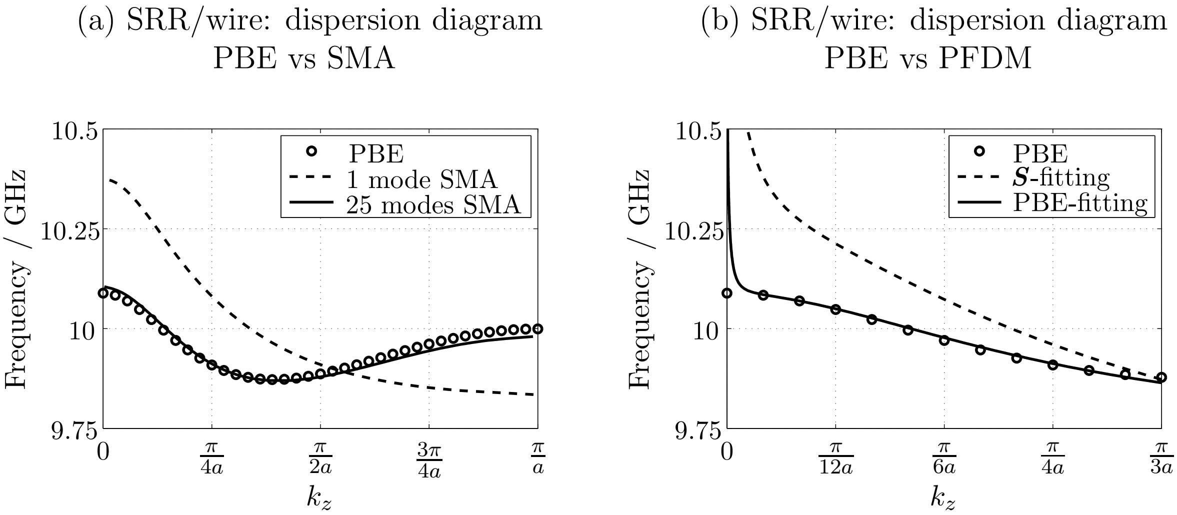

Figure 5.4: (a) Dispersion curve of the first eigenmode for the array of SRR/wires obtained by PBE (o markers), single-mode-based SMA (dashed line) and 25-modes-based SMA (solid line). (b) Dispersion curve of the first eigenmode obtained by PBE (o markers), from ε_{eff} and μ_{eff} models fitted to the scattering parameters (dashed line) and from ε_{eff} and μ_{eff} models fitted to the PBE solution (solid line). After [195].

phase constant from the value computed on the basis of the dominant mode only.

The results of the multimode scattering matrix approach indicate that the higher order port modes can have a significant influence on the transmission process in metamaterials at certain frequencies. The PFDM approach applied to the extraction of effective parameters, however, takes into account only single-mode-based scattering parameters. This single-mode-based effective description approximates the actual electromagnetic behavior of the MTM. Hence the question arises whether it is necessary to account for the higher order port modes in the formulation of the effective MTM description.

5.2 Effective Description Based on Eigensolutions

The predefined Drude and Lorentz models fitted with PFDM to the single-mode scattering parameters can be re-optimized to fit the dispersion diagram obtained by the PBE approach. In this case, the dispersion curve of the first eigenmode replaces the $\boldsymbol{S}$-matrix reference solution used in the standard PFDM algorithm. Assuming the propagation of a TEM wave inside the parallel plate waveguide filled with the effective medium, the corresponding phase constant k_z can be expressed as the real part of the product $\frac{\omega}{c_0} \cdot \sqrt{\varepsilon_{\text{eff}} \cdot \mu_{\text{eff}}}$, where c_0 is the velocity of light in free space and ε_{eff} and μ_{eff} are the predefined dispersive models. By tuning the subparameters of the Drude and Lorentz models by PFDM, the dispersive curve $k_z(\omega)$ is fitted to the PBE solution - the numerical procedure is analogous to the fitting to the reflection and transmission coefficients and the initial solution is based on the models from Tab. 3.2. The corresponding dispersion curves are compared in Fig. 5.4b, whereas the re-optimized models are summarized in Tab. 5.1.

From the re-optimized model coefficients it can be seen that the Drude model describing effective electric permittivity is the same as in the case of fitting to the scattering matrix [hence the $\varepsilon(f)$ figure is not repeated here], whereas the Lorentz model of $\mu(f)$ is slightly

Table 5.1: Predefined effective description of SRR/wire structure optimized with PFDM to fit the reference data: single-mode scattering parameters ($\boldsymbol{S}$-fitting) or first eigenmode dispersion curve (PBE-fitting).

Model		SRR/wire	
type	parameter	$\boldsymbol{S}$-fitting	PBE-fitting
Lorentz	μ_s	1.26	1.14
	μ_∞	1.12	1.06
	f_0 / GHz	9.67	9.73
	δ / MHz	1240	110
Drude	ε_∞	1.62	1.62
	f_p / GHz	14.63	14.63
	ν_c / MHz	30.7	30.7

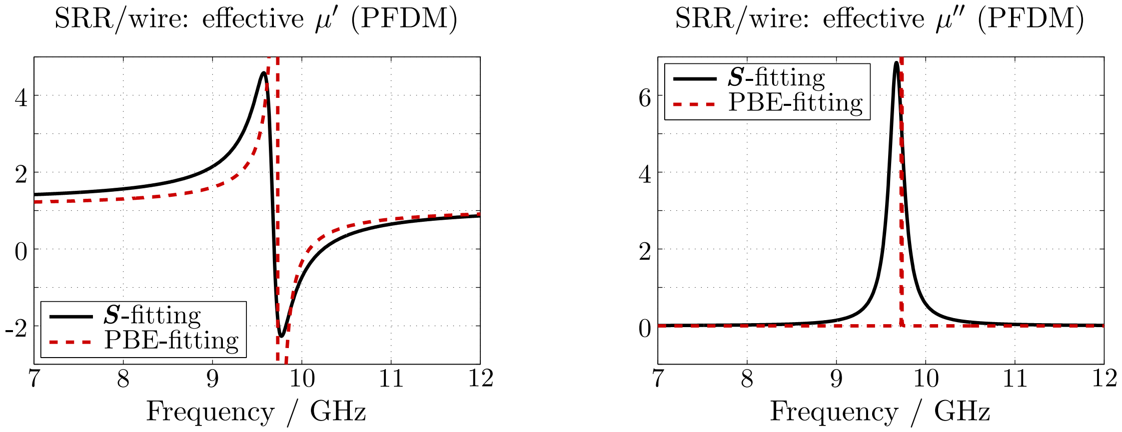

Figure 5.5: Effective magnetic permeability of SRR/wire fitted with PFDM to scattering parameters (solid line) or dispersion diagram (dashed line).

modified as shown in Fig. 5.5. This modification is especially seen in the significantly reduced value of the damping frequency δ (non-zero value of this parameter compensates imperfections of the fitting procedure). The bandwidth of the DNG range is reduced and the imaginary part of the magnetic permeability is compressed to a narrow peak near the resonance. It should be kept in mind that the dispersive curve obtained by the PBE approach describes lossless structure (lossless eigenmode solver used), whereas the PFDM solution based on scattering parameters accounts for the dielectric and conductor losses in the MTM. This partly explains the difference between both effective descriptions - this difference, however, is mostly related to the influence of higher order port modes. To show whether the PBE-fitted effective description introduces a considerable improvement over the $\boldsymbol{S}$-fitted models, both approaches are related to the results of macrostructure simulations in Sec. 6.2.2 (see Fig. 6.6 and the corresponding comments).

Analysis of higher order modes in different MTM geometries reveals that their influence on the transmission process in metamaterials grows with the reduction of the distance between metallic inclusions, i.e. for smaller lattice constants a higher order modes gain on significance [194]. At the same time, small a values are required in MTM designs to fulfill (or at least to approach) the salient long-wavelength requirement $a \ll \lambda_{\mathrm{m}}$, where λ_{m} is the wavelength in the medium. Moreover, a small lattice constant is desired, as due to the large absolute value of the real part of the refractive index near the MTM resonance the wavelength in the medium is strongly shortened and can become comparable with the lattice period. Within the frequency band characterized by $\lambda_{\mathrm{m}} \approx a$ the homogenization of the MTM lattice is not valid [12]. What is more, it is difficult to predict the exact spectrum range in which it happens - one cannot know a priori how large the ratio of the vacuum wavelength to the unit-cell size has to be in order to reach a reasonable effective medium behavior [11].

When λ_{m} becomes comparable to the lattice constant a, some of the evanescent modes have a non-negligible contribution to the transmission phenomena. The presence of the higher order modes is responsible for the anomalous features of the effective parameters retrieved using inversion procedures (Sec. 3.2.1). The frequency region in which the constitutive parameters show non-physical behavior coincides with the one where the evanescent modes predominate. The definition of effective parameters in this frequency region is inconsistent irrespective of the homogenization approach used [196].

These considerations indicate that care is required with the interpretation and application of the effective MTM description. On the one hand, this description is expected to be physically robust and correct in the frequency range of interest, i.e. close to the MTM resonance. On the other hand, the effective parameters are meaningless at the frequency of resonance and in its direct vicinity, but it is difficult to determine a priori the exact spectrum range in which it takes place. The general approach to MTM assumes, that the lattice parameter a should be significantly smaller than the free-space wavelength λ_0, and, what is more important, than the wavelength in the medium λ_{m}. However, shorter a means enhanced influence of evanescent modes and significantly shortened λ_{m} near the resonance. As a consequence, it results in the extended width of the forbidden frequency band where the homogenization of the MTM is not possible.

The multimode scattering matrix approach helps to identify the bandwidth where the homogenization of a MTM structure is not valid due to the significant influence of higher order modes. For the analysed SRR/wire geometry this frequency range equals $9.55 - 9.85$ GHz (Δf-HOM in Fig. 5.1).

Chapter 6

Metamaterial Macrostructures

Metamaterials can be analysed at two levels of abstraction: as microstructures or macrostructures. In the previous chapters (Ch. 3-5), metamaterials are analysed as microstructures, i.e. single unit cells of periodic lattices. In the present chapter the macrostructure approach is shown, based, *inter alia*, on the results obtained from the unit-cell level simulations. Macrostructure approach allows for the observation of various interesting phenomena related to metamaterials and predicted from unit-cell level simulations. Moreover, it can provide validation of the results obtained from the unit-cell level analysis [195, 197].

6.1 Unit-Cell Level Analysis

The unit-cell analysis presented in this work is based on the following three steps:

(a) Extraction of effective constitutive parameters from scattering matrix with the method of parameter fitting of dispersive models.

(b) Analysis of the dispersion diagrams obtained by the solution of a periodic boundary eigenvalue problem.

(c) Higher order modes analysis based on the simulation of a multimode scattering matrix.

The above-mentioned steps provide, respectively:

(a) Effective electric permittivity and magnetic permeability in the frequency range of interest.

(b) Band structure of the periodic lattice with the frequency range and type (forward or backward) of the propagating mode.

(c) Frequency band, where the homogenized model of the MTM lattice is not valid due to the significant contribution of the higher order modes.

The numerical analysis of a single unit cell delivers the necessary information essential for the description of EM properties of the related macrostructure. For the analysed SRR/wire metamaterial the relevant information obtained in the previous sections is summarized schematically in Fig. 6.1.

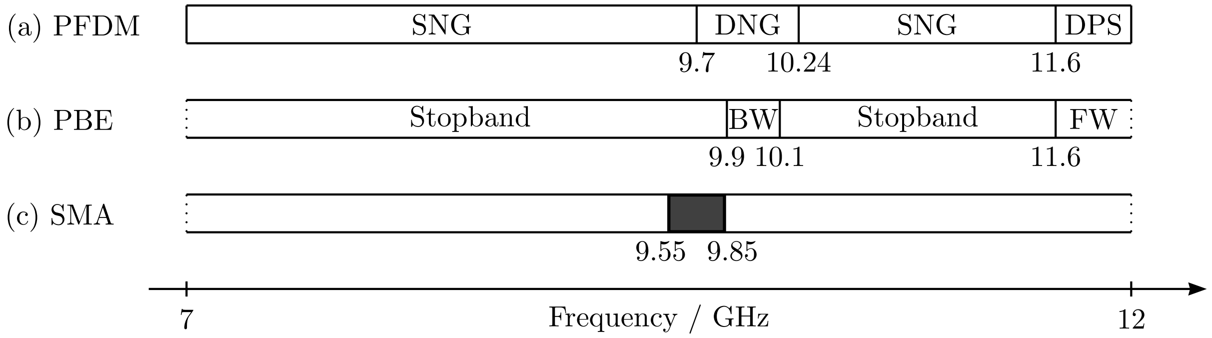

Figure 6.1: SRR/wire: frequency bands obtained from the unit-cell analysis. (a) Single negative, double negative and double positive effective description. (b) Stopbands and passbands: forward/backward wave (FW/BW) from dispersion diagram. (c) Significant interaction of higher order modes. Homogenization is not valid in this range (shaded area).

The real parts of the dispersive constitutive parameters obtained by PFDM and presented in Figs. 3.25-3.26 reveal four frequency regions that can be distinguished (neglecting the imaginary parts of permittivity and permeability is not critical in this case, for a detailed analysis taking into account ε'' and μ'' see e.g. [96]).

The first frequency region $7 - 9.7$ GHz is a stopband in which ε' is negative and μ' is positive (single negative band). Due to the different signs of both constitutive parameters and a significant value of the magnitude of ε', strong attenuation is predicted in this range.

The second frequency region of $9.7 - 10.24$ GHz is a double negative band, where the propagation of a backward wave and negative refraction is expected (the simultaneously negative values of ε' and μ' form a sufficient condition for the opposite direction of the phase velocity and the power flow [96]). However, in a part of this region, strong attenuation is expected, indicated by the high values of μ'' in the vicinity of the resonant frequency of the Lorentz model.

The third frequency band $10.24 - 11.6$ GHz is similar to the first one, i.e. characterized by the negative ε' and positive μ' (single negative band). This configuration of constitutive parameters forms a stopband, whereas the attenuation of the electromagnetic field is expected to be significantly lower than in the first frequency region due to the lower values of ε' and μ' magnitudes.

The fourth frequency band, from 11.6 to 12 GHz (and possibly further, beyond the high-frequency limit of the Drude/Lorentz model description) is characterized by double positive material parameters corresponding to the propagation of a forward wave. At the frequency of 11.6 GHz, the $\varepsilon'(f)$ curve changes its sign (Fig. 3.26), and the MTM structure changes its character from single negative to double positive medium.

These observations are confirmed by the PBE solution, which indicates a backward wave passband between 9.9 and 10.1 GHz and a forward wave passband between 11.6 and 18 GHz, according to the dispersion curve in Fig. 4.7. On the other hand, in the vicinity of the resonant frequency of the μ model, multimode scattering matrix analysis shows enhanced influence of higher order modes ($9.55 - 9.85$ GHz). The homogenized description is not valid in this spectrum range.

The dispersive properties of the MTM under test predicted at the unit-cell level are verified by the simulation of the MTM macrostructure in Sec. 6.2.

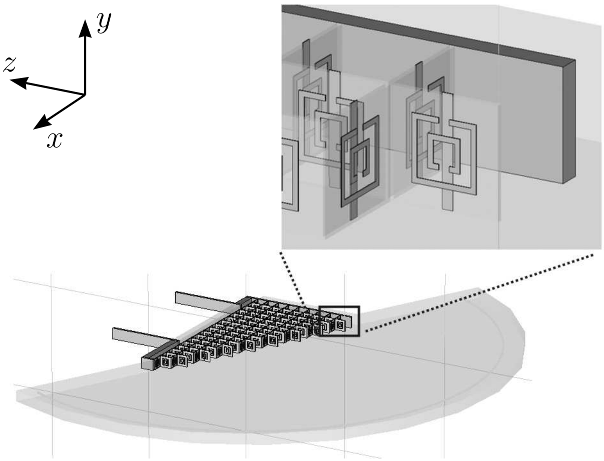

Figure 6.2: Rigorous detailed implementation of the SRR/wire based MTM macrostructure [195].

6.2 Macrostructure Level Analysis

Macrostructure level simulations allow for prediction and visualization of the phenomena characteristic to metamaterials, e.g. the negative refraction reported in [14]. Moreover, the obtained results can verify the proposed modeling approach based on the description of effective MTM properties from the unit-cell level analysis. The macrostructure can be simulated in two forms: as a rigorous detailed lattice or as a homogeneous effective structure.

6.2.1 Rigorous Macrostructure Implementation

In order to obtain a macrostructure reference result, in the first step, the MTM is implemented and simulated as a rigorous representation of the lattice composed from SRRs and wires (Fig. 6.2). The MTM macrostructure composed of 17 unit cells in the x direction and up to 9 unit cells in the z direction is shaped in the form of a wedge which results in 89 MTM cells. The refraction interface is characterized by a staircase pattern with a step ratio 2 : 1, and represents a wedge with 26.6 deg angle. There is one layer of MTM unit cells in the y direction, whereas PEC plates limit the computational model and serve as top and bottom boundary conditions. The wedge is excited by the fundamental mode of a waveguide port (TE_{10}, cutoff frequency 2.8 GHz) located at the left-hand-side boundary of the structure. The additional PEC elements located at the sides of the lattice and guiding the excitation signal from the waveguide port help to properly excite the structure and prevent distortion of the refracted field pattern by the waveguide port signal. Open boundary conditions are applied at the $\pm x$ and $\pm z$ limits of the computational mesh. This configuration is adapted from the reported negative refraction experiment (cf. Fig. 1.9) [14].

The recorded distribution of the electric field at four frequency points in the range of interest is shown in Fig. 6.3a.

According to the predictions from the unit-cell level analysis, there is a very weak transmission at 7 GHz, i.e. in the first frequency band (7 – 9.7 GHz). A strong reflection is observed in this frequency region.

The transmission is highly enhanced at 10 GHz, i.e. in the middle of the second, DNG

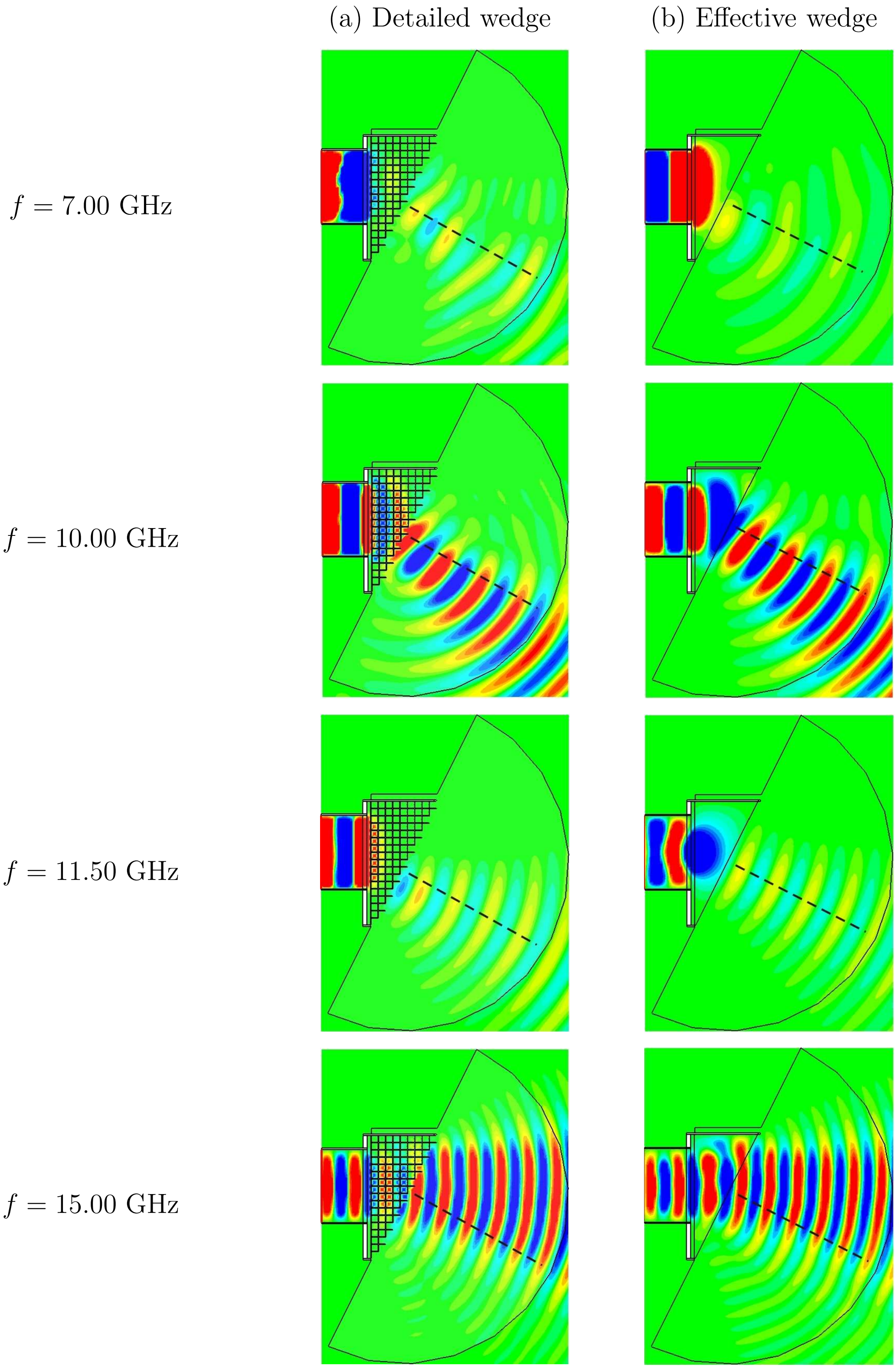
(a) Detailed wedge (b) Effective wedge

Figure 6.3: Distribution of the electric field at four frequencies for (a) detailed and (b) effective wedge structure (dashed line: normal to the boundary between MTM and parallel plate waveguide) [195].

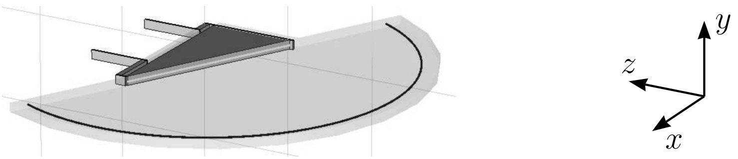

Figure 6.4: Homogeneous effective implementation of the MTM macrostructure (the continuous line indicates the semicircular curve for the sampling of the field distribution and extraction of the refraction angle) [195].

band ($9.7 - 10.24$ GHz). The propagation of a backward wave is observed inside the MTM wedge. From the field distribution, the negative refraction can clearly be noticed.

In the third frequency region ($10.24 - 11.6$ GHz), a weak transmission is observed (significantly stronger, however, than in the first frequency band). Due to the low magnitudes of ε' and μ', the corresponding refractive index is characterized by extremely small values, which results in the transmission nearly parallel to the direction normal to the boundary between the MTM and free space.

The lowest attenuation is observed in the fourth, double positive frequency band ($11.6 - 18$ GHz). From the field distribution at 15 GHz, a positive refraction can clearly be noticed. In this range, the corresponding refractive index of MTM increases from ultra-low values to nearly unity and the propagation of a forward wave is observed inside the wedge.

6.2.2 Effective Macrostructure Implementation

The dispersive effective parameters delivered by PFDM at the unit-cell level constitute the effective representation of the MTM macrostructure. The effective macrostructure is a homogeneous slab shaped in the form of a wedge with the dimensions equivalent to the corresponding detailed implementation (Fig. 6.4). The electric permittivity and magnetic permeability are described by the extracted Drude and Lorentz models, respectively, and assumed to be isotropic. The excitation and boundary conditions used for the numerical simulations are equivalent to those applied for the detailed macrostructure.

The electric field distribution in the effective wedge recorded at the frequency points corresponding to the previous, detailed wedge case, is presented in Fig. 6.3b.

At 7 GHz, in the first frequency band, a strong reflection and very weak transmission is observed. At 10 GHz, in the second, double negative band, a negative refraction can clearly be seen. A backward wave propagates inside the MTM at this frequency. At 11.5 GHz, in the third frequency band, a weak transmission parallel to the direction normal to the boundary between MTM and free space occurs. Due to the small value of the refractive index in the macrostructure, the wavelength in the MTM medium is significantly longer than in the free space. Finally, at 15 GHz, in the fourth, double positive band, the positive refraction can be observed. Note that the effective MTM model is valid for the frequencies between $7 - 12$ GHz. However, due to the absence of additional eigenmodes up to 20 GHz, it still provides good qualitative approximation of the detailed wedge behavior in this frequency region ($11.6 - 18$ GHz).

Comparison of the electric field distribution in the detailed (Fig. 6.2) and effective (Fig. 6.4) MTM macrostructures allows one to observe very good qualitative agreement in the electromagnetic behavior of both structures. The frequency ranges of positive and negative refraction, as well as of high reflection and weak transmission, are equivalently

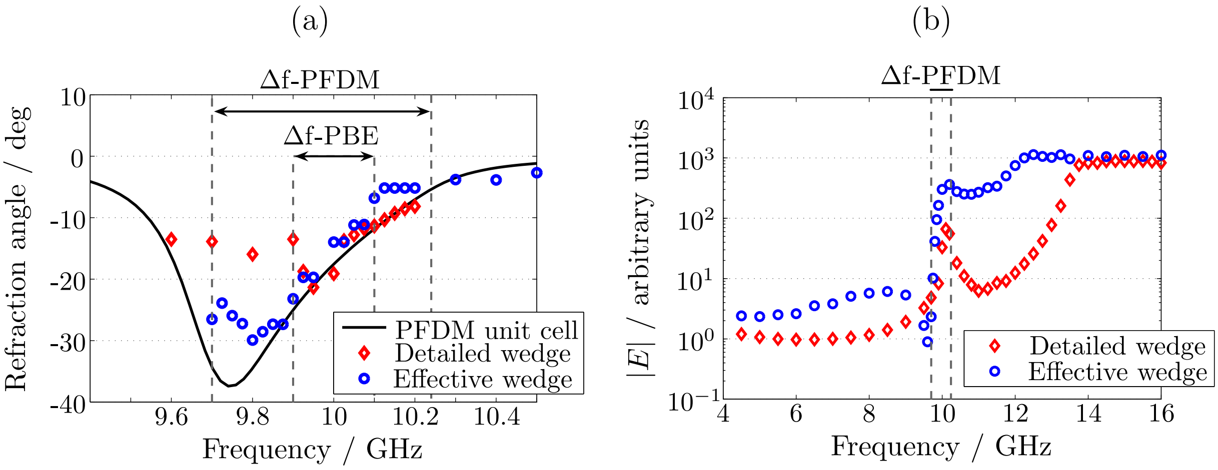

Figure 6.5: (a) Extracted angle of refraction for the detailed (diamonds) and effective (circles) MTM macrostructures. The solid line presents the solution based on PFDM Drude/Lorentz models. The frequency ranges of the first PBE mode (Δf-PBE) and the DNG band based on PFDM (Δf-PFDM) are indicated by the vertical lines. (b) Electric field magnitude sampled along the semicircular curve for the detailed (diamonds) and effective (circles) MTM macrostructures. After [195].

represented. In order to compare both macrostructures in a more quantitative way, the angle of refraction is extracted from the corresponding field distributions. The direction of propagation of the transmitted wave is found from the maximum of the simulated electric field distribution along the semicircular curve of a 12-cm radius (equivalent to $4\lambda_0$ at 10 GHz, see Fig. 6.4), i.e. in the same way as in the referenced negative refraction experiment [14]. An evaluation at a distance of 75 cm ($25\lambda_0$) has been also performed with no significant changes in the field patterns.

In Fig. 6.5a the extracted angle of refraction θ_R in the vicinity of the DNG frequency range is presented for both detailed and effective macrostructure implementations. The unit-cell level results are represented by θ_R obtained from Drude (ε_{eff}) and Lorentz (μ_{eff}) models, according to Snell's law: $n_1 \cdot \sin(\theta_I) = n_2 \cdot \sin(\theta_R)$, where $n_1 = \sqrt{\varepsilon_{\text{eff}}\,\mu_{\text{eff}}}$ is refractive index of the metamaterial structure, $\theta_I = 26.6$ deg is the angle of incidence on the boundary between MTM and free space, whereas refractive index of free space $n_2 = 1$. A very good agreement can be noticed between the results of the detailed and effective macrostructures in the frequency range of the first eigenmode obtained by PBE ($9.9-10.1$ GHz). This is not observed below 9.9 GHz, i.e. in the range close to the magnetic resonance, characterized by the strong influence of higher order modes ($9.55 - 9.85$ GHz) - an indication that the homogenized model is not valid in this band. Moreover, there is a rapid drop of the transmitted electric field in this range (Fig. 6.5b). Below the band edge of the fundamental PBE mode the transmission through the structure and the corresponding field distributions start to behave very irregularly: especially outside of the Δf-PFDM band, this irregularity results in the ambiguity of the refraction angle definition (similar observation is made in [114]).

The corresponding maximal values of the electric field magnitude sampled along the curve are plotted in Fig. 6.5b. The double negative and double positive frequency bands are characterized by enhanced transmission, whereas reduced transmission is observed in single negative bands. These observations agree well with the predictions found from the

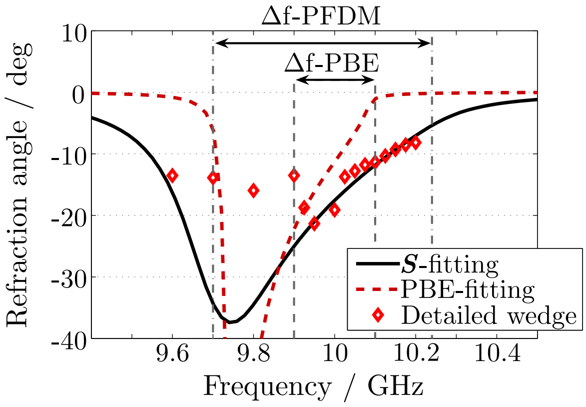

Figure 6.6: Angle of refraction for the Drude and Lorentz models fitted to the single-mode scattering parameters and PBE dispersive curve. The frequency ranges of the first PBE mode (Δf-PBE) and the DNG band based on PFDM (Δf-PFDM) are indicated by the vertical lines [195].

unit-cell analysis.

The angle of refraction based on the Drude and Lorentz models fitted to the single-mode scattering parameters and PBE dispersive curve (Tab. 5.1) is compared in Fig. 6.6. Both characteristics are in reasonable agreement in the Δf-PBE range (comparable observations regarding the effective refractive index extracted from $\boldsymbol{S}$-matrix and dispersive curve for similar MTM geometry are reported in [196]). Relating these results to the angle of refraction observed in the detailed wedge, fitting the dispersive models to the dispersive curve does not lead to any significant improvement in the approximation of the macrostructure behavior. This supports the conclusion, that although the effective description extracted by PFDM from scattering parameters is limited in its accuracy due to the neglection of higher order port modes, it still provides an acceptable approximation of the actual electromagnetic behavior of the MTM under test.

Isotropic Modeling of Anisotropic Structures

The MTM structures are generally anisotropic and their electromagnetic properties depend on the polarization of the applied fields. The extracted Drude and Lorentz models describe the diagonal components of the constitutive parameters tensors corresponding to the orientation of the excitation fields. The effective parameters represent the ε_{yy} and μ_{xx} principal axes components of the electric permittivity and magnetic permeability tensors (E_y and H_x are dominant in the SRR/wire structure). Generally, other tensor elements can take arbitrary (e.g. positive) values, leading to the so-called indefinite medium. However, as long as the incident wave vector points along the principal axis of the MTM (z axis in Figs. 6.2 and 6.4), there is no difference in refractive properties of a macrostructure composed of an isotropic negative index MTM and a medium, for which only ε'_{yy} and μ'_{xx} are less than zero [111], [198]. Consequently, the MTM can be substituted by a homogeneous, isotropic medium with $\varepsilon_{\text{eff}} = \varepsilon_{yy}$ and $\mu_{\text{eff}} = \mu_{xx}$. This also supports the equivalent representation of the 2D MTM lattice by the 1D counterpart in the PBE approach (cf. Fig. 4.6). It should be kept in mind, however, that this equivalence may not hold for all cases, e.g. for waves incident at an angle to an indefinite medium interface cut along principal axes [198].

6.3 Numerical Efficiency

One of the main reasons for the extraction of MTM effective parameters are enormous computational costs inevitably connected with the simulations of electromagnetic properties of large MTM macrostructures. Once extracted, the effective parameters allow for efficient simulation of any macrostructure composed of the described unit cells, providing that additional requirements regarding e.g. field polarization and direction of propagation in the lattice are fulfilled. In the presented numerical experiment, the effective description of the SRR/wire based MTM macrostructure allows for the reduction of computational efforts by approximately two orders of magnitude. The number of mesh nodes for the effective (detailed) wedge with the semicircular space radius $4\lambda_0$ amounts $100 \cdot 10^3$ $(12 \cdot 10^6)$ corresponding to $600 \cdot 10^3$ $(72 \cdot 10^6)$ field unknowns, whereas the CPU costs of the time-domain solver are typically in the range of several minutes (hours) on a modern PC (2× Intel Xeon 3.20 GHz) with 12-GB RAM. On the other hand, the simulation of the macrostructures with the semicircular space radius equal to $25\lambda_0$ requires $3 \cdot 10^6$ $(310 \cdot 10^6)$ mesh nodes corresponding to $18 \cdot 10^6$ $(1.9 \cdot 10^9)$ field unknowns with the CPU costs of 30 minutes (65 hours) on a modern PC (2× Intel Xeon Quadcore 3.00 GHz) with 64-GB RAM. The numerical costs are summarized in Tab. 6.1.

Table 6.1: Numerical costs for the detailed and effective implementations of SRR/wire MTM macrostructure.

Semicircular space radius	Mesh nodes		Memory savings factor	CPU		CPU savings factor
	detailed	homogenized		detailed	homogenized	
	macrostructure			macrostructure		
$4\,\lambda_0$	$12 \cdot 10^6$	$100 \cdot 10^3$	120	2-3 h	1-2 mins.	~ 100
$25\,\lambda_0$	$310 \cdot 10^6$	$3 \cdot 10^6$	103	65 h	30 mins.	130

The time-domain solver used for macrostructure simulations offers an advantage over the frequency-domain solver, as it typically has a superior scalability with respect to the number of mesh cells, both in terms of memory requirements and simulation time. Consequently, the time-domain formulation makes it possible to attack larger numerical problems than the frequency-domain formulation (it should be noted, however, that the applied Cartesian mesh is well suited to the particular problem at hand). Furthermore, all relevant spectral information including distribution of electromagnetic fields at the frequencies of interest is acquired from a single[1] transient run due to the recorded field monitors and discrete Fourier transform.

---

[1] In the case of single-mode-based scattering parameters.

Chapter 7

Summary and Outlook

Summary

This thesis presents an efficient approach to the numerical modeling of metamaterial structures. Numerical simulations of novel phenomena observed in metamaterials pose numerous challenges due to the large size of the multiscale computational problem and the resonant character of the complex, artificially fabricated structures.

In the frame of this work, a set of methods and tools is proposed, that allows one to predict macroscopic effects observed in metamaterial lattices from the analysis of single unit cells. Hence, metamaterials are analysed at two levels: as microstructures (unit cells) and macrostructures (lattices). The simulation approach at the unit-cell level is based on the extraction of effective constitutive parameters from transmission and reflection coefficients, solution of a periodic boundary eigenvalue problem and analysis of higher order modes. On the other hand, macrostructure simulations provide reference and validation to the proposed modeling procedure.

For the metamaterials homogenization the method of parameter fitting of dispersive models is proposed within this work. This approach is related to the popular procedure based on the retrieval of effective electric permittivity and magnetic permeability from the reference scattering parameters of a unit cell. The proposed PFDM approach is based on the predefined dispersive models and avoids the common pitfalls of the $\boldsymbol{S}$-retrieval method that often delivers non-physical results in the frequency range of interest.

As metamaterials occupy a special niche between homogeneous media and photonic crystals, the Bloch analysis and computation of band structures constitute important tools in the modeling of metamaterials. Dispersion diagrams obtained by the solution of a periodic boundary eigenvalue problem reveal the band structure of the analysed lattice, i.e. passbands corresponding to double positive/negative effective parameters and stopbands equivalent to single negative constitutive description. Moreover, a positive or negative slope of the extracted dispersion curves indicates the forward or backward type of the wave propagated in the lattice. Propagation of a backward wave in the periodic structure is a sign of the antiparallel relation between phase and group velocities that is characteristic for double negative materials.

Due to the inherent resonant character, most metamaterial structures are characterized by a significant level of higher order modes near the resonance frequency. The simulation results of a multimode scattering matrix for a metamaterial unit cell allow one to identify the spectral range in which the homogenized metamaterial model is not valid because of a non-negligible contribution of the higher order modes to the transmission process. This frequency band coincides with the one, in which the standard homogenization methods based on $\boldsymbol{S}$-retrieval fail, delivering non-physical values of constitutive parameters.

The simulation results of a negative refraction phenomena observed in the rigorous and homogenized implementations of the metamaterial macrostructure provide the validation of the presented numerical approach. It is shown that all relevant information regarding the phenomena observed at the macrostructure level can be predicted from the unit-cell level analysis. Application of the homogenized model to the macrostructure description allows for the reduction of computational efforts by two orders of magnitude, regarding both CPU and memory costs.

Outlook

There are several limitations in the modeling approach presented in this thesis, including e.g. the requirement for propagation of the EM wave along the principal axis of the metamaterial, isotropic character of the constitutive parameters and non-bianisotropy of the MTM unit cell. Further work on this subject may extend the numerical procedure to account for these aspects.

Some ideas and remarks are listed below:

- The homogenization approach in the present form requires that the wave vector in the metamaterial lattice points along its principal axis. This situation is equivalent to an optimal excitation of the magnetic response of the split ring resonator. The modeling procedure could be extended by allowing the wave vector to form an angle with the principal axis, i.e. for wave propagation in any direction in the metamaterial plane.

- Currently, most efforts regarding numerical analysis of metamaterials concentrate on the improvement of the homogenization methods. However, the salient question "when a particular metamaterial cannot be homogenized" seems to be barely touched in the literature. Therefore, it would be of interest to further explore this topic, especially with relation to bianisotropic metamaterials. In fact, in bianisotropic structures higher order modes can be excited due to magnetoelectric couplings between electric and magnetic quantities. In such cases a significant level of higher order modes does not have to be a sign that homogenization of the medium is not allowed, but could be reflected in additional effective parameters describing cross-polarizability effects in the medium.

- Bloch analysis of metamaterial structures presented in this thesis is performed with a lossless eigenmode solver. Although the neglection of losses in not a critical simplification for the metamaterial structures under test, a solution of periodic boundary eigenvalue problem including lossy effects could deliver valuable information regarding e.g. the complex propagation constant in a periodic lattice. Moreover, it could shed new light on the character of the dispersive curve for the fundamental eigenmode of the SRR/wire unit cell that changes its slope from negative to positive in function of the wavenumber. This topic is not sufficiently explored in the literature and may be related to the existence of complex modes in metamaterial structures.

Appendix A

Constitutive Relations of Bianisotropic Media

The linear, homogeneous, bianisotropic medium responds to electromagnetic excitation according to the following relations [31]:

$$\vec{D} = \overleftrightarrow{\varepsilon} \cdot \vec{E} + \overleftrightarrow{\xi} \cdot \vec{H}, \tag{A.1}$$

$$\vec{B} = \overleftrightarrow{\mu} \cdot \vec{H} + \overleftrightarrow{\zeta} \cdot \vec{E}. \tag{A.2}$$

The material effects are contained in the tensors $\overleftrightarrow{\varepsilon}$, $\overleftrightarrow{\mu}$, $\overleftrightarrow{\xi}$, $\overleftrightarrow{\zeta}$ that due to anisotropy contain up to 36 scalar material parameters. For bi-isotropic medium, the four medium dyadics reduce to four scalar coefficients:

$$\vec{D} = \varepsilon\vec{E} + \xi\vec{H}, \tag{A.3}$$

$$\vec{B} = \mu\vec{H} + \zeta\vec{E}. \tag{A.4}$$

The effects of chirality and non-reciprocity can be distinguished by redefining the magnetoelectric coupling coefficients ξ, ζ:

$$\vec{D} = \varepsilon\vec{E} + (\chi - j\kappa)\sqrt{\mu_0\,\varepsilon_0}\vec{H}, \tag{A.5}$$

$$\vec{B} = \mu\vec{H} + (\chi + j\kappa)\sqrt{\mu_0\,\varepsilon_0}\vec{E}. \tag{A.6}$$

The material parameters used in (A.3)-(A.6) have clear physical meaning: the permittivity ε is a measure for the electric polarization induced by the electric field whereas the permeability μ gives correspondingly the magnetic polarizability of the material. The magnetoelectric parameters ξ, ζ describe the cross-polarizability effects in the medium. The parameter κ contains the degree of chirality[1] and is a measure of the handedness of the material, whereas χ is the degree of inherent non-reciprocity of the medium. Due to the separation of the factor $\sqrt{\mu_0\,\varepsilon_0}$ both κ and χ are dimensionless quantities.

It should be noted that there are several other notational systems for constitutive relations of the material parameters of bi-isotropic media (for an overview, see e.g. [31,199]).

---

[1] Note that the symbol κ that is typically used in the literature to describe chirality, throughout this thesis denotes conductivity.

Appendix B

S-Retrieval Method

A typical configuration for the retrieval of effective constitutive parameters μ_{eff}, ε_{eff} from the measured/calculated scattering matrix is shown in Fig. B.1. The material sample under test is inserted into a segment of a transmission line[1], whose axis is in the x direction. The electric fields at the three sections of the transmission line are denoted as E_A, E_B and E_C, i.e. [200]:

$$\begin{aligned} E_{\text{A}} &= \exp(-jk_0x) + C_1\exp(jk_0x), && \text{(B.1)}\\ E_{\text{B}} &= C_2\exp(-jk_0nx) + C_3\exp(jk_0nx), && \text{(B.2)}\\ E_{\text{C}} &= C_4\exp(-jk_0x). && \text{(B.3)} \end{aligned}$$

where $n = \sqrt{\mu_{\text{eff}}\,\varepsilon_{\text{eff}}}$.

The constants C_i ($i = 1, 2, 3, 4$) are determined from the boundary conditions on the electric field and the magnetic field. The boundary condition on the electric field is the continuity of the tangential component at the interfaces (cf. Fig. B.1):

$$\begin{aligned} E_{\text{A}}\big|_{x=0} &= E_{\text{B}}\big|_{x=0}, && \text{(B.4)}\\ E_{\text{B}}\big|_{x=a} &= E_{\text{C}}\big|_{x=a}. && \text{(B.5)} \end{aligned}$$

The boundary condition on the magnetic field requires the additional assumption that no surface currents are generated, so the tangent component of the magnetic field is continuous across the interface:

$$\begin{aligned} \frac{1}{\mu_0}\frac{\partial E_{\text{A}}}{\partial x}\bigg|_{x=0} &= \frac{1}{\mu_0\mu_{\text{eff}}}\frac{\partial E_{\text{B}}}{\partial x}\bigg|_{x=0}, && \text{(B.6)}\\ \frac{1}{\mu_0\mu_{\text{eff}}}\frac{\partial E_{\text{B}}}{\partial x}\bigg|_{x=a} &= \frac{1}{\mu_0}\frac{\partial E_{\text{C}}}{\partial x}\bigg|_{x=a}. && \text{(B.7)} \end{aligned}$$

The scattering parameters of the two-port network are obtained by solving (B.1)-(B.3) subject to the boundary conditions (B.4)-(B.7) [200]:

$$\begin{aligned} S_{11} &= \frac{(1-T^2)R}{1-R^2T^2}, && \text{(B.8)}\\ S_{21} &= \frac{(1-R^2)T}{1-R^2T^2}, && \text{(B.9)} \end{aligned}$$

---

[1] The method can also be applied in the free-space environment.

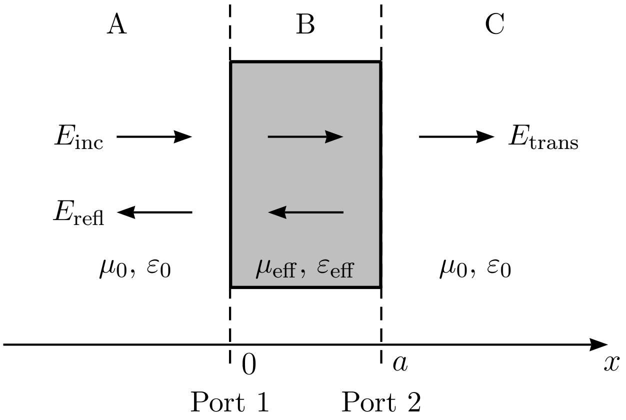

Figure B.1: Electromagnetic waves transmitted through and reflected from a sample under test.

where the transmission T and reflection R are given by:

$$T = \exp(-jk_0 na), \tag{B.10}$$

$$R = \frac{z-1}{z+1}, \tag{B.11}$$

whereas $z = \sqrt{\mu_{\mathrm{eff}}/\varepsilon_{\mathrm{eff}}}$ is the normalized wave impedance and the sample is measured in a TEM transmission line characterized by the impedance $z = 1$.

The transmission and reflection can be related to the measured/calculated scattering parameters according to the Nicolson-Ross-Weir relations [156, 201]:

$$R = \frac{1 + S_{11}^2 - S_{21}^2}{2\, S_{11}} \pm \sqrt{\left(\frac{1 + S_{11}^2 - S_{21}^2}{2\, S_{11}}\right)^2 - 1}, \tag{B.12}$$

$$T = \frac{(S_{11} + S_{21}) - R}{1 - (S_{11} + S_{21})R}. \tag{B.13}$$

where the sign in (B.12) is determined by the requirement $|R| \leq 1$. Alternatively, transmission can be computed directly from scattering parameters [158]:

$$T = \frac{1 - S_{11}^2 + S_{21}^2}{2\, S_{21}} \pm j\sqrt{1 - \left(\frac{1 - S_{11}^2 + S_{21}^2}{2\, S_{21}}\right)^2}, \tag{B.14}$$

leading to the refractive index defined as:

$$n = -\frac{1}{k_0 a}\Big(\big(\Im(\ln T) + 2m\pi\big) - j\Re(\ln T)\Big). \tag{B.15}$$

The parameter $m \in \mathbb{Z}$ (B.15) is related to the branch index of n' (principal value for $m = 0$), whereas the sign in (B.14) is determined by the requirement $n'' \geq 0$ for passive media.

The normalized wave impedance characterizing the sample under test is expressed in terms of scattering parameters as [104, 157]:

$$z = \pm\sqrt{\frac{(1 + S_{11})^2 - S_{21}^2}{(1 - S_{11})^2 - S_{21}^2}}, \tag{B.16}$$

with the sign determined by the requirement $\Re(z) \geq 0$.

The effective electric permittivity and magnetic permeability characterizing the material sample under test are calculated from (B.15) and (B.16) as:

$$\varepsilon_{\text{eff}} = \frac{n}{z}, \tag{B.17}$$

$$\mu_{\text{eff}} = nz. \tag{B.18}$$

The presented approach is limited to symmetric structures, i.e. reciprocal systems characterized by scattering matrix $\boldsymbol{S}=\boldsymbol{S}^T$. As mentioned in Sec. 3.1, in order to avoid the bianisotropic effects metamaterials are typically designed as symmetric structures. For asymmetric MTM unit cells, the standard $\boldsymbol{S}$-retrieval method leads to two generally distinct values for the wave impedance, that are assigned to the structure depending on the direction of wave propagation with respect to the unit cell. Consequently, two distinct values of electric permittivity and magnetic permeability are obtained. In such cases, the standard $\boldsymbol{S}$-retrieval method presented here should be modified, see [9].

Applied Notations and Symbols

General Mathematical Symbols

$\mathbb{Z}$	Integer numbers
$\mathbb{R}$	Real numbers
$\mathbb{I}$	Imaginary numbers
$\mathbb{C}$	Complex numbers
∇	Nabla operator
$\vec{r}$	Spatial vector
$\mathbf{M}$	Matrix
$\mathbf{M}^{-1}$	Inverse matrix
$\mathbf{M}^{T}$	Transpose of matrix $\mathbf{M}$
$d\vec{s}, d\vec{A}, d\vec{V}$	Infinitesimal length, surface, volume elements
$\partial A, \partial V$	Boundary of the area, volume
$\langle\cdot\rangle_L, \langle\cdot\rangle_A, \langle\cdot\rangle_V$	Line/surface/volume averaged quantity

Finite Integration Technique

$G, \widetilde{G}$	Primary grid, dual grid
$L_n, \widetilde{L}_n$	Primary/dual grid edges
$A_n, \widetilde{A}_n$	Primary/dual grid facets
$V_n, \widetilde{V}_n$	Primary/dual grid cell (volume)
$\widehat{\mathrm{e}}, \widehat{\mathbf{e}}$	Element, vector of electric grid voltage
$\widehat{\mathrm{h}}, \widehat{\mathbf{h}}$	Element, vector of magnetic grid voltage
$\widehat{\widehat{\mathrm{d}}}, \widehat{\widehat{\mathbf{d}}}$	Element, vector of electric facet flux
$\widehat{\widehat{\mathrm{b}}}, \widehat{\widehat{\mathbf{b}}}$	Element, vector of magnetic facet flux
$\widehat{\widehat{\mathrm{j}}}, \widehat{\widehat{\mathbf{j}}}$	Element, vector of facet currents
$\widehat{\widehat{\mathrm{j}}}_{\mathrm{l}}, \widehat{\widehat{\mathbf{j}}}_{l}$	Element, vector of facet conduction currents
$\widehat{\widehat{\mathrm{j}}}_{\mathrm{e}}, \widehat{\widehat{\mathbf{j}}}_{e}$	Element, vector of facet externally imposed currents
$\mathrm{q}, \mathbf{q}$	Element, vector of electric grid charges
$\mathbf{C}, \widetilde{\mathbf{C}}$	Discrete curl operator on the primary/dual grid
$\mathbf{S}, \widetilde{\mathbf{S}}$	Discrete divergence operator on the primary/dual grid
$\mathbf{M}_{\varepsilon}$	Material matrix of electric permittivity
$\mathbf{M}_{\mu^{-1}}$	Material matrix of inversed magnetic permeability
$\mathbf{M}_{\kappa}$	Material matrix of conductivity
$\overline{\varepsilon}$	Averaged electric permittivity
$\overline{\mu}$	Averaged magnetic permeability
$\overline{\kappa}$	Averaged conductivity
Δt	Time step

Basic Relations

$$\begin{aligned} \varepsilon &= \varepsilon_0\,\varepsilon_{\text{eff}} &&= \varepsilon_0(\varepsilon' - j\varepsilon'') \\ \mu &= \mu_0\,\mu_{\text{eff}} &&= \mu_0(\mu' - j\mu'') \end{aligned}$$

Continuous Field Theory

$\vec{E}$	Electric field strength
$\vec{D}$	Electric flux density
$\vec{H}$	Magnetic field strength
$\vec{B}$	Magnetic flux density
$\vec{J}$	Electric current density
ρ	Electric charge density
ε	Electric permittivity
ε_0	Electric permittivity of free space
ε_{eff}	Effective electric permittivity (relative to free space)
μ	Magnetic permeability
μ_0	Magnetic permeability of free space
μ_{eff}	Effective magnetic permeability (relative to free space)
ξ, ζ	Magnetoelectric coupling coefficients
κ	Electric conductivity
$\lambda, \lambda_0, \lambda_{\text{m}}$	Wavelength, free-space wavelength, medium wavelength
n	Refractive index
Z, Z_0	Wave impedance, free-space wave impedance
z	Normalized wave impedance
$\vec{k}$	Wave vector
φ	Phase shift
ω	Angular frequency
f	Frequency
f_c	Cutoff frequency of a rectangular waveguide
c_0	Velocity of light in free space
v_g	Group velocity
a_i, b_i	Incident/reflected wave at the ith port
θ_I, θ_R	Angle of incidence/refraction
$\boldsymbol{S}$	Scattering matrix
$\boldsymbol{T}$	Transfer matrix
$\gamma_m, \mathbf{v}_m$	Eigenvalue, eigenvector of a transfer matrix
T, R	Transmission, reflection coefficient
t_{ij}, r_{ij}	Transmission, reflection coefficent for the ith mode with jth mode incident
L	Inductance
C	Capacitance

Dispersive Models

n_e	Density of electrons
m, m_{e}	Electron's mass, effective electron's mass
e	Elementary electron's charge
μ_s	Magnetic permeability at the low-frequency limit of the Lorentz model (relative to free space)
μ_∞	Magnetic permeability at the high-frequency limit of the Lorentz model (relative to free space)
ω_0	Angular resonance frequency of the Lorentz model
δ	Damping frequency of the Lorentz model
ε_∞	Electric permittivity at the high-frequency limit of the Drude model (relative to free space)
ω_p	Angular plasma frequency of the Drude/Lorentz model
ν_c	Collision frequency of the Drude model

Photonic Crystals

a	Lattice constant, unit-cell size
Γ	Center of the Brillouin zone
X, Y	Face of the Brillouin zone
M	Corner of the Brillouin zone

Acronyms

EM	Electromagnetic
PDE	Partial Differential Equations
MGE	Maxwell's Grid Equations
TE/TM/TEM	Transverse Electric/Magnetic/Electromagnetic
1D, 2D, 3D	One-, Two-, Three-dimensional
PEC	Perfect Electric Conductor
PMC	Perfect Magnetic Conductor
PBC	Periodic Boundary Condition
PML	Perfectly Matched Layer
FIT	Finite Integration Technique
FDTD	Finite-Difference Time Domain
CAA	Computer-Aided Analysis
MTM	Metamaterial
SNG	Single Negative
DNG	Double Negative
DPS	Double Positive
SRR	Split Ring Resonator
EC-SRR	Edge-Coupled Split Ring Resonator
BC-SRR	Broadside-Coupled Split Ring Resonator
FAM	Fields Averaging Method
PFDM	Parameter Fitting of Dispersive Models
PBE	Periodic Boundary Eigenvalue problem
SMA	Scattering Matrix Approach
Δf-PFDM	Frequency range of double negative material parameters obtained by PFDM
Δf-PBE	Frequency range of a fundamental eigenmode obtained from PBE
Δf-HOM	Frequency range of significant higher order mode transmission obtained from multimode SMA

Bibliography

[1] J.D. Jackson. *,,Classical electrodynamics"*. Wiley, 3rd edition, 1999.

[2] G.W. Milton. *,,The theory of composites"*. Cambridge University Press, 2004.

[3] K.D. Cherednichenko, V.P. Smyshlyaev, and V.V. Zhikov. ,,Non-local homogenized limits for composite media with highly anisotropic periodic fibres". *Proceedings of the Royal Society of Edinburgh*, 136A:87–114, 2006.

[4] A. Bensoussan, J.L. Lions, and G. Papanicolaou. *,,Asymptotic analysis for periodic structures"*, volume 5 of *Studies in Mathematics and its Applications*. North-Holland Publishing, Amsterdam, 1978.

[5] A. Sihvola. *,,Electromagnetic mixing formulas and applications"*. The Institution of Electrical Engineers, 1999.

[6] J.M. Lourtioz, H. Benisty, V. Berger, J.M. Gerard, D. Maystre, and A. Tschelnokov. *,,Photonic crystals: towards nanoscale photonic devices"*. Springer, 2005.

[7] M. Notomi. ,,Theory of light propagation in strongly modulated photonic crystals: refractionlike behavior in the vicinity of the photonic band gap". *Physical Review B*, 62(16):10696–10705, 15 Oct 2000.

[8] M. Lapine and S. Tretyakov. ,,Contemporary notes on metamaterials". *IET Microwaves, Antennas and Propagation*, 1(1):3–11, Feb 2007.

[9] D.R. Smith, D.C. Vier, T. Koschny, and C.M. Soukoulis. ,,Electromagnetic parameter retrieval from inhomogeneous metamaterials". *Physical Review E*, 71:036617(1–11), 22 Mar 2005.

[10] C. Caloz, A. Lai, and T. Itoh. ,,The challenge of homogenization in metamaterials". *New Journal of Physics*, 7(167):1–15, 8 Aug 2005.

[11] T. Koschny, P. Markos, E.N. Economou, D.R. Smith, D.C. Vier, and C.M. Soukoulis. ,,Impact of inherent periodic structure on effective medium description of left-handed and related metamaterials". *Physical Review B*, 71(24):245105(1–22), 8 Jun 2005.

[12] C.R. Simovski and S.A. Tretyakov. ,,Local constitutive parameters of metamaterials from an effective-medium perspective". *Physical Review B*, 75(19):195111(1–10), 14 May 2007.

[13] R. Marques, F. Medina, and R. Rafii-El-Idrissi. ,,Role of bianisotropy in negative permeability and left-handed metamaterials". *Physical Review B*, 65:144440(1–5), 4 Apr 2002.

[14] R.A. Shelby, D.R. Smith, and S. Schultz. ,,Experimental verification of a negative index of refraction". *Science*, 292:77–79, 6 Apr 2001.

[15] Lord Rayleigh. ,,The influence of obstacles arranged in rectangular order upon the properties of a medium". *Philosophical Magazine*, 34(5):481–502, 1892.

[16] J.C. Bose. ,,On the rotation of plane of polarisation of electric waves by a twisted structure". *Proceedings of the Royal Society of London*, 63:146–152, 1898.

[17] I.V. Lindell, A.H. Sihvola, and J. Kurkijarvi. ,,Karl F. Lindman: the last Hertzian, and a harbinger of electromagnetic chirality". *IEEE Antennas and Propagation Magazine*, 34(3):24–30, Jun 1992.

[18] W.E. Kock. ,,Metal-lens antennas". *Proceedings of the I.R.E.*, 34(11):828–836, Nov 1946.

[19] R.E. Collin and F.J. Zucker, editors. *,,Antenna theory, Part 2"*, chapter 18: ,,*Lens antennas*", by J. Brown, pages 104–150. Inter-University Electronics Series, Vol. 7. McGraw-Hill, New York, 1969.

[20] R.E. Collin. *,,Field theory of guided waves"*, chapter 12: ,,*Artificial dielectrics*", pages 749–786. The IEEE Press Series on Electromagnetic Wave Theory. IEEE Press, New York, 2nd edition, 1991.

[21] W.E. Kock. ,,Metallic delay lenses". *Bell System Technical Journal*, 17:58–82, Jan 1948.

[22] S.A. Schelkunoff and H.T. Friis. *,,Antennas, theory and practice"*, chapter 19: ,,*Lenses*", pages 573–591. Applied Mathematics Series. John Wiley and Sons, New York, 1952.

[23] J. Brown. *,,Microwave lenses"*. Methuen's Monographs on Physical Subjects. John Wiley and Sons, London, 1953.

[24] H. Jasik, editor. *,,Antenna engineering handbook"*, chapter 14: ,,*Lens-type radiators*", by S.B. Cohn, pages 14(1–43). McGraw-Hill, New York, 1961.

[25] J. Brown. ,,Artificial dielectrics". *Progress in Dielectrics*, 2:195–225, 1960.

[26] C.J.F. Bottcher. *,,Theory of electric polarisation"*, page 199. Elsevier, Amsterdam, 1952.

[27] W. Rotman. ,,Plasma simulation by artificial dielectrics and parallel-plate media". *IEEE Transactions on Antennas and Propagation*, 10(1):82–95, Jan 1962.

[28] I.J. Bahl and K.C. Gupta. ,,A leaky-wave antenna using an artificial dielectric medium". *IEEE Transactions on Antennas and Propagation*, 22(1):119–122, Jan 1974.

[29] R.J. King, D.V. Thiel, and K.S. Park. ,,The synthesis of surface reactance using an artificial dielectric". *IEEE Transactions on Antennas and Propagation*, 31(3):471–476, May 1983.

[30] A. Lakhtakia and V.K. Varadan. *,,Time-harmonic electromagnetic fields in chiral media (lecture notes in physics)".* Springer Verlag, New York, 1989.

[31] I.V. Lindell, A.H. Sihvola, S.A. Tretyakov, and A.J. Viitanen. *,,Electromagnetic waves in chiral and bi-isotropic media".* Artech House, 1994.

[32] O.N. Singh and A. Lakhtakia, editors. *,,Electromagnetic fields in unconventional materials and structures".* Wiley Series in Microwave and Optical Engineering. John Wiley and Sons, New York, 2000.

[33] N. Engheta. ,,Special Issue on Wave Interaction with Chiral and Complex Media". *Journal of Electromagnetic Waves and Applications, JEWA*, 6(5-6):533–793, 1992.

[34] A. Priou. ,,Special Issue on Bianisotropic and Bi-isotropic Media and Applications". *Progress In Electromagnetics Research, PIER*, 9:1–397, 1994.

[35] W.S. Weiglhofer, A.M. Barbosa, and A.L. Topa. ,,Special Issue on Bianisotropics 2000". *AEÜ International Journal of Electronics and Communications*, 55(4):209–291, 2001.

[36] S. Zouhdi, A. Sihvola, and M. Arsalane, editors. *,,Proceedings of 9th International Conference on Electromagnetics of Complex Media (NATO Advanced Workshop on Bianisotropics 2002)"*, volume 89 of *NATO Science Series, II. Mathematics, Physics and Chemistry*, Marrakesh, Morocco, 8-11 May 2002. Kluwer Academic Publishers.

[37] L.D. Barron. *,,Molecular light scattering and optical activity"*, page 25. Cambridge University Press, 2nd edition, 2004.

[38] D.K. Cheng and J.A. Kong. ,,Covariant descriptions of bianisotropic media". *Proceedings of the IEEE*, 56(3):248–251, Mar 1968.

[39] J.A. Kong. *,,Theory of electromagnetic waves".* John Wiley and Sons, New York, 1975.

[40] A. Lakhtakia. *,,Encyclopedia of RF and microwave engineering"*, chapter ,,*Chirality*", pages 610–622. John Wiley and Sons, 2005.

[41] V.K. Varadan and V.V. Varadan. ,,Electromagnetic shielding and absorptive materials". *U.S. Patent*, No. 4948922, Mar 1990.

[42] C.R. Brewitt-Taylor. ,,Modeling of helix-loaded chiral radar-absorbing layers". *Progress In Electromagnetics Research, PIER*, 9:289–310, 1994.

[43] O. Reynet and O. Acher. ,,Theoretical and experimental limitations of chiral microwave absorbers". In S. Zouhdi, A. Sihvola, and M. Arsalane, editors, *,,Advances in electromagnetics of complex media and metamaterials"*, volume 89 of *NATO Science Series, II. Mathematics, Physics and Chemistry*, pages 461–470, Amsterdam, 2002. Kluwer Academic Publishers.

[44] J.H. Cloete, M. Bingle, and D.B. Davidson. ,,The role of chirality and resonance in synthetic microwave absorbers". *AEÜ International Journal of Electronics and Communications*, 55(4):233–239, 2001.

[45] P. Pelet and N. Engheta. ,,The theory of chirowaveguides". *IEEE Transactions on Antennas and Propagation*, 38(1):90–98, Jan 1990.

[46] F. Mariotte, P. Pelet, and N. Engheta. ,,A review of recent study of guided waves in chiral media". *Progress In Electromagnetics Research, PIER*, 9:311–350, 1994.

[47] P. Pelet and N. Engheta. ,,Theoretical study of radiation properties of a finite-length thin-wire chirostrip antenna using dyadic Green's functions and method of moments". *Progress In Electromagnetics Research, PIER*, 9:265–288, 1994.

[48] A. Lakhtakia and R. Messier. *,,Introduction to complex mediums for optics and electromagnetics"*, chapter *,,The past, the present, and the future of sculptured thin films"*, pages 447–478. SPIE Press, Bellingham, USA, 2003.

[49] M.W. McCall. *,,Introduction to complex mediums for optics and electromagnetics"*, chapter *,,Towards optoelectronic applications of chiral sculptured thin films"*, pages 479–506. SPIE Press, Bellingham, USA, 2003.

[50] E. Yablonovitch. ,,Inhibited spontaneous emission in solid-state physics and electronics". *Physical Review Letters*, 58(20):2059–2062, 18 May 1987.

[51] S. John. ,,Strong localization of photons in certain disordered dielectric superlattices". *Physical Review Letters*, 58(23):2486–2489, 8 Jun 1987.

[52] J.D. Joannopoulos, R.D. Meade, and J.N. Winn. *,,Photonic crystals: molding the flow of light"*. Princeton University Press, 1995.

[53] K. Sakoda. *,,Optical properties of photonic crystals"*. Springer, 2001.

[54] S.G. Johnson and J.D. Joannopoulos. *,,Photonic crystals: the road from theory to practice"*. Kluwer Academic Publishers, Boston, 2002.

[55] K. Busch, S. Lolkes, R.B. Wehrspohn, and H. Foll, editors. *,,Photonic crystals: advances in design, fabrication, and characterization"*. Wiley-VCH Verlag, 2004.

[56] F. Zolla, G. Renversez, A. Nicolet, B. Kuhlmey, S. Guenneau, and D. Felbacq. *,,Foundations of photonic crystal fibers"*. Imperial College Press, 2005.

[57] K. Yasumoto, editor. *,,Electromagnetic theory and applications for photonic crystals"*. CRC Press, Taylor and Francis Group, 2006.

[58] J.D. Joannopoulos, S.G. Johnson, J.N. Winn, and R.D. Meade. *,,Photonic crystals: molding the flow of light"*. Princeton University Press, 2nd edition, 2008.

[59] A. Martinez, A. Griol, P. Sanchis, and J. Marti. *,,Encyclopedia of RF and microwave engineering"*, chapter *,,Photonic band gap (PBG)"*, pages 3823–3838. John Wiley and Sons, 2005.

[60] J.D. Joannopoulos, P.R. Villeneuve, and S. Fan. ,,Photonic crystals: putting a new twist of light". *Nature*, 386:143–149, 13 Mar 1997.

[61] J.B. Pendry, A.J. Holden, D.J. Robbins, and W.J. Stewart. ,,Magnetism from conductors and enhanced nonlinear phenomena". *IEEE Transactions on Microwave Theory and Techniques*, 47(11):2075–2084, Nov 1999.

[62] J.B. Pendry, A.J. Holden, D.J. Robbins, and W.J. Stewart. ,,Low frequency plasmons in thin-wire structures". *Journal of Physics: Condensed Matter*, 10:4785–4809, 1998.

[63] D.R. Smith, W.J. Padilla, D.C. Vier, S.C. Nemat-Nasser, and S. Schultz. ,,Composite medium with simultaneously negative permeability and permittivity". *Physical Review Letters*, 84(18):4184–4187, 1 May 2000.

[64] V.G. Veselago. ,,The electrodynamics of substances with simultaneously negative values of permittivity and permeability". *Soviet Physics USPEKHI*, 10(4):509–514, Jan/Feb 1968.

[65] S.A. Tretyakov. *,,Analytical modeling in applied electromagnetics"*. Artech House, Boston, 2003.

[66] G.V. Eleftheriades and K.G. Balmain, editors. *,,Negative-refraction metamaterials, fundamental principles and applications"*. IEEE Press, 2005.

[67] C. Caloz and T. Itoh. *,,Electromagnetic metamaterials: transmission line theory and microwave applications"*. John Wiley and Sons, 2006.

[68] N. Engheta and R.W. Ziolkowski, editors. *,,Metamaterials, physics and engineering explorations"*. IEEE Press, 2006.

[69] R. Marques, F. Martin, and M. Sorolla. *,,Metamaterials with negative parameters, theory, design, and microwave applications"*. John Wiley and Sons, 2007.

[70] A.K. Sarychev and V.M. Shalaev. *,,Electrodynamics of metamaterials"*. World Scientific Publishing, 2007.

[71] J. Pendry. ,,Focus Issue: Negative Refraction and Metamaterials". *Optics Express*, 11(7):639–760, Apr 2003.

[72] R.W. Ziolkowski and N. Engheta. ,,Metamaterials: Special Issue". *IEEE Transactions on Antennas and Propagation*, 51(10):2546–2750, Oct 2003.

[73] N. Zheludev and V. Shalaev. ,,Special Issue on Nanostructured Optical Metamaterials: Beyond Photonic Bandgap Effects". *Journal of Optics A: Pure and Applied Optics*, 7(2):1–254, Feb 2005.

[74] T. Itoh and A.A. Oliner. ,,Special Issue on Metamaterials". *IEEE Transactions on Microwave Theory and Techniques*, 53(4):1418–1556, Apr 2005.

[75] A. Lakhtakia. ,,Focus on Negative Refraction". *New Journal of Physics*, 7, Aug 2005.

[76] T.M. Grzegorczyk. ,,Special Issue on Metamaterials Exhibiting Left-Handed Properties and Negative Refraction". *Progress In Electromagnetics Research*, 51:1–340, 2005.

[77] S. He. ,,Special Issue on the International Workshop on Metamaterials and Negative Refraction, 27-29 August 2005, Hangzhou, China". *Journal of Zhejiang University Science A*, 7(1):1–108, Jan 2006.

[78] C. Caloz. ,,Special Issue on Numerical Modelling of Metamaterial Properties, Structures and Devices". *International Journal of Numerical Modelling*, 19(2):83–228, Mar 2006.

[79] F. Martin. ,,Special Issue on Metamaterials". *Journal of the European Microwave Association*, 2(1):1–109, Mar 2006.

[80] V.M. Shalaev and A. Boardman. ,,Focus Issue on Metamaterials". *Journal of the Optical Society of America B*, 23(3):386–583, Mar 2006.

[81] I.B. Vendik, N.P. Johnson, and T. Szoplik. ,,Special Issue on Metamaterials". *Opto-Electronics Review*, 14(3):167–262, Sept 2006.

[82] F. Martin and A. Toscano. ,,Special Issue on Metamaterials and Special Materials for Electromagnetic Applications and Telecommunications". *Microwave and Optical Technology Letters*, 48(12):2481–2638, Dec 2006.

[83] K. Sato. ,,Special Issue: Metamaterials and Automotive Applications". *Technical Journal, R and D Review of Toyota*, 41(4):1–31, 2006.

[84] A. Sihvola. ,,Special Issue on Complex Media and Metamaterials". *Electromagnetics*, 26(3):189–314, 2006.

[85] G. Eleftheriades and Y. Vardaxoglou. ,,Special Issue: Metamaterials". *IET Microwaves, Antennas and Propagation*, 1(1):1–266, Feb 2007.

[86] H. Giessen and J. Pendry. ,,Metamaterials: Optical Elements for the 21st Century; Conference Report: DPG Summer School, 17-22 Sept 2006, Bad Honnef, Germany". *Physica Status Solidi B*, 244(4):1167–1269, Apr 2007.

[87] R.S. Williams, X. Zhang, S. He, N. Fang, M.S. Islam, L. Thylen, and S.-Y. Wang. ,,Special Issue on Metamaterials". *Applied Physics A: Materials, Science and Processing*, 87(2):137–341, May 2007.

[88] E.E. Narimanov, V.M. Shalaev, and A.Z. Genack. ,,Special Issue on Photonic Metamaterials". *Journal of the Optical Society of America A*, 24(10):A1–A97, Oct 2007.

[89] Y. Lu, W. Zhang, and M. Qiu. ,,Special Issue on Metamaterials, Plasmonics, and THz Frequency Photonic Components". *Active and Passive Electronic Components*, 2007.

[90] R. Merlin, G. Shvets, and N. Engheta. ,,Special Section on Negative Refraction and Metamaterials for Optical Science and Engineering". *Solid State Communications*, 146(5-6):197–238, May 2008.

[91] M. Lapine. ,,The age of metamaterials". *Metamaterials*, 1(1):1, Mar 2007.

[92] A. Sihvola. ,,Electromagnetic emergence in metamaterials, deconstruction of terminology of complex media". In S. Zouhdi, A. Sihvola, and M. Arsalane, editors, *,,Advances in electromagnetics of complex media and metamaterials"*, volume 89 of *NATO Science Series, II. Mathematics, Physics and Chemistry*, pages 3–17, Amsterdam, 2002. Kluwer Academic Publishers.

[93] A. Sihvola. ,,Metamaterials in electromagnetics". *Metamaterials*, 1(1):2–11, 2007.

[94] E. Shamonina and L. Solymar. ,,Metamaterials: how the subject started". *Metamaterials*, 1(1):12–18, 2007.

[95] W.S. Weiglhofer and A. Lakhtakia, editors. *,,Introduction to complex mediums for optics and electromagnetics"*. SPIE Press, 2003.

[96] M.W. McCall, A. Lakhtakia, and W.S. Weiglhofer. ,,The negative index of refraction demystified". *European Journal of Physics*, 23(3):353–359, May 2002.

[97] R. Marques, F. Mesa, J. Martel, and F. Medina. ,,Comparative analysis of edge- and broadside-coupled split ring resonators for metamaterial design - theory and experiments". *IEEE Transactions on Antennas and Propagation*, 51(10):2572–2581, Oct 2003.

[98] R. Rotman. ,,Early work on artificial dielectrics, periodic structures and their relationship to modern metamaterials". In *Proceedings of the 10th International Conference on Electromagnetics in Advanced Applications (ICEAA'07)*, Torino, Italy, 17-21 Sept 2007.

[99] J.B. Pendry, A.J. Holden, W.J. Stewart, and I. Youngs. ,,Extremely low frequency plasmons in metallic mesostructures". *Physical Review Letters*, 76(25):4773–4776, 17 Jun 1996.

[100] P. Gay-Balmaz, C. Maccio, and O.J.F. Martin. ,,Microwire arrays with plasmonic response at microwave frequencies". *Applied Physics Letters*, 81(15):2896–2898, 7 Oct 2002.

[101] T. Weiland, R. Schuhmann, R.B. Greegor, C.G. Parazzoli, A.M. Vetter, D.R. Smith, D.C. Vier, and S. Schultz. ,,Ab initio numerical simulation of left-handed metamaterials: comparison of calculations and experiments". *Journal of Applied Physics*, 90(10):5419–5424, 15 Nov 2001.

[102] P. Markos and C.M. Soukoulis. ,,Transmission studies of left-handed materials". *Physical Review B*, 65:033401(1–4), 7 Dec 2001.

[103] D.R. Smith, D.C. Vier, N. Kroll, and S. Schultz. ,,Direct calculation of permeability and permittivity for a left-handed metamaterial". *Applied Physics Letters*, 77(14):2246–2248, 2 Oct 2000.

[104] P. Markos and C.M. Soukoulis. ,,Transmission properties and effective electromagnetic parameters of double negative metamaterials". *Optics Express*, 11(7):649–661, 7 Apr 2003.

[105] P.M. Valanju, R.M. Walser, and A.P. Valanju. ,,Wave refraction in negative-index media: always positive and very inhomogeneous". *Physical Review Letters*, 88(18):187401(1–4), 6 May 2002.

[106] M. Born and E. Wolf. *,,Principles of optics"*. Pergamon Press, 1959.

[107] D.R. Smith, D. Schurig, and J.B. Pendry. ,,Negative refraction of modulated electromagnetic waves". *Applied Physics Letters*, 81(15):2713–2715, 7 Oct 2002.

[108] J. Pacheco, T.M. Grzegorczyk, B.-I. Wu, Y. Zhang, and J.A. Kong. ,,Power propagation in homogeneous isotropic frequency-dispersive left-handed media". *Physical Review Letters*, 89(25):257401(1–4), 16 Dec 2002.

[109] J.B. Pendry and D.R. Smith. ,,Comment on Wave Refraction in Negative-Index Media: Always Positive and Very Inhomogeneous". *Physical Review Letters*, 90(2):029703(1), 17 Jan 2003.

[110] N. Garcia and M. Nieto-Vesperinas. ,,Is there an experimental verification of a negative index of refraction yet?". *Optics Letters*, 27(11):885–887, 1 Jun 2002.

[111] C.G. Parazzoli, R.B. Greegor, K. Li, B.E.C. Koltenbah, and M. Tanielian. ,,Experimental verification and simulation of negative index of refraction using Snell's law". *Physical Review Letters*, 90(10):107401(1–4), 14 Mar 2003.

[112] A.A. Houck, J.B. Brock, and I.L. Chuang. ,,Experimental observations of left-handed material that obeys Snell's law". *Physical Review Letters*, 90(13):137401(1–4), 4 Apr 2003.

[113] J.S. Derov, B.W. Turchinetz, E.E. Crisman, A.J. Drehman, S.R. Best, and R.M. Wing. ,,Free space measurements of negative refraction with varying angles of incidence". *IEEE Microwave and Wireless Components Letters*, 15(9):567–569, Sept 2005.

[114] C.D. Moss, T.M. Grzegorczyk, Y. Zhang, and J.A. Kong. ,,Numerical studies of left handed metamaterials". *Progress In Electromagnetics Research, PIER*, 35:315–334, 2002.

[115] Z.G. Dong, S.N. Zhu, H. Liu, J. Zhu, and W. Cao. ,,Numerical simulations of negative-index refraction in wedge-shaped metamaterials". *Physical Review E*, 72:016607(1–4), 12 Jul 2005.

[116] J.B. Pendry. ,,Negative refraction makes a perfect lens". *Physical Review Letters*, 85(18):3966–3969, 30 Oct 2000.

[117] G.W. 't Hooft. ,,Comment on negative refraction makes a perfect lens". *Physical Review Letters*, 87(24):249701(1), 10 Dec 2001.

[118] J.M. Williams. ,,Some problems with negative refraction". *Physical Review Letters*, 87(24):249703(1), 10 Dec 2001.

[119] N. Garcia and M. Nieto-Vesperinas. ,,Left-handed materials do not make a perfect lens". *Physical Review Letters*, 88(20):207403(1–4), 20 May 2002.

[120] J.B. Pendry. ,,Pendry replies". *Physical Review Letters*, 87(24):249702(1), 10 Dec 2001.

[121] J.B. Pendry. ,,Pendry replies". *Physical Review Letters*, 87(24):249704(1), 10 Dec 2001.

[122] J.B. Pendry. ,,Comment on Left-Handed Materials Do Not Make a Perfect Lens". *Physical Review Letters*, 91:099701(1), 29 Aug 2003.

[123] D.R. Smith, J.B. Pendry, and M.C.K. Wiltshire. ,,Metamaterials and negative refractive index". *Science*, 305:788–792, 6 Aug 2004.

[124] A. Grbic and G.V. Eleftheriades. ,,Overcoming the diffraction limit with a planar left-handed transmission line lens". *Physical Review Letters*, 92(11):117403(1–4), 19 Mar 2004.

[125] A.N. Lagarkov and V.N. Kissel. ,,Near-perfect imaging in a focusing system based on a left-handed-material plate". *Physical Review Letters*, 92(7):077401(1–4), 20 Feb 2004.

[126] R.J. Blaikie and D.O.S. Melville. ,,Imaging through planar silver lenses in the optical near field". *Journal of Optics A: Pure and Applied Optics*, 7(2):176–183, Feb 2005.

[127] N. Fang, H. Lee, C. Sun, and X. Zhang. ,,Sub-diffraction-limited optical imaging with a silver superlens". *Science*, 308:534–537, 22 Apr 2005.

[128] T. Taubner, D. Korobkin, Y. Urzhumov, G. Shvets, and R. Hillenbrand. ,,Near-field microscopy through a SiC superlens". *Science*, 313:1595, 15 Sept 2006.

[129] M. Gil, I. Gil, J. Bonache, J. Garcia-Garcia, and F. Martin. ,,Metamaterial transmission with extreme impedance values". *Microwave and Optical Technology Letters*, 48(12):2499–2505, Dec 2006.

[130] J.B. Pendry, D. Schurig, and D.R. Smith. ,,Controlling electromagnetic fields". *Science*, 312:1780–1782, 23 Jun 2006.

[131] U. Leonhardt. ,,Optical conformal mapping". *Science*, 312:1777–1780, 23 Jun 2006.

[132] D. Schurig, J.J. Mock, B.J. Justice, S.A. Cummer, J.B. Pendry, A.F. Starr, and D.R. Smith. ,,Metamaterial electromagnetic cloak at microwave frequencies". *Science*, 314:977–980, 10 Nov 2006.

[133] T.J. Yen, W.J. Padilla, N. Fang, D.C. Vier, D.R. Smith, J.B. Pendry, D.N. Basov, and X. Zhang. ,,Terahertz magnetic response from artificial materials". *Science*, 303:1494–1496, 5 Mar 2004.

[134] S. Linden, C. Enkrich, M. Wegener, J. Zhou, T. Koschny, and C.M. Soukoulis. ,,Magnetic response of metamaterials at 100 Terahertz". *Science*, 306:1351–1353, 19 Nov 2004.

[135] S. Linden, C. Enkrich, G. Dolling, M.W. Klein, J. Zhou, T. Koschny, C.M. Soukoulis, S. Burger, F. Schmidt, and M. Wegener. ,,Photonic metamaterials: magnetism at optical frequencies". *IEEE Journal of Selected Topics in Quantum Electronics*, 12(6):1097–1105, Nov/Dec 2006.

[136] T.A. Klar, A.V. Kildishev, V.P. Drachev, and V.M. Shalaev. ,,Negative-index metamaterials: going optical". *IEEE Journal of Selected Topics in Quantum Electronics*, 12(6):1106–1115, Nov/Dec 2006.

[137] V.M. Shalaev. ,,Optical negative-index metamaterials". *Nature Photonics*, 1:41–48, Jan 2007.

[138] L.D. Landau and E.M. Lifshitz. *,,Electrodynamics of continuous media"*. Pergamon Press, 1960.

[139] E.J. Rothwell and M.J. Cloud. *,,Electromagnetics"*. CRC Press, 2001.

[140] K.E. Oughstun and N.A. Catwright. ,,On the Lorentz-Lorenz formula and the Lorentz model of dielectric dispersion". *Optics Express*, 11(13):1541–1546, 30 Jun 2003.

[141] N.W. Ashcroft and N.D. Mermin. *,,Solid state physics"*. Harcourt College Publishers, 1976.

[142] Microwave Studio. CST Darmstadt, Germany, 2008. http://www.cst.com.

[143] T. Weiland. ,,A discretization method for the solution of Maxwell's equations for six-component fields". *AEÜ International Journal of Electronics and Communications*, 31(3):116–120, 1977.

[144] T. Weiland. ,,Verfahren und Anwendungen der Feldsimulation". Skriptum zum Vorlesung, Technische Universität Darmstadt, 2004.

[145] H. Krüger. *,,Zur numerischen Berechnung transienter elektromagnetischer Felder in gyrotropen Materialien"*. PhD thesis, Technische Universität Darmstadt, 2000.

[146] K.S. Yee. ,,Numerical solution of initial boundary value problems involving Maxwell's equations in isotropic media". *IEEE Transactions on Antennas and Propagation*, 14(3):302–307, May 1966.

[147] T. Weiland. ,,Time domain electromagnetic field computation with finite difference methods". *International Journal of Numerical Modelling*, 9:295–319, 1996.

[148] T. Weiland. ,,Modes in infinitely repeating structures of cylindrical symmetry". In *Proceedings of the 1986 Linear Accelerator Conference (LINAC86)*, pages 292–295, Stanford University, Stanford, USA, 2-6 Jun 1986.

[149] J.P. Berenger. ,,A perfectly matched layer for the absorption of electromagnetic waves". *Journal of Computational Physics*, 114:185–200, 1994.

[150] P. Thoma. *,,Zur numerischen Lösung der Maxwellschen Gleichungen im Zeitbereich"*. PhD thesis, Technische Universität Darmstadt, 1997.

[151] W.J. Padilla. ,,Group theoretical description of artificial electromagnetic metamaterials". *Optics Express*, 15(4):1639–1646, 19 Feb 2007.

[152] J.D. Baena, L. Jelinek, and R. Marques. ,,Towards a systematic design of isotropic bulk magnetic metamaterials using the cubic point groups of symmetry". *Physical Review B*, 76(24):245115(1–14), 17 Dec 2007.

[153] T. Koschny, L. Zhang, and C.M. Soukoulis. ,,Isotropic three-dimensional left-handed metamaterials". *Physical Review B*, 71(12):121103(1–4), 21 Mar 2007.

[154] D.R. Smith, J. Gollub, J.J. Mock, W.J. Padilla, and D. Schurig. ,,Calculation and measurement of bianisotropy in a split ring resonator metamaterial". *Journal of Applied Physics*, 100(2):024507(1–9), 21 Jul 2006.

[155] J. Garcia-Garcia, F. Martin, J.D. Baena, R. Marques, and L. Jelinek. ,,On the resonances and polarizabilities of split ring resonators". *Journal of Applied Physics*, 98:033103(1–9), 2005.

[156] A.M. Nicolson and G.F. Ross. ,,Measurement of the intrinsic properties of materials by time-domain techniques". *IEEE Transactions on Instrumentation and Measurement*, 19(4):377–382, Nov 1970.

[157] D.R. Smith, S. Schultz, P. Markos, and C.M. Soukoulis. ,,Determination of effective permittivity and permeability of metamaterials from reflection and transmission coefficients". *Physical Review B*, 65:195104(1–5), 19 Apr 2002.

[158] X. Chen, T.M. Grzegorczyk, B.-I. Wu, J. Pacheco, and J.A. Kong. ,,Robust method to retrieve the constitutive effective parameters of metamaterials". *Physical Review E*, 70:016608(1–7), 26 Jul 2004.

[159] R.W. Ziolkowski. ,,Design, fabrication and testing of double negative metamaterials". *IEEE Transactions on Antennas and Propagation*, 51(7):1516–1529, Jul 2003.

[160] J. Zhou, L. Zhang, G. Tuttle, T. Koschny, and C.M. Soukoulis. ,,Negative index materials using simple short wire pairs". *Physical Review B*, 73(4):041101(1–4), 4 Jan 2006.

[161] A.L. Efros. ,,Comment II on Resonant and antiresonant frequency dependence of the effective parameters of metamaterials". *Physical Review E*, 70:048602(1), 29 Oct 2004.

[162] R.A. Depine and A. Lakhtakia. ,,Comment I on Resonant and antiresonant frequency dependence of the effective parameters of metamaterials". *Physical Review E*, 70:048601(1), 29 Oct 2004.

[163] D.R. Smith and J.B. Pendry. ,,Homogenization of metamaterials by field averaging (invited paper)". *Journal of the Optical Society of America B*, 23(3):391–402, Mar 2006.

[164] D.R. Smith, W.J. Padilla, D.C. Vier, R. Shelby, S.C. Nemat-Nasser, N. Kroll, and S. Schultz. ,,Left-handed metamaterials". In C.M. Soukoulis, editor, *Photonic crystals and light localization in the 21st century*, NATO Science Series C: Mathematical and Physical Sciences, Heraklion, Crete, 19-30 Jun 2000. NATO-ASI, Kluwer Academic Publishers.

[165] S.I. Maslovski, S.A. Tretyakow, and P.A. Belov. ,,Wire media with negative effective permittivity: a quasi-static model". *Microwave and Optical Technology Letters*, 35(1):47–51, 5 Oct 2002.

[166] O. Acher, A.L. Adenot, and F. Duverger. ,,Fresnel coefficients at an interface with a lamellar composite material". *Physical Review B*, 62(20):13748–13756, 15 Nov 2000.

[167] J.-M. Lerat, N. Mallejac, and O. Acher. ,,Determination of the effective parameters of a metamaterial by field summation method". *Journal of Applied Physics*, 100(8):084908(1–9), 25 Oct 2006.

[168] O. Acher, J.-M. Lerat, and N. Mallejac. ,,Evaluation and illustration of the properties of metamaterials using field summation". *Optics Express*, 15(3):1096–1106, 5 Feb 2007.

[169] O. Acher, J.-M. Lerat, and N. Mallejac. ,,The field summation method: an efficient route to determine epsilon and mu of metamaterials". In *Proceedings of 1st International Congress on Advanced Electromagnetic Materials in Microwaves and Optics (Metamaterials 2007)*, Rome, Italy, 22-24 Oct 2007.

[170] C. Croenne, J.M. Lerat, M.N. Mallejac, O. Acher, and D. Lippens. ,,Retrieval technique by field summation: application to double negative media". In *Proceedings of 1st International Congress on Advanced Electromagnetic Materials in Microwaves and Optics (Metamaterials 2007)*, pages 706–709, Rome, Italy, 22-24 Oct 2007.

[171] G. Lubkowski, R. Schuhmann, and T. Weiland. ,,Extraction of effective metamaterial parameters by parameter fitting of dispersive models". *Microwave and Optical Technology Letters*, 49(2):285–288, Feb 2007.

[172] R. Storn and K. Price. ,,Differential evolution - a simple and efficient heuristic for global optimization over continuous spaces'. *Journal of Global Optimization*, 11:341–359, 1997.

[173] D. Corne, M. Dorigo, and F. Glover, editors. *,,New ideas in optimization"*. McGraw-Hill, London, 1999.

[174] R.W. Ziolkowski and C. Ching-Ying. ,,Existence and design of trans-vacuum-speed metamaterials". *Physical Review E*, 68:026612(1–18), 25 Aug 2003.

[175] S.A. Tretyakov. ,,Comment on Existence and design of trans-vacuum-speed metamaterials". *Physical Review E*, 70:068601(1–2), 6 Dec 2004.

[176] R.W. Ziolkowski. ,,Reply to Comment on Existence and design of trans-vacuum-speed metamaterials". *Physical Review E*, 70:068602(1–2), 6 Dec 2004.

[177] S. Enoch, G. Tayeb, and D. Maystre. ,,Dispersion diagrams of Bloch modes applied to the design of directive sources". *Progress In Electromagnetics Research, PIER*, 41:61–81, 2003.

[178] B. Gralak, S. Enoch, and G. Tayeb. ,,Anomalous refractive properties of photonic crystals". *Journal of the Optical Society of America A*, 17(6):1012–1020, Jun 2000.

[179] S. Foteinopoulou and C.M. Soukoulis. ,,Negative refraction and left-handed behavior in two-dimensional photonic crystals". *Physical Review B*, 67:235107(1–5), 22 Mar 2003.

[180] M. Ghebrebrhan, M. Ibanescu, S.G. Johnson, M. Soljacic, and J.D. Joannopoulos. ,,Distinguishing zero-group-velocity modes in photonic crystals". *Physical Review A*, 76:063810(1–6), 14 Dec 2007.

[181] B. Bandlow. ,,Entwurf, Simulation und experimentelle Validierung von Metamaterialien für Hohlleiteranwendungen". Diplomarbeit, Technische Universität Darmstadt, Fachbereich 18, 5 Oct 2005.

[182] G. Lubkowski, C. Damm, B. Bandlow, R. Schuhmann, M. Schüßler, and T. Weiland. ,,Broadband transmission below the cutoff frequency of a waveguide loaded with resonant scatterer arrays". *IET Microwaves, Antennas and Propagation*, 1(1):165–169, Feb 2007.

[183] G. Lubkowski, C. Damm, B. Bandlow, R. Schuhmann, M. Schüßler, and T. Weiland. ,,Metamaterial loaded waveguides for miniaturized filter applications". *Frequenz*, 62(3-4):71–74, Mar/Apr 2008.

[184] G. Lubkowski, C. Damm, B. Bandlow, R. Schuhmann, M. Schüßler, and T. Weiland. ,,Waveguide miniaturization using spiral resonators and dipole arrays". In *Proceedings of 36th European Microwave Conference (EuMC 2006)*, pages 1312–1315, Manchester, UK, 10-15 Sept 2006.

[185] G. Lubkowski, C. Damm, B. Bandlow, R. Schuhmann, M. Schüßler, and T. Weiland. ,,Experimental study of subwavelength waveguides loaded by electric and magnetic resonant scatterer arrays". In *Proceedings of 38th European Microwave Conference (EuMC 2008)*, pages 1050–1053, Amsterdam, 27-31 Oct 2008.

[186] R. Marques, J. Martel, F. Mesa, and F. Medina. ,,Left-handed-media simulation and transmission of em waves in subwavelength split-ring-resonator-loaded metallic waveguides". *Physical Review Letters*, 89(18):183901(1–4), 28 Oct 2002.

[187] R. Marques, J. Martel, F. Mesa, and F. Medina. ,,A new 2D isotropic left-handed metamaterial design: theory and experiment". *Microwave and Optical Technology Letters*, 35(5):405–408, 5 Dec 2002.

[188] C.R. Simovski. ,,Plane-wave reflection and transmission by grids of conducting omega particles and dispersion of omega electromagnetic crystals". *AEÜ International Journal of Electronics and Communications*, 57(5):358–364, 2003.

[189] J.D. Baena, R. Marques, F. Medina, and J. Martel. ,,Artificial magnetic metamaterial design by using spiral resonators". *Physical Review B*, 69:014402(1–5), 8 Jan 2004.

[190] M. Caiazzo, S. Maci, and N. Engheta. ,,A metamaterial surface for compact cavity resonators". *IEEE Antennas and Wireless Propagation Letters*, 3:261–264, 2004.

[191] T. Bertuch. ,,A TM leaky-wave antenna comprising a textured surface". In *Proceedings of the 10th International Conference on Electromagnetics in Advanced Applications (ICEAA'07)*, Torino, Italy, 17-21 Sept 2007.

[192] S. Hrabar, J. Bartolic, and Z. Sipus. ,,Waveguide miniaturization using uniaxial negative permeability metamaterial". *IEEE Transactions on Antennas and Propagation*, 53(1):110–119, Jan 2005.

[193] P.A. Belov and C.R. Simovski. ,,Subwavelength metallic waveguides loaded by uniaxial resonant scatterers". *Physical Review E*, 72:036618(1–11), 29 Sept 2005.

[194] B. Bandlow, G. Lubkowski, R. Schuhmann, and T. Weiland. ,,Analysis of single-cell modeling of periodic metamaterial structures". *IEEE Transactions on Magnetics*, 44(6):1662–1665, Jun 2008.

[195] G. Lubkowski, B. Bandlow, R. Schuhmann, and T. Weiland. ,,Effective modeling of double negative metamaterial macrostructures". *IEEE Transactions on Microwave Theory and Techniques*, 57(5):1136–1146, May 2009.

[196] D. Seetharamdoo, R. Sauleau, K. Mahdjoubi, and A.-C. Tarot. ,,Effective parameters of resonant negative refractive index metamaterials: interpretation and validity". *Journal of Applied Physics*, 98:063505(1–4), 19 Sept 2005.

[197] G. Lubkowski, F. Hirtenfelder, B. Bandlow, R. Schuhmann, and T. Weiland. ,,Macromodeling of parabolic double negative metamaterial antennas". *Frequenz*, 62(3-4):67–70, Mar/Apr 2008.

[198] D.R. Smith, P. Kolinko, and D. Schurig. ,,Negative refraction in indefinite media". *Journal of the Optical Society of America B*, 21(5):1032–1043, May 2004.

[199] S. Ougier, I. Chenerie, A. Sihvola, and A. Priou. ,,Propagation in bi-isotropic media: effect of different formalisms on the propagation analysis". *Progress In Electromagnetics Research, PIER*, 9:19–30, 1994.

[200] J. Baker-Jarvis, E.J. Vanzura, and W.A. Kissick. ,,Improved technique for determining complex permittivity with the transmission/reflection method". *IEEE Transactions on Microwave Theory and Techniques*, 38(8):1096–1103, Aug 1990.

[201] W.B. Weir. ,,Automatic measurement of complex dielectric constant and permeability at microwave frequencies". *Proceedings of the IEEE*, 62(1):33–36, Jan 1974.

Journal papers and conference contributions published in the frame of this work

Journals

G. Lubkowski, R. Schuhmann, and T. Weiland. "Extraction of effective metamaterial parameters by parameter fitting of dispersive models". *Microwave and Optical Technology Letters*, 49(2):285-288, Feb 2007.

G. Lubkowski, C. Damm, B. Bandlow, R. Schuhmann, M. Schüßler, and T. Weiland. "Broadband transmission below the cutoff frequency of a waveguide loaded with resonant scatterer arrays". *IET Microwaves, Antennas and Propagation*, 1(1):165-169, Feb 2007.

G. Lubkowski, F. Hirtenfelder, B. Bandlow, R. Schuhmann, and T. Weiland. "Macromodeling of parabolic double negative metamaterial antennas". *Frequenz*, 62(3/4):67-70, Mar/Apr 2008.

G. Lubkowski, C. Damm, B. Bandlow, R. Schuhmann, M. Schüßler, and T. Weiland. "Metamaterial loaded waveguides for miniaturized filter applications". *Frequenz*, 62(3/4): 71-74, Mar/Apr 2008.

R. Schuhmann, B. Bandlow, G. Lubkowski, and T. Weiland. "Micro- and macroscopic simulation of periodic metamaterials". *Advances in Radio Science*, 6:77-82, May 2008.

B. Bandlow, G. Lubkowski, R. Schuhmann, and T. Weiland. "Analysis of single-cell modeling of periodic metamaterial structures". *IEEE Transactions on Magnetics*, 44(6):1662-1665, Jun 2008.

G. Lubkowski, B. Bandlow, R. Schuhmann, and T. Weiland. "Effective modeling of double negative metamaterial macrostructures". *IEEE Transactions on Microwave Theory and Techniques*, 57(5):1136-1146, May 2009.

Conferences

G. Lubkowski, R. Schuhmann, and T. Weiland. "Computation of effective material parameters for double negative metamaterial cells based on 3D field simulations". *Proceedings of EPFL Latsis Symposium (LATSIS 2005)*, p. 94, Lausanne, Switzerland, 28 Feb - 2 Mar 2005.

R. Schuhmann, G. Lubkowski, and T. Weiland. "Full-wave simulations and extraction of effective material parameters for left-handed metamaterials". *Proceedings of the German Microwave Conference (GeMIC 2005)*, pp. 201-204, Ulm, 5-7 Apr 2005.

G. Lubkowski, R. Schuhmann, and T. Weiland. "Computation of effective magnetic permeability for ring resonator structures based on 3D field simulations". *Proceedings of the Seminar on Metamaterials and Circuit Design based on Split Ring Resonators*, Barcelona, Spain, 22 Apr 2005.

G. Lubkowski, R. Schuhmann, and T. Weiland. "Extraction of effective material parameters for double negative metamaterials from 3D field simulations". *IEEE International Symposium on Antennas and Propagation and USNC/CNC/URSI North American Radio*

Science Meeting, Washington DC, USA, 3-8 Jul 2005.

G. Lubkowski, R. Schuhmann, and T. Weiland. "Effective metamaterial representation by parameter-fitting of dispersion models". *Proceedings of the Progress in Electromagnetics Research Symposium (PIERS 2006)*, p. 87, Cambridge, MA, USA, 26-29 Mar 2006.

G. Lubkowski, C. Damm, B. Bandlow, R. Schuhmann, M. Schüßler, and T. Weiland. "Waveguide miniaturization using spiral resonators and dipole arrays". *Proceedings of 36th European Microwave Conference (EuMC 2006)*, pp. 1312-1315, Manchester, UK, 10-15 Sept 2006.

F. Hirtenfelder and G. Lubkowski. "3D field simulations using FI time domain technique of wedge- and parabolic-shaped left handed materials (LHM)". *Proceedings of 2007 IEEE International Workshop on Antenna Technology: Small and Smart Antennas, Metamaterials and Applications*, pp. 259-262, Cambridge, UK, 21-23 Mar 2007.

B. Bandlow, G. Lubkowski, R. Schuhmann, and T. Weiland. "An analysis of single-cell modeling of periodic metamaterial structures". *Proceedings of 16th International Conference on the Computation of Electromagnetic Fields (Compumag 2007)*, pp. 501-502, Aachen, Germany, 24-28 Jun 2007.

R. Schuhmann, B. Bandlow, G. Lubkowski, and T. Weiland. "Mikro- und Makroskopische Simulation von Periodischen Metamaterialien". *U.R.S.I. Landesausschuss Deutschland e.V., Kleinheubacher Tagung 2007*, Miltenberg, Germany, 24-27 Sept 2007.

G. Lubkowski, F. Hirtenfelder, R. Schuhmann, and T. Weiland. "3D full-wave field simulations of double negative metamaterial macrostructures". *Proceedings of 1st International Congress on Advanced Electromagnetic Materials in Microwaves and Optics (Metamaterials 2007)*, pp. 731-734, Rome, Italy, 22-26 Oct 2007.

G. Lubkowski, C. Damm, B. Bandlow, R. Schuhmann, M. Schüßler, and T. Weiland. "Metamaterial loaded waveguides for filter applications". *Metamaterials Week 2008*, Barcelona, Spain, 5-8 Feb 2008.

G. Lubkowski, C. Damm, B. Bandlow, R. Schuhmann, M. Schüßler, and T. Weiland. "Experimental study of subwavelength waveguides loaded by electric and magnetic resonant scatterer arrays". *Proceedings of 38th European Microwave Conference (EuMC 2008)*, pp. 1050-1053, Amsterdam, 27-31 Oct 2008.

M. Maasch, M. Schüßler, E. Gonzalez Rodriguez, C. Damm, G. Lubkowski, R. Jakoby. "Voltage Tunable Split-Ring-Resonators for Waveguide Applications". *Proceedings of 3rd International Congress on Advanced Electromagnetic Materials in Microwaves and Optics (Metamaterials 2009)*, London, UK, 30 Aug - 4 Sept 2009.

Supervised Research/Diploma Projects

B. Bandlow. "Metamaterialien". Studienarbeit, Technische Universität Darmstadt, Fachbereich 18, 21 Feb 2005.

B. Bandlow. "Entwurf, Simulation und experimentelle Validierung von Metamaterialien für Hohlleiteranwendungen". Diplomarbeit (co-supervised with Dipl.-Ing. Christian Damm, Fachgebiet für Mikrowellentechnik), Technische Universität Darmstadt, Fachbereich 18, 5 Oct 2005.

Acknowledgments

Many people and institutions provided support during the whole time of my work on this PhD project. I would like to thank:

- Prof. Dr.-Ing. Thomas Weiland for providing the opportunity of working in an excellent research environment at TEMF.
- Prof. Dr.-Ing. Rolf Schuhmann for careful reviewing and correcting of the manuscript and numerous useful discussions regarding the shape of this thesis.
- Prof. Dr.-Ing. Rolf Jakoby for careful reading and reviewing of the manuscript and providing an interesting interdisciplinary research environment in the frame of the Graduiertenkolleg TICMO.
- Dr.-Ing. Wolfgang Ackermann for valuable discussions and plenty of helpful tips regarding computational electromagnetics.
- Dipl.-Ing. Bastian Bandlow, Dipl.-Ing. Christian Damm and Dr.-Ing. Martin Schüßler for fruitful cooperation related to metamaterial loaded waveguides.
- Dipl.-Ing. Franz Hirtenfelder (CST) for smooth cooperation regarding simulation of metamaterial macrostructures.
- D.Sc. Pekka Ikonen (Nokia) for providing access to publications concerning early research on artificial dielectrics.
- PhD Lukas Jelinek (University of Seville) for helpful discussion of bianisotropic effects in metamaterial structures.
- Heike Seiler for readiness to help in administrative and daily issues.
- All colleagues at TEMF for creating a pleasant and nice working environment.

A special thank goes to my family, especially my wife Marzena, for a constant support, and Mark Spence for corrections of the manuscript.

Curriculum Vitae

Grzegorz Lubkowski
born on 23 July 1976 in Gdansk (Danzig)

1983-1991	Primary school, Gdansk
1991-1996	Technical College of Electronics and Telecommunication, Gdansk Technician of Telecommunication
1996-2001	Gdansk University of Technology Faculty of Electronics, Telecommunication and Computer Sciences MSc in Microwave Engineering and Optical Telecommunication First Class Honours Degree
2000-2002	Gdansk University of Technology Faculty of Management and Economics MSc in Organization and Design of Production Systems
2002-2004	Fraunhofer Institut für Zuverlässigkeit und Mikrointegration, Paderborn R&D engineer
2004-2009	Technische Universität Darmstadt Institut für Theorie Elektromagnetischer Felder Research associate